ISTANBUL TECHNICAL UNIVERSITY ★ GRADUATE SCHOOL

NUMERICAL INVESTIGATION OF THE INFLUENCE OF SWEEP AND LEAN ON A TRANSONIC AXIAL COMPRESSOR ROTOR

M.Sc. THESIS

Hasan Berk GÜÇLÜ

Department of Aeronautical and Astronautical Engineering

Aeronautical and Astronautical Engineering Programme

AUGUST 2023

ISTANBUL TECHNICAL UNIVERSITY ★ GRADUATE SCHOOL

NUMERICAL INVESTIGATION OF THE INFLUENCE OF SWEEP AND LEAN ON A TRANSONIC AXIAL COMPRESSOR ROTOR

M.Sc. THESIS

Hasan Berk GÜÇLÜ
(511201129)

Department of Aeronautical and Astronautical Engineering

Aeronautical and Astronautical Engineering Programme

Thesis Advisor: Prof. Dr. Aydın Mısırlıoğlu

AUGUST 2023

ISTANBUL TEKNİK ÜNİVERSİTESİ ★ LİSANSÜSTÜ EĞİTİM ENSTİTÜSÜ

TRANSONİK EKSENEL KOMPRESÖR ROTORUNDA UYGULANAN 'SWEEP' VE 'LEAN' METHODLARININ AERODİNAMİK ETKİLERİNİN NÜMERİK YAKLAŞIMLAR İLE İNCELENMESİ

YÜKSEK LİSANS TEZİ

Hasan Berk Güçkü
(511201129)

Uçak ve Uzay Mühendisliği Anabilim Dalı

Uçak ve Uzay Mühendisliği Programı

Tez Danışmanı: Prof. Dr. Aydın Mısırlıoğlu

AĞUSTOS 2023

Hasan Berk Güçlü, a M.Sc. student of ITU Graduate School student ID 511201129, successfully defended the thesis/dissertation entitled "NUMERICAL INVESTIGATION OF THE INFLUENCE OF SWEEP AND LEAN ON A TRANSONIC AXIAL COMPRESSOR ROTOR", which he prepared after fulfilling the requirements specified in the associated legislations, before the jury whose signatures are below.

Thesis Advisor	**Prof. Dr. Aydın MISIRLIOĞLU** İstanbul Technical University	.....
Jury Members	**Prof. Dr. Fırat Oğuz EDİS** Istanbul Technical University	.....
	Asst. Prof.Onur SON Gebze Technical University	.....

Date of Submission : 7 July 2023
Date of Defense : 2 August 2023

To my family,

FOREWORD

Firstly, I would like to express my deepest gratitude to my advisor Prof. Dr. Aydın Mısırlıoğlu for the wise guidance that he showed during my journey.

Also, an important thanks should be addressed to my colleagues and the TUSAS Engine Industries (TEI) for inspiring me and providing a sustainable research environment.

August 2023

Hasan Berk GÜÇLÜ
Aerodynamics Engineer

TABLE OF CONTENTS

Page

ABBREVIATIONS

AGARD : Advisory Group for Aerospace Research and Development
B2B : Blade-to-blade
CFD : Computational Fluid Dynamics
ITU : Istanbul Technical University
MFR : Mass Flow Rate
NASA : National Aeronautics and Space Administration
PR : Pressure Ratio
RPM : Revolutions per Minute
SFC : Specific Fuel Consumption
SM : Stall Margin
TLF : Tip Leakage Flow
TLV : Tip Leakage Vortex
TR : Temperature Ratio

SYMBOLS

ρ	**:** Density
M	**:** Mach Number
P	**:** Static Pressure
PR	**:** Total Pressure Ratio
R	**:** Gas Constant
SM	**:** Stall Margin
T	**:** Static Temperature
TR	**:** Total Temperature Ratio

LIST OF TABLES

Page

LIST OF FIGURES

Page

NUMERICAL INVESTIGATION OF THE INFLUENCE OF SWEEP AND LEAN ON A TRANSONIC AXIAL COMPRESSOR ROTOR

SUMMARY

The state-of-the-art gas turbine engine technology tends to have modules with superior loadings within the compact design strategy.

The technology trend created a necessity to design transonic high-pressure compressors that are efficient while having a reasonably high operational range.

Transonic regime creates additional design aspects that need to be carefully done, mainly shock related structures and losses.

An efficient way to control shock structure is three-dimensional stacking, namely sweep and lean, which has been used for aircraft wing designs.

The recent studies relevant to the three-dimensional stacking of compressor blades have not completely enlightened the flow mechanism behind the sweep and lean, which keeps the controversy about the sweep and lean alive.

This paper aims to investigate the influence of three-dimensional stacking, namely true sweep and lean, on a transonic axial compressor stage with a 3D Reynolds Averaged Navier-Stokes solver. NASA Rotor 37, which is a common benchmark case used for numerical studies in the literature, is used for validation and further investigation study. A total of 8 new geometries based on NASA Rotor 37 have been generated that are swept and leaned with different characteristics. The generated geometries have been investigated with the validated numerical approach in terms of the flow field in a systematic way. The results show that the axially aft sweep and positive lean design improve the design point in terms of isentropic efficiency and stall margin. The mechanism behind the improvement is seen to be the relocation of the passage shock and the weakening of the tip leakage vortex.

The outstanding cases among the offered geometries in terms of efficiency and the operational range are combined and investigated through a similar systematical approach. It is seen that the combined geometry has a 4.67% stall margin improvement and 0.83% isentropic efficiency improvement. It is noted that the improvement of the global performance parameters of combined geometry is higher than in singular cases however it is not the direct superposition of singular geometries' characters.

TRANSONİK EKSENEL KOMPRESÖR ROTORUNDA UYGULANAN ‘SWEEP’ VE ‘LEAN’ METHODLARININ AERODİNAMİK ETKİLERİNİN NÜMERİK YAKLAŞIMLAR İLE İNCELENMESİ

ÖZET

Havacılık endüstrisindeki rekabeti oluşturan önemli unsurlardan bir tanesi olan kompakt tasarım felsefesidir. Gaz türbinli motorlardaki teknoloji eğiliminin gelişiminde de önemli bir rol oynayan bu felsefe, özellikle havacılık motorlarında yüksek yükleme altında çalışan kompakt modül tasarımlarının ortaya çıkması ihtiyacını oluşturmuştur. Bunun yanında, modül verimlerinin iyileştirilmesi de gaz türbinli motor teknolojisinin gelişiminin önemli bir parçasıdır. Özellikle yüksek basınç kompresörlerinden elde edilebilecek yüksek verimin spesifik yakıt tüketiminin iyileştirilmesi ile doğrudan bağlı olduğu bilinmektedir. Hem verim hem de kompakt tasarım felsefesi açısından rekabetçi kompresör tasarımların ortaya koyulabilmesinin önemi günümüz gaz türbinli motor teknolojisinin gelişimi ile artmaya devam etmektedir.

Hem yüksek verimlilikte çalışabilen hem de yeterli operasyonel marjine sahip kompakt yüksek basınç kompresörlerinin tasarlanması ihtiyacı, transonik rejimde çalışan modül tasarımlarını gerektirmektedir. Günümüzde kullanılan yüksek basınç kompresörlerinin giriş kademeleri genellikle transonik akış rejiminde olacak şekilde tasarlanmıştır. Transonik akış rejimi, aerodinamik tasarım açısından dikkatli yaklaşılması gereken şok yapıları ve şok yapılarından tetiklenen ekstra kayıp mekanizmlarını içermektedir. Oluşan şok yapılarını ve şok yapılarından kaynaklanan performans etkilerini kontrol etmenin etkili bir yolu son yıllarda sıklıkla kullanılan üç boyutlu örme methodları olan ‘sweep’ ve ‘lean’ uygulamalarıdır. Bu yaklaşımlar uzun yıllardır uçak kanatlarında başarı ile uygulanmaktadır.

Kompresör uygulamalarında kullanılan üç boyutlu örme methodları hakkında yapılan çalışmalar, bu uygulamaların arkasında yatan akış fiziğinin tam anlamıyla aydınlatılamamıştır. Bu sebeple ‘sweep’ ve ‘lean’ uygulamaları hakkındaki akademik araştırma ve tartışma süreçleri devam etmektedir. Bu tez çalışmasında, üç boyutlu örme yaklaşımları olan ‘sweep’ ve ‘lean’ uygulamalarının kompresör akışı üzerindeki etkileri, bir transonik eksenel kompresör rotoru üzerinde yapılan üç-boyutlu Reynolds Ortalamalı Akış Çözücüsü yöntemiyle nümerik olarak incelenmiştir.

Literatürde nümerik çalışmalar için oldukça yaygın biçimde kullanılan NASA Rotor 37 geometrisi, validasyon ve detaylı inceleme çalışmaları için kullanılmıştır. Çok kademeli bir yüksek basınç kompresörünün giriş kademesi olarak tasarlanan NASA Stage 37 bu tez kapsamında odaklanılan problem açısından oldukça uygundur.

Dört farklı yapıda çözüm ağı oluşturularak HAD modelinin ağdan bağımsızlığı araştırılmıştır. Hem çözüm maliyetleri hem de sayısal doğruluk açısında makul olan çözüm ağı detaylı çalışmalarda kullanılmak üzere seçilmiştir. HAD modelinden elde edilen akış alanı çıktıları literatürde yer alan deneysel sonuçlar ile kıyaslanmıştır. Hem global performans haritaları hem çıkış düzlemindeki radyal akış profilleri hem de B2B

düzlemi akış alanları ile yapılan bu kıyaslama sonucunda sayısal modelin yeterli doğruluğu sağladığı ortaya koyulmuştur.

‘Sweep’ ve ‘lean’ uygulamalarının araştırılması amacıyla NASA Rotor 37 kanadı baz alınarak farklı karakterdeki kanatlar üretilmiştir. Toplamda 8 farklı kanat üretilmiş ve doğrulaması yapılan nümerik yöntem ile akış alanları incelenmiştir. Bu inceleme elde edilen kanatların global performans çıktıları, radyal yöndeki akış karakterleri, B2B düzlemlerindeki akış alanları, emme yüzeylerindeki akış çizgileri ve uç açıklığı girdabını içerecek şekilde sistematik bir yaklaşım içerisinde sunulmuştur.

Global performans açısından geri ‘sweep’ yapısına sahip kanat geometrisinin hem daha yüksek operasyonel zarfa hem de daha yüksek verim davranışına sahip olduğu görülmüştür. Benzer şekilde pozitif ‘lean’ yapısına sahip kanat geometrisinin operasyonellik ve verim açısından daha avantajlı olduğu görülmüştür. Ayrıca ‘sweep’ uygulamasının boğulma debisinin değişimine neden olduğu fakat ‘lean’ uygulamasının böyle bir etkide bulunmadığı görülmüştür.

Radyal yöndeki akış profillerinin incelenmesi ile üç boyutlu örme methodları uygulanan kanatların özellikle uç bölgesinde farklılık gösterdiği görülmüştür. Bu durumun uç açıklığı girdabında yaşanan değişim nedeniyle olduğu yorumlanmıştır. B2B düzlemde yapılan relatif Mach alanı incelemesi ile şok sisteminde yaşanan değişim ortaya koyulmuştur. İleri ‘sweep’ uygulaması ile pasaj şokunun hücum kenarına doğru ilerlediği görülmüştür. Bu durum nedeniyle hem operasyonellik hem de verim açısından daha dezavantajlı bir koşul oluşmuştur. Ayrıca hücum kenarına yakın bölgede yüklemenin artması nedeniyle uç açıklığı girdabının daha güçlü olmasına neden olduğu görülmüştür. Geri ‘sweep’ uygulamasında ise bahsi geçen tüm fenomenlerin tersi yönde işleyerek iyileştirilmiş bir akış alanı ortaya koyduğu görülmektedir.

Benzer incelemeler ‘lean’ uygulaması olan kanatlar için de yapılmıştır. Dönüş yönünde uygulanan pozitif ‘lean’ uygulaması ile bahsi geçen mekanizmaların benzer şekilde gelişmesi sonucunda akış alanında iyileşme sağladığı görülmüştür.

Kanat yüzeyindeki akış çizgileri üzerinden yapılan incelemelerde şok mekanizmasında yaşanan değişimler ve bağlantılı olarak değişim gösteren ayrılma baloncukları gösterilmiştir. Elde edilen tüm çözümlerde şok yapısının radyal yöndeki karakterinin duvar ile dik kesişimi sağlayacak şekilde yeniden düzenlendiği görülmüştür. Literatürde de bahsedilen bu durum çözüm modelinde de doğrulanmıştır.

Yapılan incelemelerde genel olarak eksenel olarak geri ‘sweep’ yapısı ve dönüş yönünde pozitif ‘lean’ karakterine sahip olan kanatların hem operasyonal marjin hem de verimlilik anlamında daha başarılı olduğu görülmüştür. Aerodinamik iyileşmenin arkasındaki ana mekanizmanın şok sisteminde yaşanan değişim ve uç girdabının zayıflaması olduğu görülmüştür.

İncelenen kanat yapıları arasında verim ve operasyonel marjin açısından en başarılı geometrilerin karakterleri olan geri ‘sweep’ ve pozitif ‘lean’ yaklaşımları kombine edilerek yeni bir kanat yapısı oluşturulmuştur. Bu aşamaya kadar tekil yaklaşım ile incelenen üç boyutlu örme methodları, bu aşamada kombine uygulanmaları durumunda incelenmiştir.

Final kanat yapısı baz alınan NASA Rotor 37 modeline göre %4.67 operasyonel marjin artışı ve %0.83 izantropik verim artışı göstermiştir. Kombine edilen geometrinin global aerodinamik performansının tekil 'Sweep' ve 'lean' uygulamalarına göre daha başarılı olduğu görülmüştür fakat tekil geometrilerde görülen performans artışlarının toplamından daha küçük bir artış olduğu vurgulanmıştır. Bu durum üç boyutlu örme methodlarının aerodinamik performans üzerindeki etkilerinin lineer olarak kombine edilemediğini göstermektedir.

1. INTRODUCTION

1.1 Aim of the Thesis

It is aimed to investigate the influence of three-dimensional stacking, namely sweep and lean, on the aerodynamic performance of a transonic compressor blade. The investigation has been performed based on a 3D Reynolds Averaged Navier-Stokes solver and with a transonic axial compressor rotor.

1.2 Transonic Axial Compressor

The axial compressor technology has been used widely in gas turbines for years, mostly in aircraft engines. The state-of-the-art gas turbine engine technology tends to have compact designs to be compatible in the market which necessitates module design with superior loadings.

The technology shows a tendency to the transonic high pressure compressor designs that are efficient while having a reasonably high operational range. Having competitive efficiency levels is crucial while satisfying compactness and operability requirements. The efficiency improvement of %1 may reduce the SFC up to %1. (Obrecht, 2012)

Transonic axial compressors are commonly used in the industry today. Usually, the front stages feature transonic blade rows that have rotor tip Mach numbers up to 1.2, while some much higher levels have been applied successfully as GE E3 core compressor. (Calvert & Ginder, 1999) The modern axial compressors achieve a total pressure ratio up to 1.8, by the combination of the high tip speed and high work coefficients in the order of unity. (Biollo & Benini, 2011)

On the other hand, the transonic regime creates additional design aspects that need to be carefully done, mainly the shock system that includes bow and passage shock, and shock related loss mechanisms like intense interaction of the shock/boundary layer. (Domercq, 2012)

1.3 Supersonic Flow Regime for Transonic Axial Compressors

The aerodynamic characteristic of a supersonic rotor section can be divided into three main parts: choke, peak efficiency and near stall. (Figure 1.1) The choke case consists of a bow shock attached to the leading edge and a normal passage shock at diverging part of the airfoil near the trailing edge.

The peak efficiency case is formed for maximum deceleration through bow shock, before normal shock. It forms as the bow shock and passage shock merge on the suction side around the throat. Delta form is seen for peak efficiency case.

Further throttling pushes passage shock and the merged shock structure formed. The shock is expelled up to an unstable point, which drives the stall margin of the section. (Domercq, 2012)

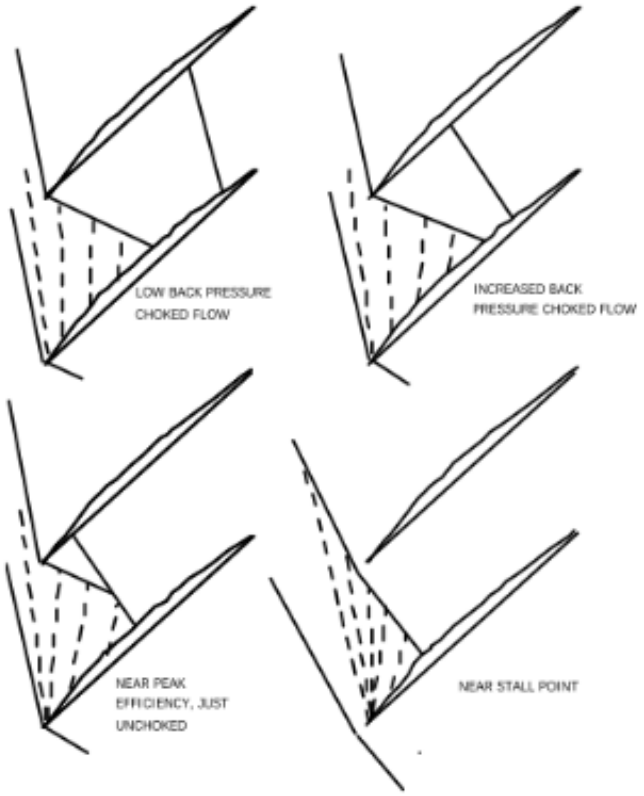

Figure 1.1 : Generic shock patterns of a transonic fan [Denton&Xu, 2002]

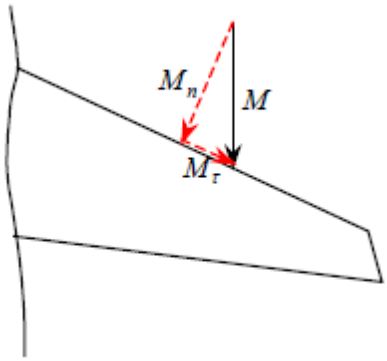

Figure 1.2 : Sweep application on wings [Ji et al., 2005]

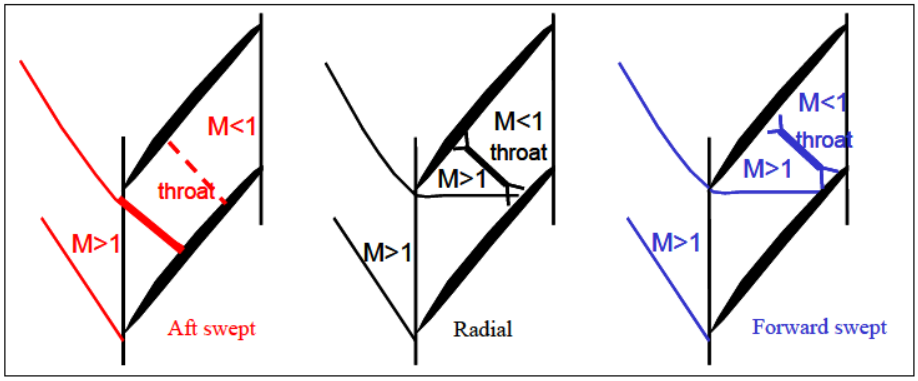

Figure 1.3 : Effect of the sweep on the shock pattern on transonic axial compressor [Domercq, 2012]

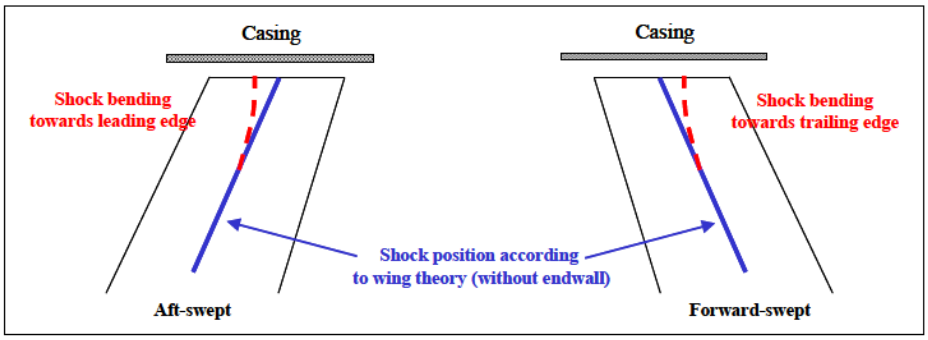

Figure 1.4 : Effect of the sweep on the shock intersection at casing [Domercq, 2012]

The shock structure of a blade section directly determines its working condition. A design Degree-of-freedom to control shock structure is 3-D stacking methods, namely sweep and lean.

1.4 Three-Dimensional Stacking Approaches

The most common 3-D stacking method that is used in turbomachinery applications is the sweep technique. The sweep strategy has been widely used in wing design to reduce mach number in perpendicular direction. (Figure 1.2) However, the transonic compressor sections are formed by a bow and passage shock, which requires additional design aspects.

One of the outstanding theories about the mechanism of the sweep in turbomachinery applications is stated by Domercq(2012). The shock intersection at the casing is seen to conserve its perpendicularity regardless of the stacking characteristics. This perpendicularity forces shock to relocate for swept blade designs. The relocation of the shock system redefines the working condition of the blade section. This mechanism gives a DOF to the blade section design. (Figure 1.3 & Figure 1.4)

Another 3D stacking method that is used in turbomachinery applications is the lean technique, also known as dihedral or bow depending on the spanwise distribution. Lean strategy is commonly used for state-of-the art vane designs, which allow spanwise redistribution of the load. The negative lean pushes flow to the middle sections, which increases loading at the endwall. Vice-versa for positive lean. (Figure 1.5)

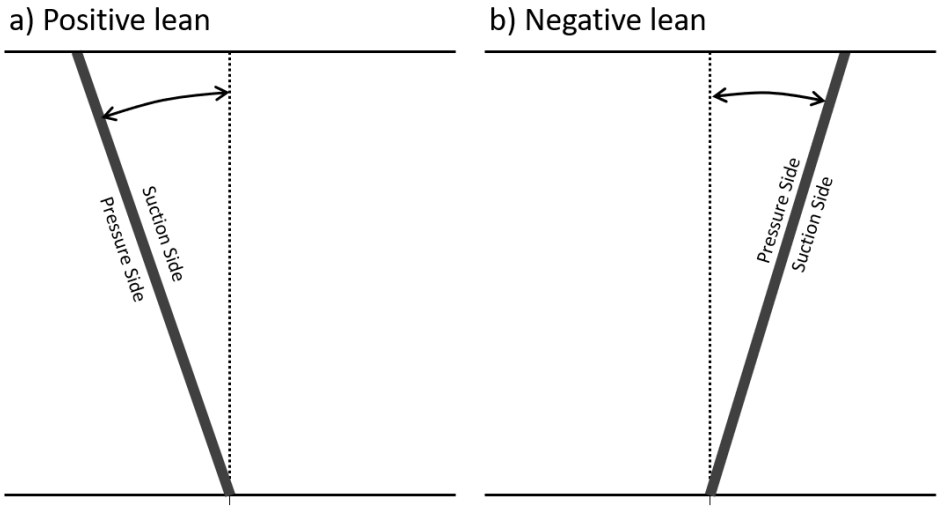

Figure 1.5 : Schematic of lean

1.5 Literature

Most of the studies regarding 3-D stacking approaches are seen to focus on low hub-to-tip ratio blades which are multistage fan applications. There are not many investigations performed for respectively higher hub-to-tip ratio blades that are suitable for high pressure compressors. Both experimental and numerical studies consist of investigation blades that are not only parameterized for 3-D stacking but also parameterized with 2-D profile properties such as chord and stagger. Additionally, the recent sweep and lean studies mainly aim to the optimizing blade shape with given free parameters through numerical approaches.

The very initial design attempts of the sweep in axial compressor date back to the 1950 and 1970s. The early studies were based on analytical approaches and low-speed test campaigns. The forward-swept blades were not ready to test in terms of structural integrity in that phase. The only testable aft-swept designs were not promising any improvement though. (Ji et al., 2005)

Further research showed some aft-swept designs that are beneficial in different aspects. One of them states that noise reduction can be achieved by aft-swept blade design, within NASA's research program including design and testing. (Hayden et al., 1977) Another paper by Hah(1990) reported the improvement of the peak efficiency with aft-sweep relative to the initial geometry with a stability penalty.

Wadia et al. (1998) reported an experimental and analytical investigation. The study includes both forward and aft swept low hub-to-tip ratio fan stages. The investigated geometries rearranged not only stacking but also barreling, which is a redistribution of the chord. It is shown that the forward-swept rotor achieved the highest peak efficiency while having operability improvement. On the other hand, the aft-swept rotor is shown to have adversely affected stall margin.

A study that aims to find optimal rotor geometry in terms of isentropic efficiency was reported by Jang et al. (2006) The response surface method has been used with design variables of sweep, lean and skew reported. NASA Rotor 37 was used as the initial geometry for the optimization study. The optimum geometry captured as aft swept, leaned through rotation direction at the tip with a skew characteristic.

Benini & Biollo (2007) performed a systematic numerical investigation of axially swept and tangentially leaned blades based on NASA Rotor 37. Among all parametric

geometries, a total of 26, the aft swept one has been shown to be 0.6% more efficient compared to the baseline. Also, the forward-leaned one, which is leaned through rotation direction, has been shown to have a 1.2% efficiency improvement.

An optimization study presented by Okui aims to improve isentropic efficiency while having unchanged stability. (Okui et al., 2011) A multi-objective numerical optimization was performed with the free variables of the sweep, chord length and the camber distribution. A typical front stage transonic rotor is used for investigation. The outcome of the optimization process shows a rotor having a strong backward sweep stacking line with a barreling chord at mid sections.

Another optimization study based on NASA Rotor 67 has been reported by Aziz et al. (2014) The optimum stacking has been reported as a forward sweep at the hub-mid section and a negative sweep at the mid to tip. Also, optimized blade lean is slightly positive at the hub and tip, and negative at the middle section. The final geometry has a %2.2 isentropic efficiency improvement.

Sun et al. (2020) investigated an ultra-high-load LR transonic compressor stage with 5 different axially forward swept configurations, which includes true lean because of axially swept geometries. For all the geometries, the stall margin has been improved whereas the maximum improvement is %15. The change in stall margin because of the forward sweep is associated with the tip flow field improvement. The shock structure and tip leakage vortex are seen to be improved with forward sweeping.

Wang et al. (2021) published an optimization study with free parameters of sweep and lean based on NASA Rotor 35. The optimized blade is modified to be forward swept along the radial direction, especially from the midspan to the tip, and modifications of the forward sweep are also performed in the bottom half but to a lesser degree. Also, the optimum blade consists of lean characteristics in the rotation direction at the tip and vice versa at the hub. The peak efficiency improved to 85.01% from 84.45% whereas the stall margin improved to 20.07% from 16.11%. It is seen that the intensity of the tip vortex at stall conditions can be reduced by changing the position and intensity of the shock wave.

2. NUMERICAL APPROACH

2.1 NASA Rotor 37

A series of investigation studies conducted by Reid and Moore (1978a) at NASA Lewis Center included throughflow design and experimental effort. The study aimed to investigate the state-of-the-art core compressor designs that are highly efficient while having a reasonably high operational range. The front, middle, and rear single-stage characteristics of an eight-stage core compressor with 20 OPR were planned to investigate separately.

Within the scope of this study, four different single stages, namely stage 35-36-37-38, that are designed as a front stage have been reported in terms of throughflow design details and performance characteristics evaluated by experimental studies. (Reid & Moore, 1978a & 1978b)

Figure 2.1 : NASA Rotor 37 Geometry

Stage 37 is a well-known benchmark case in the numerical turbomachinery literature. It is designed with MCA (multiple-circular-arc) blading for a design pressure ratio of 2.1. It consists of 36 blades with a 1.19 aspect ratio. The design RPM of Stage 37 is 12188.7 RPM which corresponds to 454.14 m/s tip speed. The summary of the design specifications of the NASA Stage-37 is given in Table 2.1.

Table 2.1: NASA Rotor 37 Design Specifications

Blading	Multiple Circular Arc
Number of Blades	36
Hub to tip ratio	0.7
Running tip clearance	0.356 mm
Design Speed	17188.7 RPM
Tip speed	454 m/s
Total Pressure Ratio	2.106
Polytropic Efficiency	0.889

The geometrical dataset as manufacturing coordinates is given by Reid and Moore (1978a). However, it has been figured out that the transition analysis of intended hot geometry to manufacturing cold geometry was not successfully done, resulting as miss prediction of twist angle up to 2°. Complex analysis methods to calculate blade deflections were not present at the time, which is a reasonable factor behind the discrepancy. (Suder, 1996)

The experimental setup details, including survey locations, running tip clearance, spanwise inlet profiles, turbulence intensity, rotating and non-rotating endwall locations and blade fillets are given by the AGARD Report. (Dunham, 1998)

The experimental outputs of Stage 37 are published by Reid and Moore (1978a), while detailed flowfield results of Rotor 37 were given by Suder (1996).

The NASA Rotor 37 (Figure 2.1), which is the rotor blade of Stage 37, has been used for validation and further investigation studies in this paper.

2.2 Grid

The grid generation has been performed with commercial code AutoGrid5, which is a turbomachinery dedicated automatic grid generator based on structured hexahedral elements. O4H type blade-to-blade mesh topology, an O-block around the blade surface (1) and four H-blocks to inlet (2), outlet (3), upper (4) and lower (5) periodic sides, has been applied. (Figure 2.2)

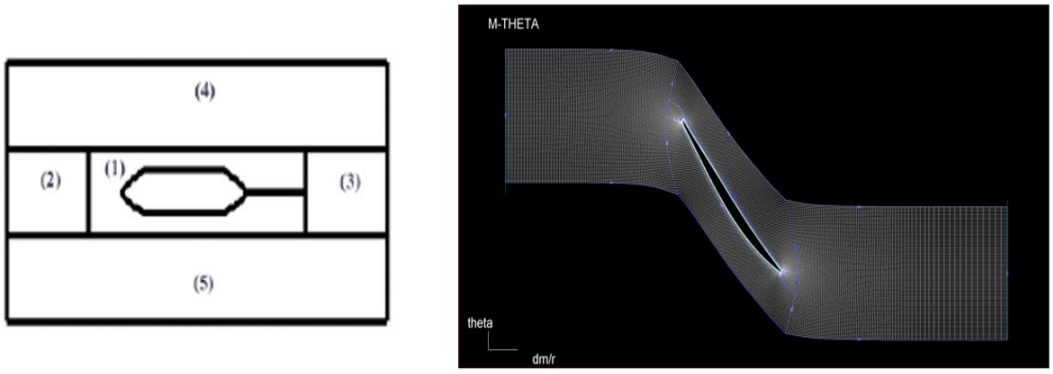

Figure 2.2 : Blade-to-blade mesh block

Near endwall features, including hub fillet and tip clearance have been modeled with additional blocks dedicated to these features. A fair number of radial elements have been generated at tip clearance and fillet blocks (Figure 2.3), to capture reasonable y+ and tip leakage vortex which is quite complex.

Due to the periodicity of turbomachinery nature, a single passage with periodic matching surfaces has been generated. (Figure 2.4)

The first cell height is selected around 1 micron to capture a y+ distribution around 1. A contour representation of the y+ distribution on the blade surface is given in Figure 2.5 with a contour range of up to 1. It is seen that even for the suction surface the average y+ distribution is adequate for modeling any possible separation flow.

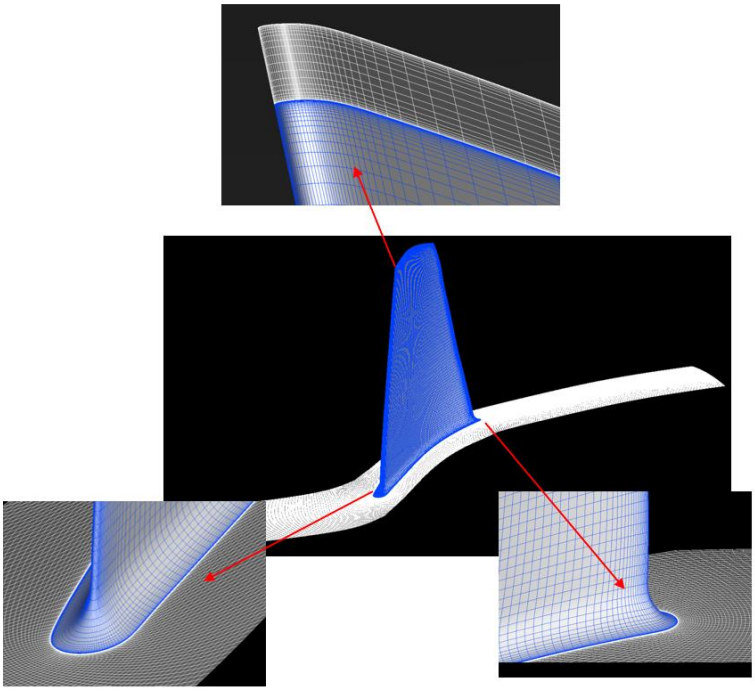

Figure 2.3 : Featured mesh blocks

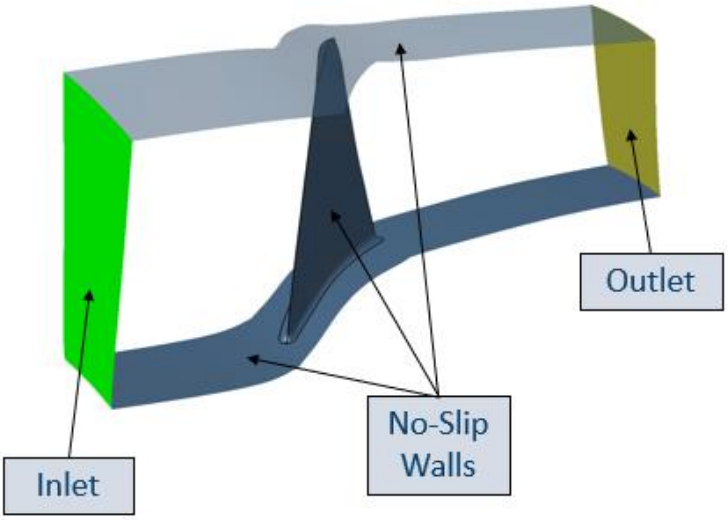

Figure 2.4 : Single blade row model

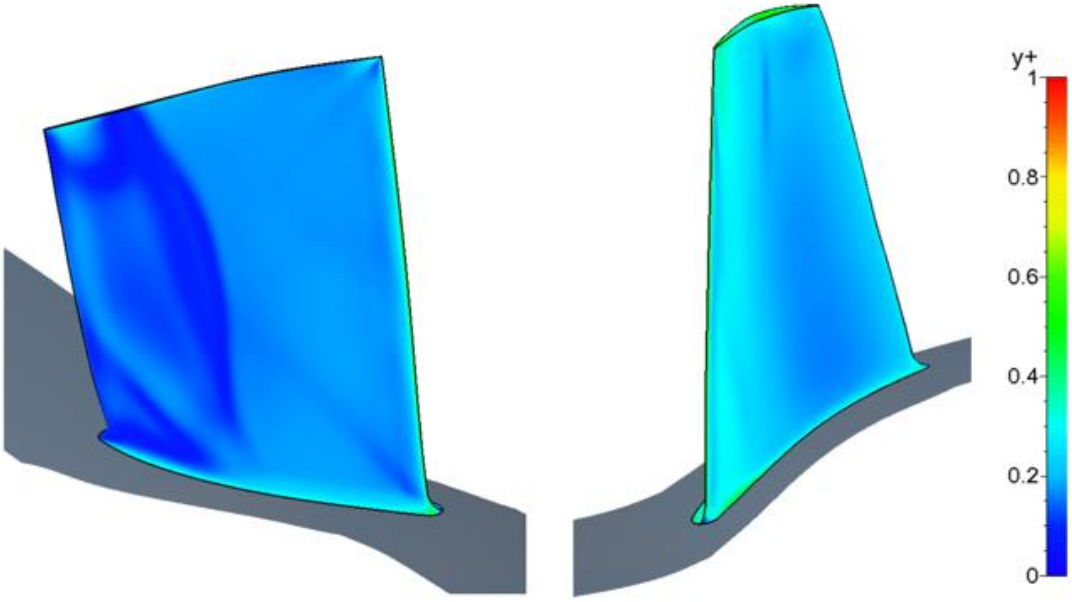

Figure 2.5 : y+ contour on blade surface

2.3 Solver

The CFD analysis has been performed with commercial code FineTurbo (Euranus solver), which is a turbomachinery dedicated state-of-the-art flow solver. Reynols-Averaged-Navier-Stokes approach with the Spalart-Allmaras turbulence model has been applied, which is shown in the literature to be a successful model to calculate

characteristics for turbomachinery problems. The single passage is taken into account due to 1/36 periodicity. Fourth order Runge-Kutta integration scheme has been applied for temporal discretization. Cell-central spatial discretization scheme has been applied. Three orders of magnitude global residual and 0.02% mass flow error between inlet and outlet are satisfied as convergency criteria.

The back pressure increased systematically during performance characteristics investigation up to 500 Pa difference. The last numerically stable point is referred as near stall solution in this paper.

2.4 Boundary Conditions

The hub, blade and shroud surfaces are modeled as no-slip walls. Also, the rotating part of the hub surface is carefully dictated as presented in the AGARD Report. (Dunham, 1998) A schematic of the applied boundary conditions is given in Figure 2.6.

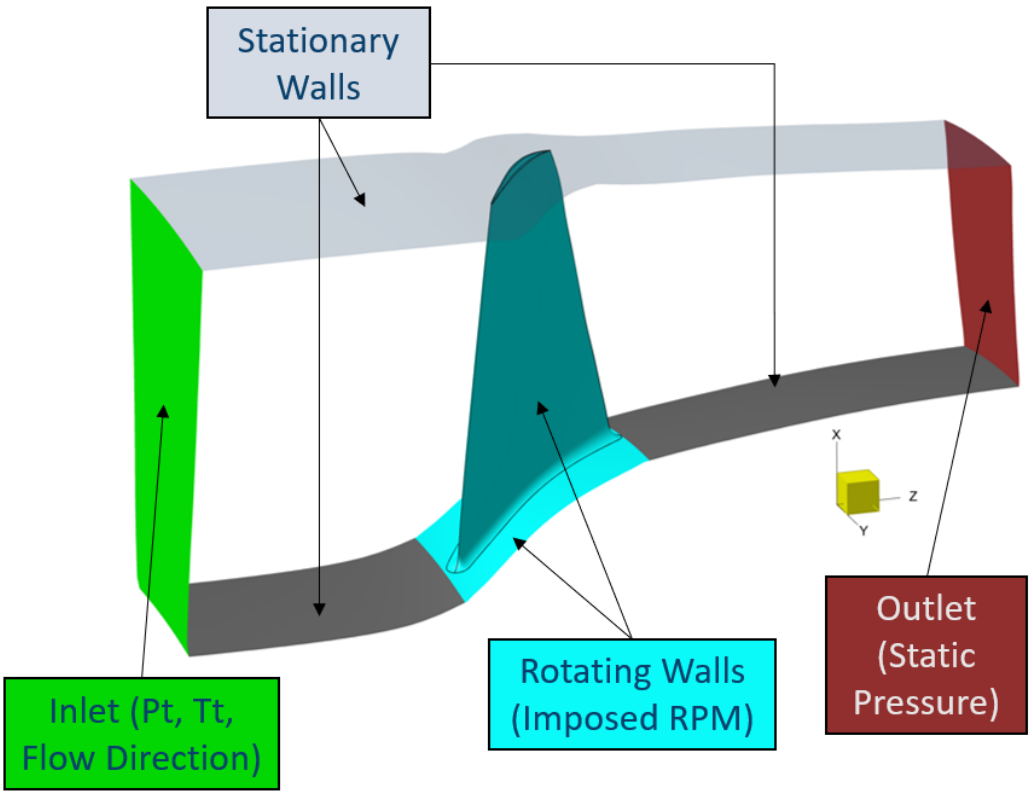

Figure 2.6 : Schematic of applied boundary conditions

The thermodynamic boundary conditions presented within the AGARD report (Dunham, 1998) have been used for the model. The spanwise total pressure and total

temperature profiles have been imposed on the inlet surface as a one-dimensional profile. (Figure 2.7) The inlet flow direction has been imposed as axial flow. The average static pressure is imposed on the outlet surface and has been systematically modified during the evaluation of performance and efficiency characteristics.

The turbulence boundary condition for a turbomachinery problem is known to be vital. However, there is no turbulence data reported for experimental studies of NASA Rotor 37. There are different approaches to the interpretation of the inlet turbulence level of the test rig based on the turbulence intensity and length scale or turbulent viscosity ratio. Shabbir, Zhu&Celestina (1996) presented a numerical solution that is compatible with experimental results, which includes the turbulent inlet boundary condition as a turbulent viscosity ratio of 100. This approach has been applied to the model.

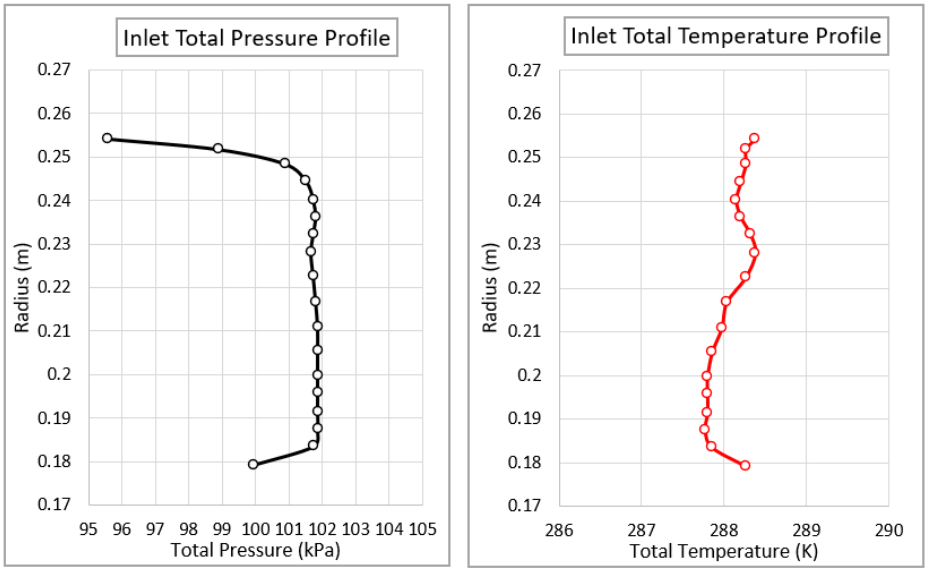

Figure 2.7 : Applied inlet boundary condition profiles

2.5 Mesh Independency

The mesh independency study has been performed with four different grid structures. 3.34, 1.34, 0.56 and 0.28 million mesh elements are used for grids, respectively named as ultra fine, fine, medium and coarse mesh. (Table 2.1) The scaling factors have been applied to all the topology elements, such as B2B, spanwise, tip clearance, and fillet meshes.

The comparison of global performance outputs has been given with a performance map in Figure 2.8 and Figure 2.9, including experimental data published by Reid and Moore (1978a).

Table 2.2: Grid Properties

	Number of Elements	Minimum Skewness	Max Aspect Ratio
Ultra Fine	3,343,285	14.8	2400
Fine	1,137,477	13.3	3300
Medium	561,113	18.3	4200
Coarse	288,777	14.5	5600

The performance map comparison shows that the stall margin is overpredicted for all meshes. The deviation of the pressurization characteristics at the part speed is less, but vice-versa for efficiency. The efficiency characteristic at design speed is well captured for all mesh configurations. It is seen that the flow capacity at the choke condition is well captured for all the mesh configurations. Also, main pressurization and stall margin characteristics show similar behavior, compatible with experimental results.

The numerical solution referred as the design point hereafter has been picked to be on the identical beta line with the given experimental data. Beta lines are auxiliary coordinate approaches used for component matching. (Kurzke, 1996)

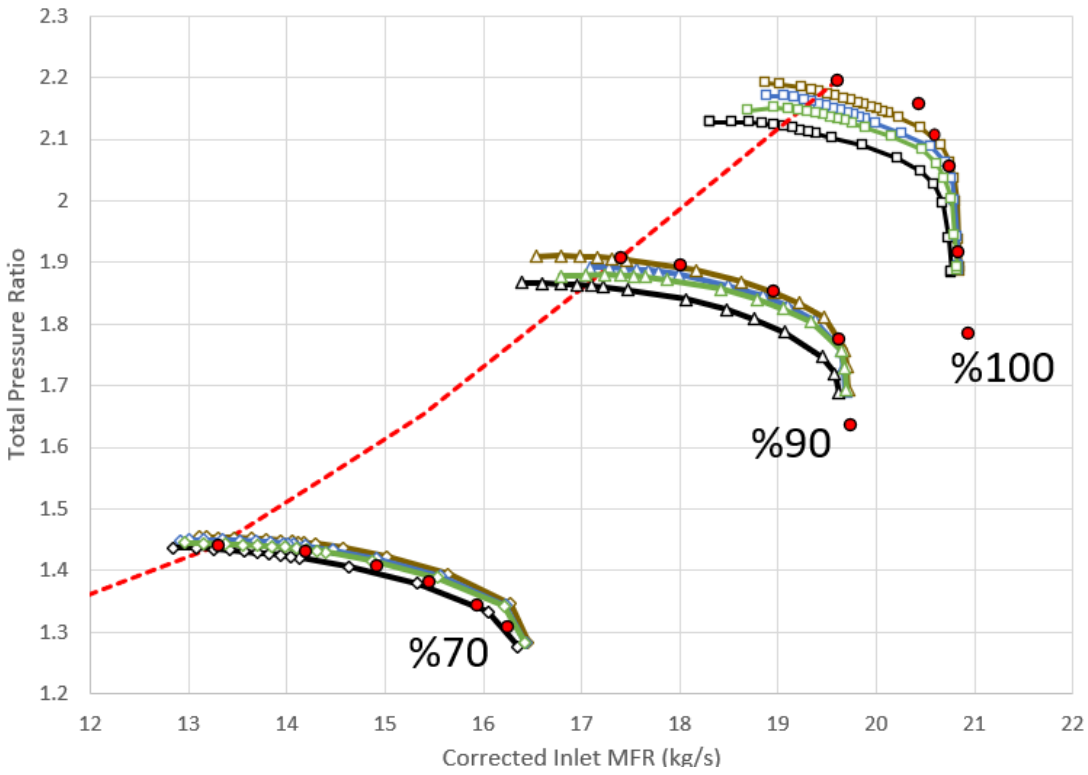

Figure 2.8 : Pressure map of different grid size approaches

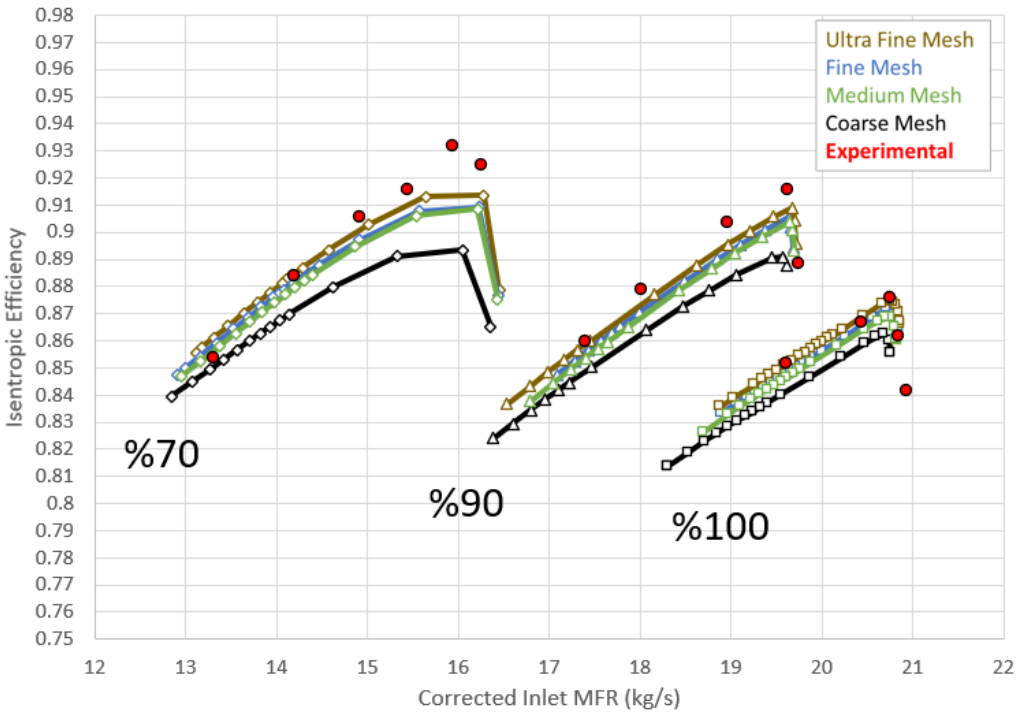

Figure 2.9 : Isentropic efficiency map of different grids

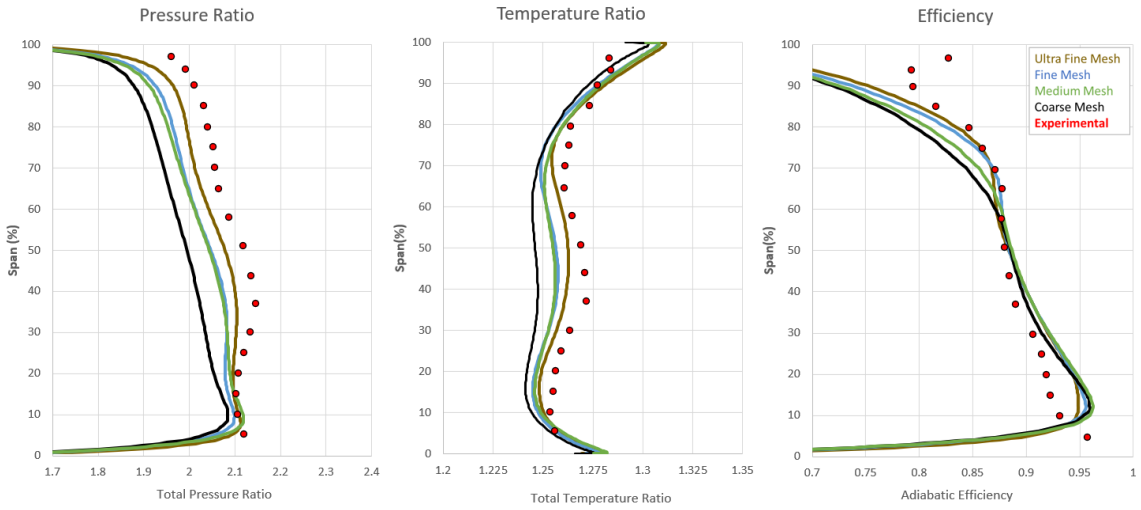

Figure 2.10 : Comparison of the spanwise flow properties of different grids

Another available experimental data that can be used for mesh independency study is one-dimensional exit profiles of Rotor 37. (Suder, 1996) The spanwise exit profiles of Rotor 37 at the design point (%100 RPM) and the CFD result comparison of different grids are given with Figure 2.10. The profiles represent the mass-weighted average through the azimuthal direction. It should be noted that the radial migration of the

stream tubes, which is expected not to be extreme, was not included in the calculation of the radial distribution of flow properties.

It is seen that the total pressure ratio prediction of the numerical model is with experimental results in terms of its characteristics. However, the calculation of the design point based on the approximate beta line leads to a slight shift in the pressure ratio values.

The compatibility of the total temperature ratio is similar to pressure ratio characteristics mainly. Additionally, the deviation of the temperature ratio at the tip section is respectively high which might reflect the overprediction of the tip vortex mechanisms.

The efficiency characteristic, which reflects both total pressure ratio and total temperature ratio characteristics, is compatible with fine mesh except in two regions: (1) It is seen that the losses are overpredicted at the near end-wall at the tip; (2) it is seen that the calculated values are slightly higher than experimental data at near to the hub, which shows underprediction of the losses.

In general, the modeled spanwise characteristic is compatible with experimental data.

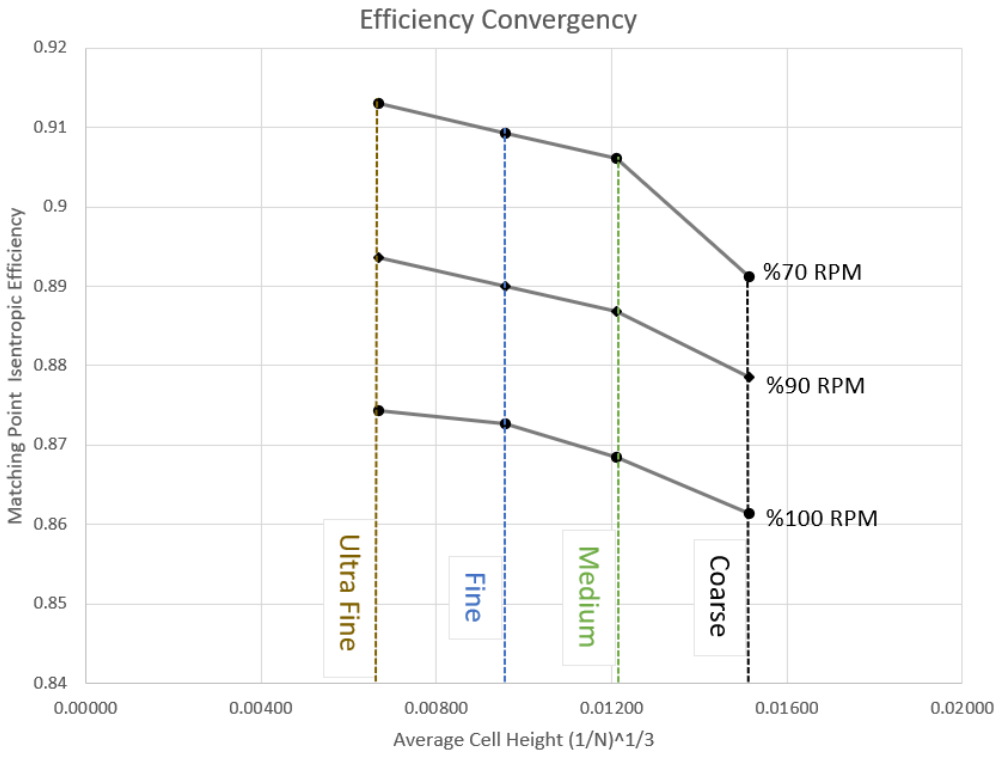

Figure 2.11 : The convergency of the isentropic efficiency over average cell height

A convergency rate based on design point efficiency has been given in Figure 2.11, within the scope of Roache (1998). The horizontal axis represents the height of an average cell element. The zero value on this axis represents an infinite number of elements. The convergency behavior is seen with decreasing slope of isentropic efficiency. It is assumed that the increment of mesh density after *Fine Mesh* can not create any significant improvement in model prediction so the *Fine Mesh* has been selected for future validation and investigation studies as a reasonable trade-off point between accuracy and numerical cost.

2.6 Validation

A comparison of blade-to-blade flow field of CFD and experimental result at the design point (Suder, 1996) is given in Figure 2.12. It is seen that the main shock characteristics, shock&BL interaction have been well captured and similar to experimental results. The upstream relative Mach number of bow shock is captured as 1.4, similar to experimental data. The acceleration at the upstream of the bow shock around suction side is slightly higher (up to Mach 1.5) at CFD case, which can be seen at the Figure B.2. The similar acceleration behavior captured in the passage at the downstream of the passage shock. The wake region is slightly wider at CFD case.

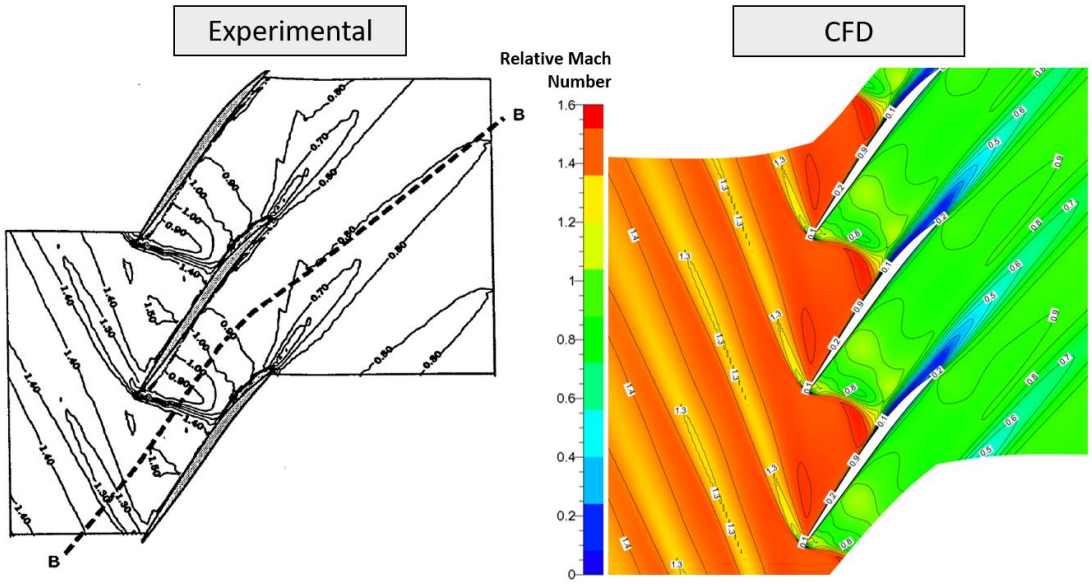

Figure 2.12 : Comparison of Design point B2B plane at %70 Span

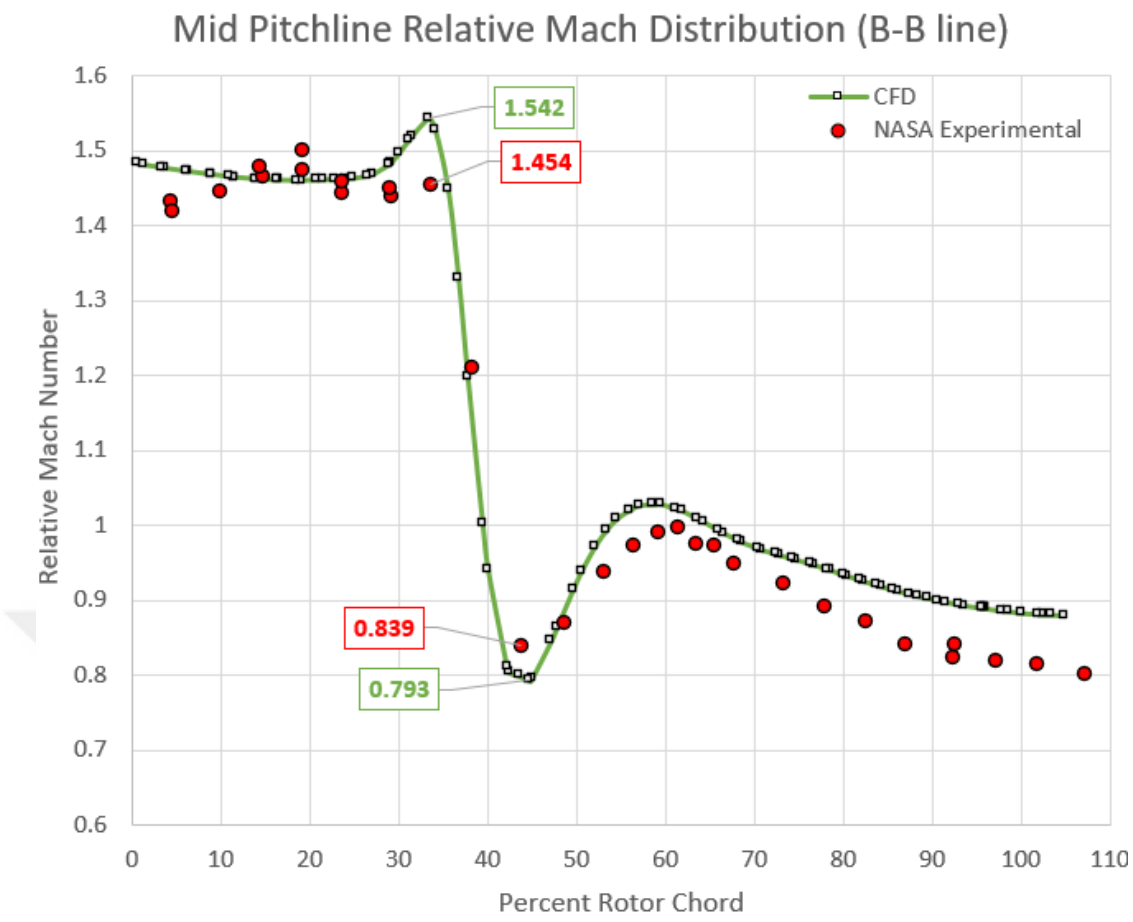

Figure 2.13 : Mid pitchline relative mach distribution

Another available experimental data (Suder, 1996) is the relative Mach number distribution on the mid-pitch line, which was given in Figure 2.12 as the B-B line. The mid-pitchline relative Mach distribution (Figure 2.13) shows that the passage shock has been slightly overpredicted, which can be interpreted from higher inlet Mach number at the inlet, and less Mach number at the outlet for the CFD solution. The fluctuation at the near leading-edge region up to shock is predicted as the averaged characteristic of experimental results by the numerical model. The outlet relative Mach number is slightly higher, which may be related to the wider wake region seen on the CFD model.

Mainly, the numerical model seems to be capable to represent the experimental case and can be used for further investigations.

3. SWEEP AND LEAN INVESTIGATIONS

In this section, the NASA Rotor 37 is manipulated in terms of sweep and lean and the flow field has been investigated with the validated numerical method given in Section-2.

3.1 Sweep and Lean Geometry Definitons

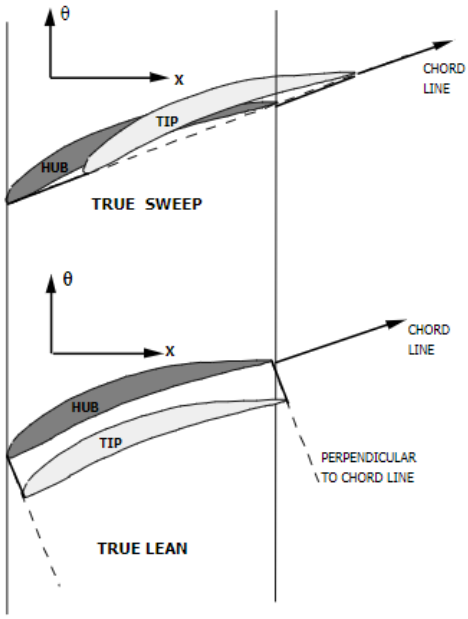

Figure 3.1 : True sweep and Lean definitions [Denton & Xu, 2002]

There are different sweep and lean approaches practiced in turbomachinery applications. One of them is true sweep and true lean given by Denton & Xu (2002) (Figure 3.1), which are a movement of the airfoil section in the direction of the chord line and perpendicular to the chord line, respectively.

Another common definition of sweep and lean is the movement of the airfoil sections according to cylindirical coordinate frame. This approach can be summarized as sweeping through the axial direction and leaning through the tangential direction. Axial sweep and tangential lean approaches have been used in this paper. The details of the stacking definitions are given below passages.

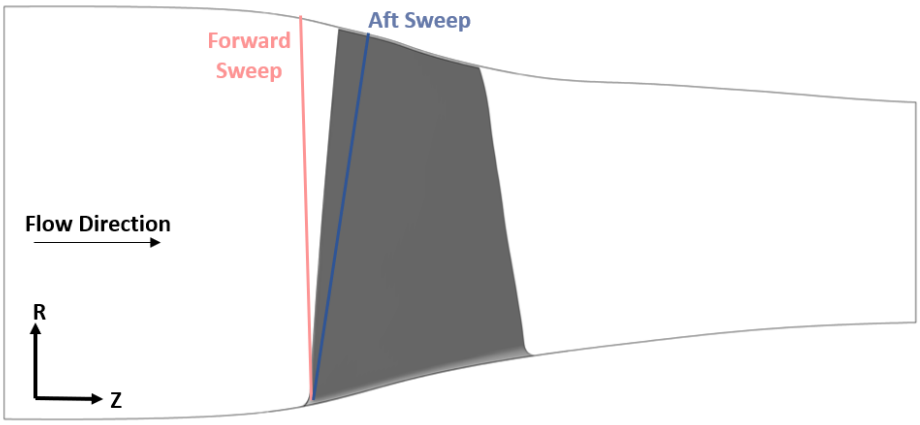

Figure 3.2 : Meridional view of sweep definition

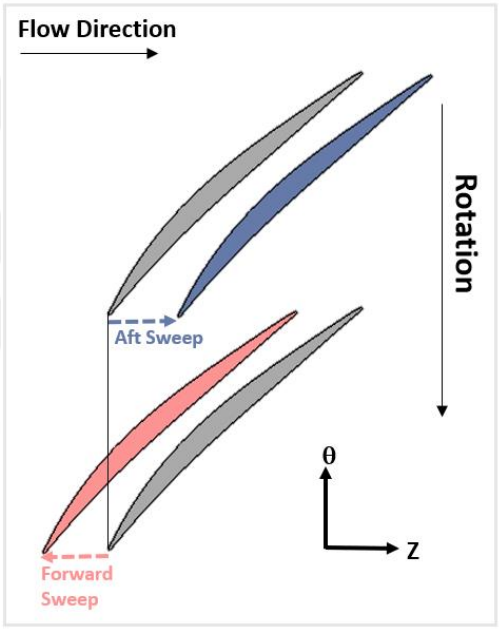

Figure 3.3 : Blade-to-blade view of sweep definition

The forward (positive) sweep is defined as an axial offset into the leading edge along z-axis; while the aft (negative & backward) sweep is defined as an axial offset into the trailing edge along z-axis. The schematic explanation of the sweep definition has been given in Figure 3.2 and Figure 3.3 through meridional and blade-to-blade perspectives.

The positive lean is defined as circumferential rotation towards the rotation direction of the rotor through the tangential direction. The negative lean is defined as circumferential rotation towards the opposite rotation direction of the rotor along the tangential direction. The schematic explanation of the lean definition has been given in Figure 3.4 and Figure 3.5 through meridional and blade-to-blade perspectives.

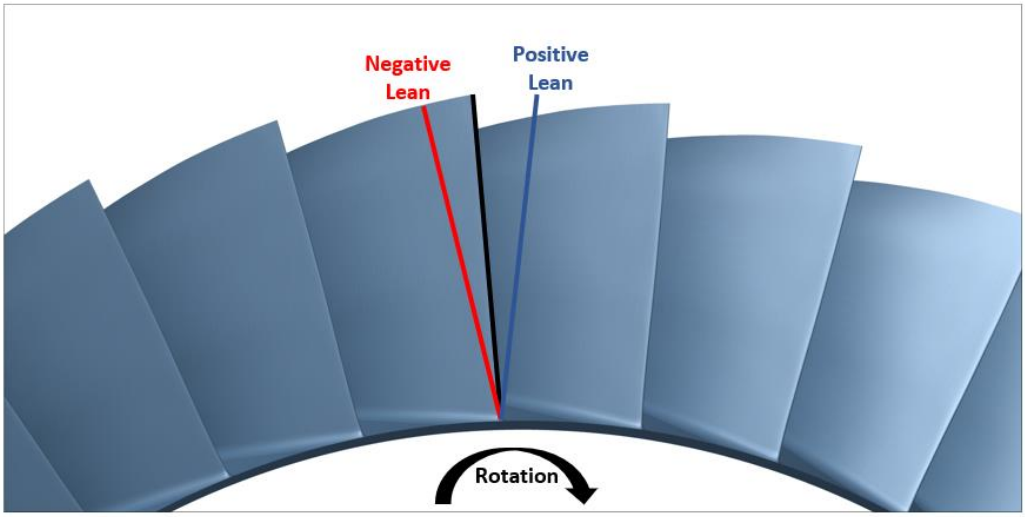

Figure 3.4 : Front-looking-aft view of the lean definition

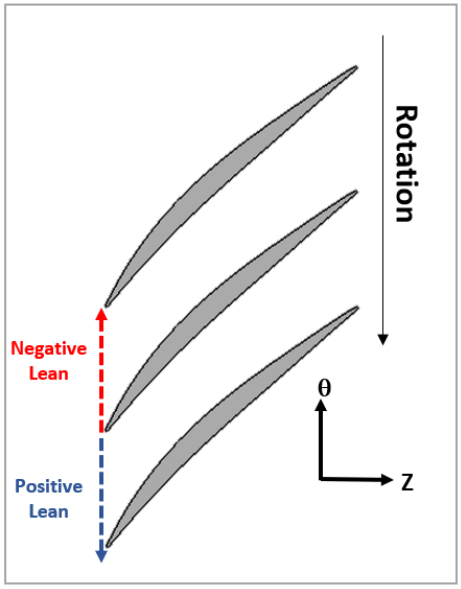

Figure 3.5 : Bade-to-blade view of lean definition

Another important aspect of the 3D stacking method is the spanwise distribution. In the case of the assumption of being independent sections, the application of the sweep and lean might lead blade surface curvature to highly fluctuate which is not suitable in terms of manufacturability and structural integrity. Also, it may challenge the discretization of the surface. Thus, the spanwise smoothness of the blade structure is a key factor in blading in terms of both numerical approach and manufacturing. In this paper, two type spanwise distribution methods have been applied during the generation of the investigation geometries, which are linear and bezier type distributions. The details of spanwise distribution methods are given in Appendix-A.

3.1.1 Sweep geometries

A total of 4 different investigation geometries have been created with different sweep approaches including both forward and aft sweep. (Figure 3.6) Two of them have linear type radial distribution and the rest of them have bezier curve distribution.

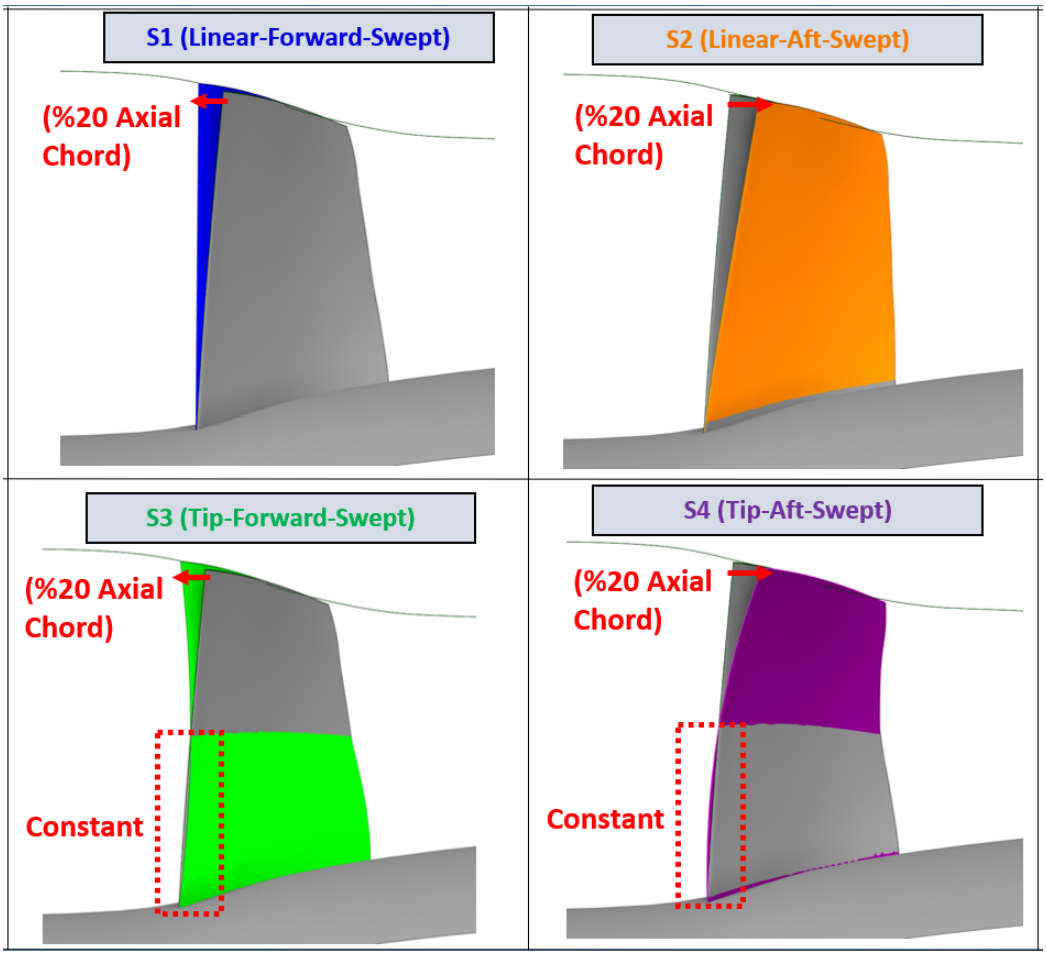

Figure 3.6 : Details of swept geometries generated

The S1 (Linear-Forward-Swept) configuration has a linearly distributed forward sweep which corresponds to a shift %20 of the axial chord at the tip section. The S2 (Linear-Aft-Swept) configuration has similar linear characteristics with S1 but in the opposite direction, which is an aft-swept blade.

The S3 (Tip-Forward-Swept) has a similar shift amount with the S1 configuration but its forward sweep characteristic mainly exists above mid-span thanks to bezier type spanwise distribution. The S4 (Tip-Aft-Swept) configuration has similar characteristics with S3 but in the opposite direction, which is an aft-swept blade. The hub-to-mid sections of the S3 and S4 configurations were kept constant as much as possible.

3.1.2 Lean geometries

A total of 4 different investigation geometries have been created with different lean applications. (Figure 3.7)

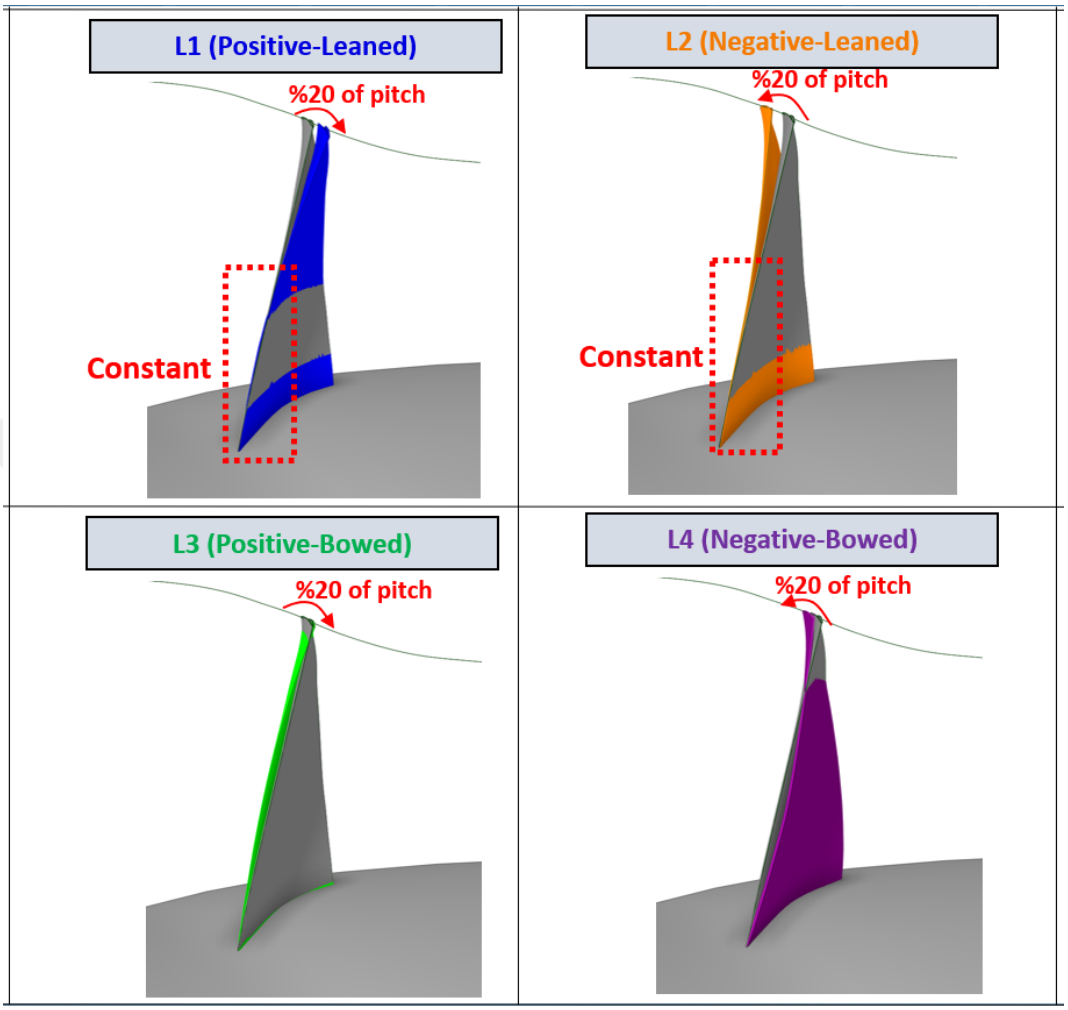

Figure 3.7 : Details of leaned geometries generated

The L1 (Positive-Leaned) configuration has a positive lean which corresponds to a rotation of %20 pitch distance at the tip section while keeping the hub-to-mid section constant. The L2 (Negative-Leaned) configuration has similar characteristics with L1 but in the opposite direction, namely negative lean. The hub-to-mid sections of both L1 and L2 configurations were kept constant as much as possible within the bezier curves' limitations.

The L3 (Positive-Bowed) has a similar rotation amount with the L1 configuration but its positive lean characteristic has been distributed spanwisely thanks to bezier type distribution. The L4 (Negative-Bowed) configuration has similar characteristics with L3 but in the opposite direction, namely negative-bowed.

3.2 Global Performance Results

The working point of a compressor on the performance map is determined by the performance cycle as compatible with the matched turbine. The determination of the design point is important to compare different designs' performance. A useful method to determine the matching point is using β-grid lines. (Kurzke, 1996) The comparison points given in this paper were selected to be on similar β-grid lines as much as possible.

Sweep

The pressure and efficiency maps of the swept geometries have been given in Figure 3.8 and Figure 3.9. The linear spanwise distributed geometries are mentioned as the most swept case here and after because those configurations have more spanwise cumulative sections shifted.

Mainly, the characteristics are seen to move to higher flow areas with increasing sweep which also includes the deviation of the choke capacity, which is similar to reported by Cui et al. (2016). The choke capacity is seen to vary in the range of ±%2.5, which reflects the re-arrangement of the throat surface. It is seen that the peak pressure ratio varies in a narrow range. The aft-swept geometries have peak pressure ratio improvement.

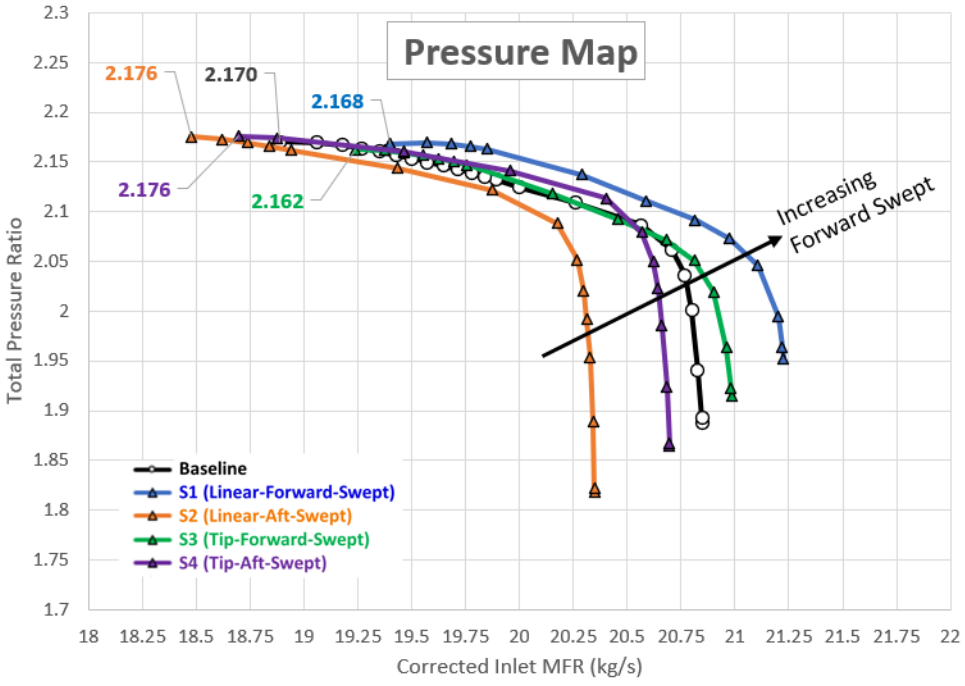

Figure 3.8 : Pressure map of the swept geometries

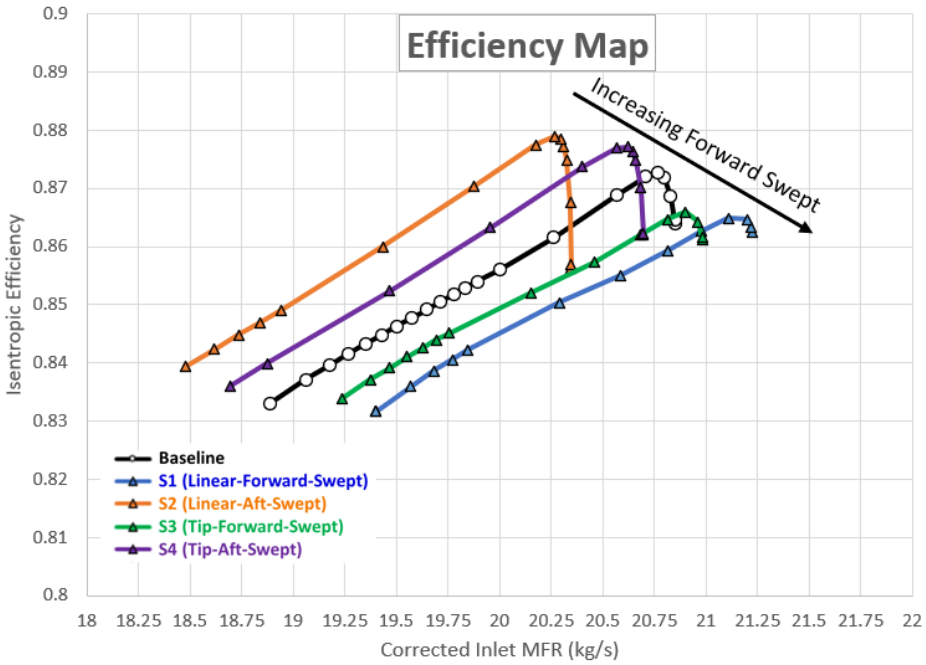

Figure 3.9 : Isentropic efficiency of the swept geometries

The peak efficiencies are seen to systematically decrease with increasing forward sweep. It can be interpreted that the main characteristic is driven by being forward or aft sweep because the peak efficiencies are seen to vary in a narrow range for individual sweep groups such as S1&S3 and S2&S4.

Also, the mass flow range between the peak efficiency point and the choke point decreases with increasing forward sweep which is a penalty in terms of efficient matching. If the blades are assumed to match the peak efficiency condition, the forward swept cases show less choking margin.

The comparison of the design point efficiency and stall margin of the swept geometries with baseline model has been given in Figure 3.10 and Figure 3.11. As mentioned before, the last numerically stable points referred as near-stall solutions and stall margins have been calculated based on this approach. The aft sweep configurations (S2 and S4) have stall margin improvement while the forward swept configurations has the stall margin deficit. The linear forward swept configuration (S1) has the most stall margin deficit, approximately %4 less stall margin. The tip-forward-swept configuration (S3) has a better stall margin compared to S1, but it is still less than the baseline. The most stall margin improvement is seen as %3 with linear-aft-swept at tip (S2).

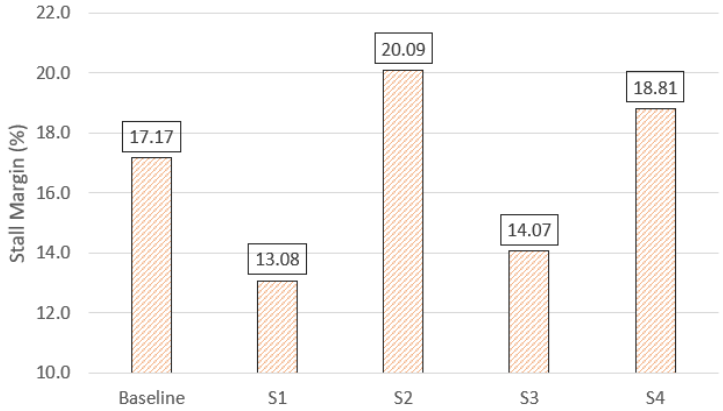

Figure 3.10 : Comparison of stall margins of swept geometries

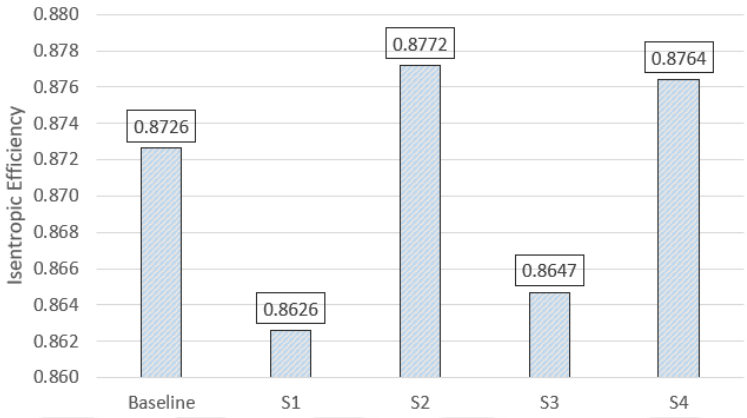

Figure 3.11 : Comparison of design point efficiencies of swept geometries

The forward-swept configurations, (S1) and (S3), have %1 less efficiency approximately, compared to the baseline solution. The efficiency deficit of the tip-forward-swept configuration (S3) is slightly less than the linear forward-swept configuration (S1). That reflects the behavior of the less span height of forward swept, the less efficiency deficit. On the other hand, the aft swept configurations, (S2 and S4), show efficiency improvement up to %0.5. The efficiency gain of linear-aft-swept (S2) configuration is slightly higher compared to tip-aft-swept configuration (S4), which also reflects the behavior of the less span height of aft swept, the less efficiency improvement.

Lean

The pressure and efficiency maps of the swept geometries have been given in Figure 3.12 and Figure 3.13. The characteristics do not vary in terms of choke capacity but the operability range has seen to change.

The choke capacity conservation reflects the conservation of the throat surface, too. It is seen that the peak pressure ratio varies in a narrow range except the L3 case. The positive leaned and positive bowed geometries have peak pressure ratio improvement compared to the baseline.

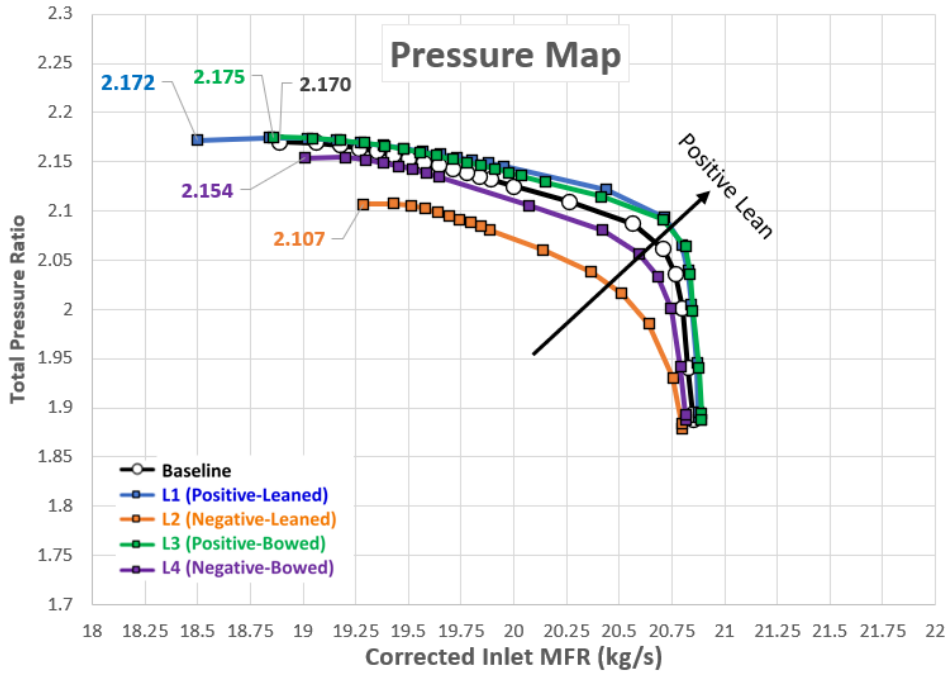

Figure 3.12 : Pressure map of the leaned geometries

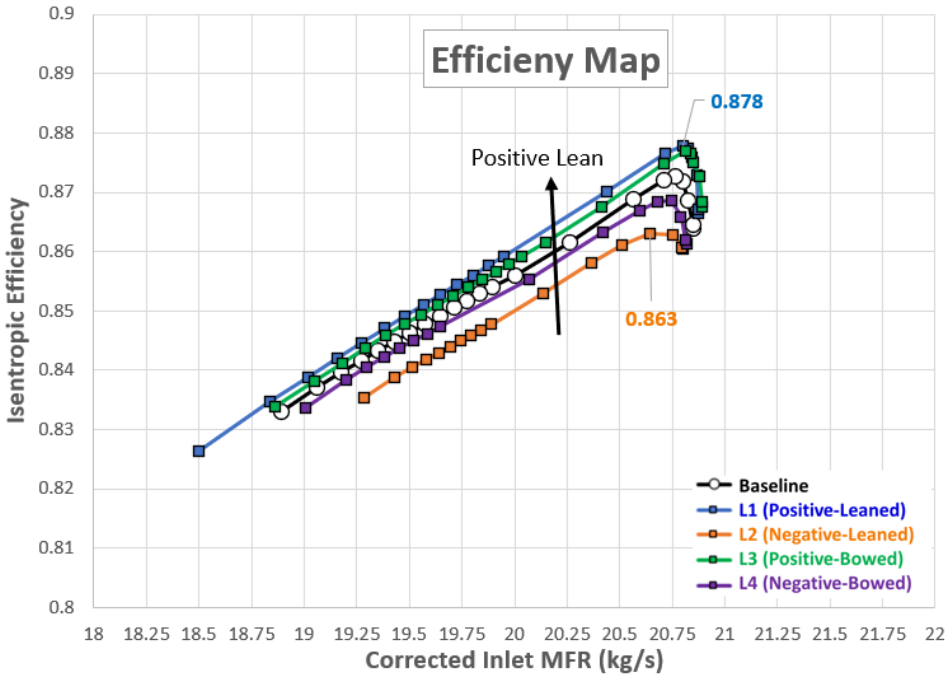

Figure 3.13 : Isentropic efficiency of the leaned geometries

The peak efficiencies are seen to systematically increase with positive lean as indicated by arrow in the map. Unlikely the sweep case, the mass flow range between the peak efficiency point and the choke does not change thanks to the conservation of the choke capacity.

The comparison of the design point efficiency and stall margin of the leaned geometries with baseline model has been given in Figure 3.14 and Figure 3.15. The positive-leaned (L1) and positive-bowed (L3) configurations have SM improvement while negative-leaned (L2) and negative-bowed (L4) configurations have stall margin deficit. The configuration L1 has the highest stall margin with a %2.75 improvement. The negative-leaned configuration (L2) is the worst in terms of operability, and has a %6 stall margin deficit, which was also seen on the performance map.

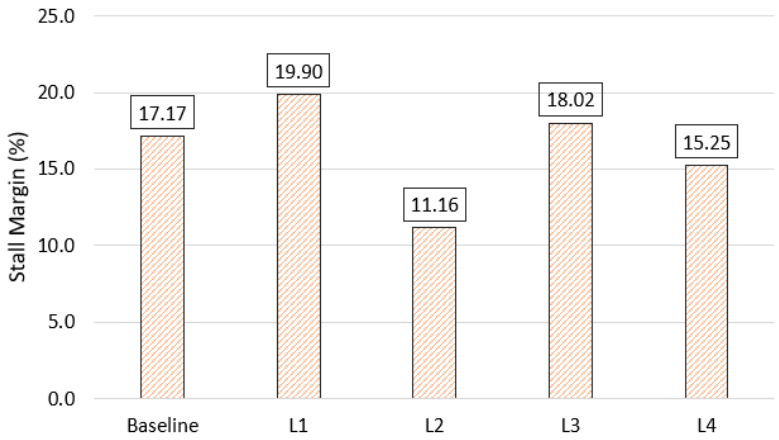

Figure 3.14 : Comparison of stall margins of leaned geometries

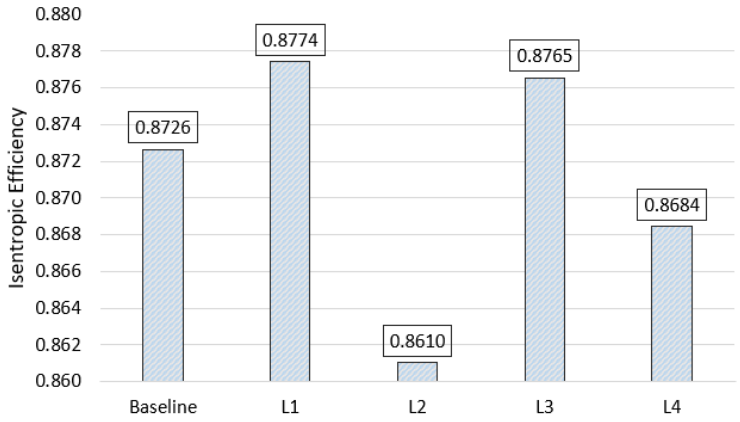

Figure 3.15 : Comparison of design point efficiencies of leaned geometries

The positive-leaned configurations (L1 and L3) have efficiency improvement, while negative-leaned configurations (L2 and L4) have an efficiency deficit compared to baseline. Configuration L1 has the highest efficiency with a %0.5 improvement. Also, the efficiency improvement of L3 is not far away from this value. The configuration L2 has the lowest efficiency with a %1.1 deficit. The overall results can be interpreted as the more span height for positive lean the more efficiency and operability improvement.

3.3 Spanwise Flow Field Results

In this section, spanwise flow properties are investigated systematically. The profiles have been calculated via a mass-weighted averaging approach in the azimuthal direction. The exit station is located on the axial location given within AGARD report (Dunham, 1998) as Station-4, where the experimental data is provided. (Appendix-C)

The near-stall solutions given in this section represent the last numerically stable solution that has converged.

Sweep

The spanwise total pressure ratio distribution at the design point (Figure 3.16) shows that forward-swept configurations (S1 and S3) have more pressurization on the tip section. On the other hand, the aft-swept configurations (S2 and S4) have less pressurization on the tip section which reflects that the forward and aft sweep applications create opposite behaviors on the pressurization feature. The overall shifting movement was observed within the performance map. The forward sweep shifts the map to the high flow and high pressure ratio region. The development of the total pressure ratio shifting is seen through the spanwise characteristics movement with a forward sweep.

The spanwise isentropic efficiency (Figure 3.17) at tip sections ranges in a narrow scale, unlikely to pressure ratio behavior at the tip section. The main difference of the isentropic efficiencies is located around the mid spans. The forward-swept configurations (S1 and S3) have less efficiency at the below %70 span. The aft-swept configurations (S2 and S4) have more efficiency at the below %70 span. The efficiency differentiation at the mid spans drives the global performance, which was given via

Figure 3.11. Briefly, it is seen that the forward sweep shifts the map to the less efficient direction, and vice-versa for the aft sweep approach.

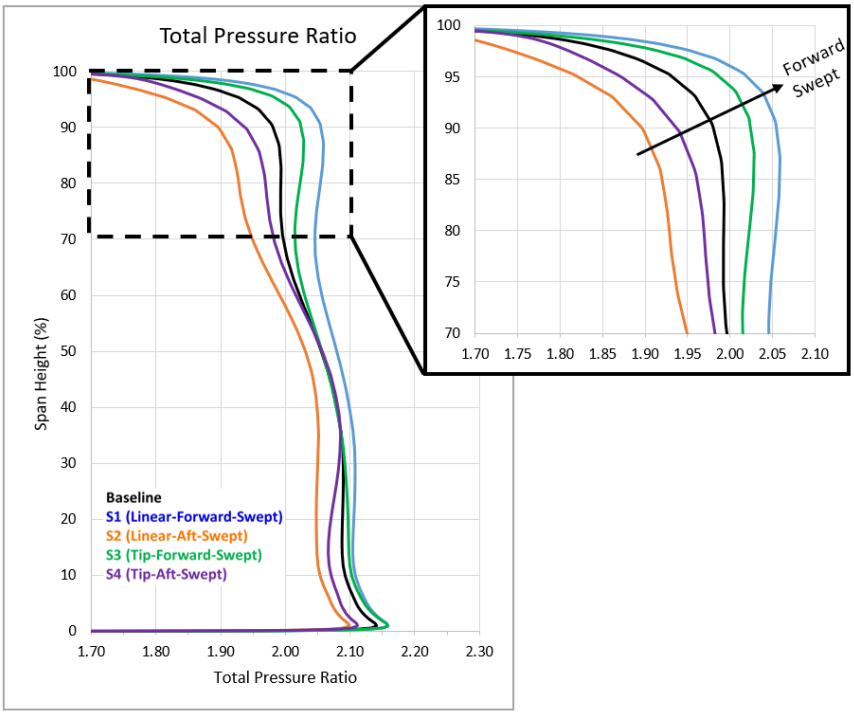

Figure 3.16 : Spanwise total pressure ratio distribution of swept geometries at design point

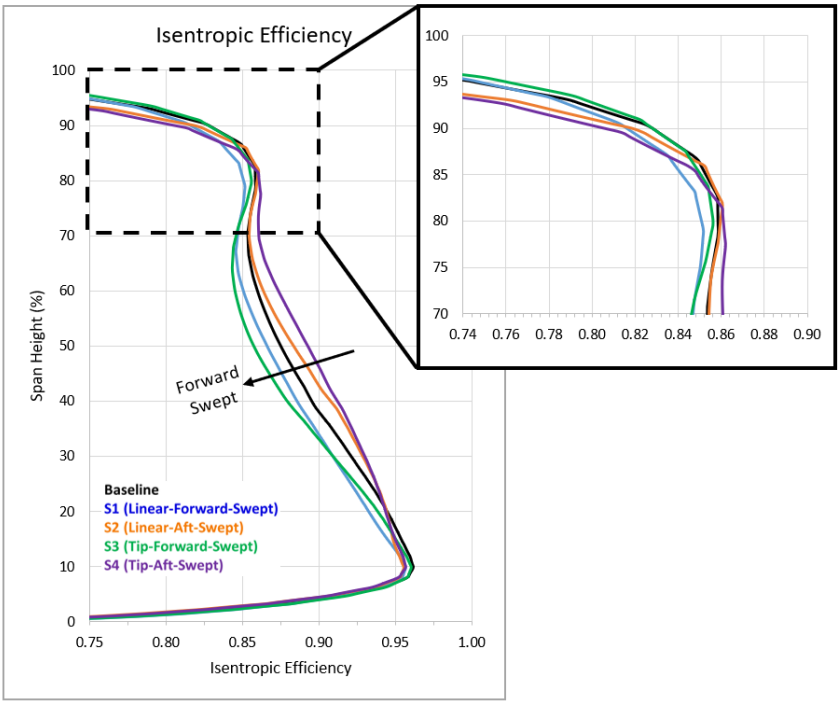

Figure 3.17 : Spanwise isentropic efficiency distribution of swept blades at design point

The understanding of the flow field at the near stall condition is important to manage the inception of the instability, namely stall. The total pressure distribution of swept geometries at near stall condition has been investigated (Figure 3.18). The forward-swept configurations (S1 and S3) have more uniform pressurization; however, that behavior is expected to be at the design point.

The aft-swept configurations (S2 and S4) have the highest loading at the tip section. The limiting section of the aft-swept geometries is seen to be the tip region, which can be associated with the tip leakage vortex. As given before (Figure 3.16), they were lightly loaded at the design point, and are highly loaded at the stall, which results in higher stall margin.

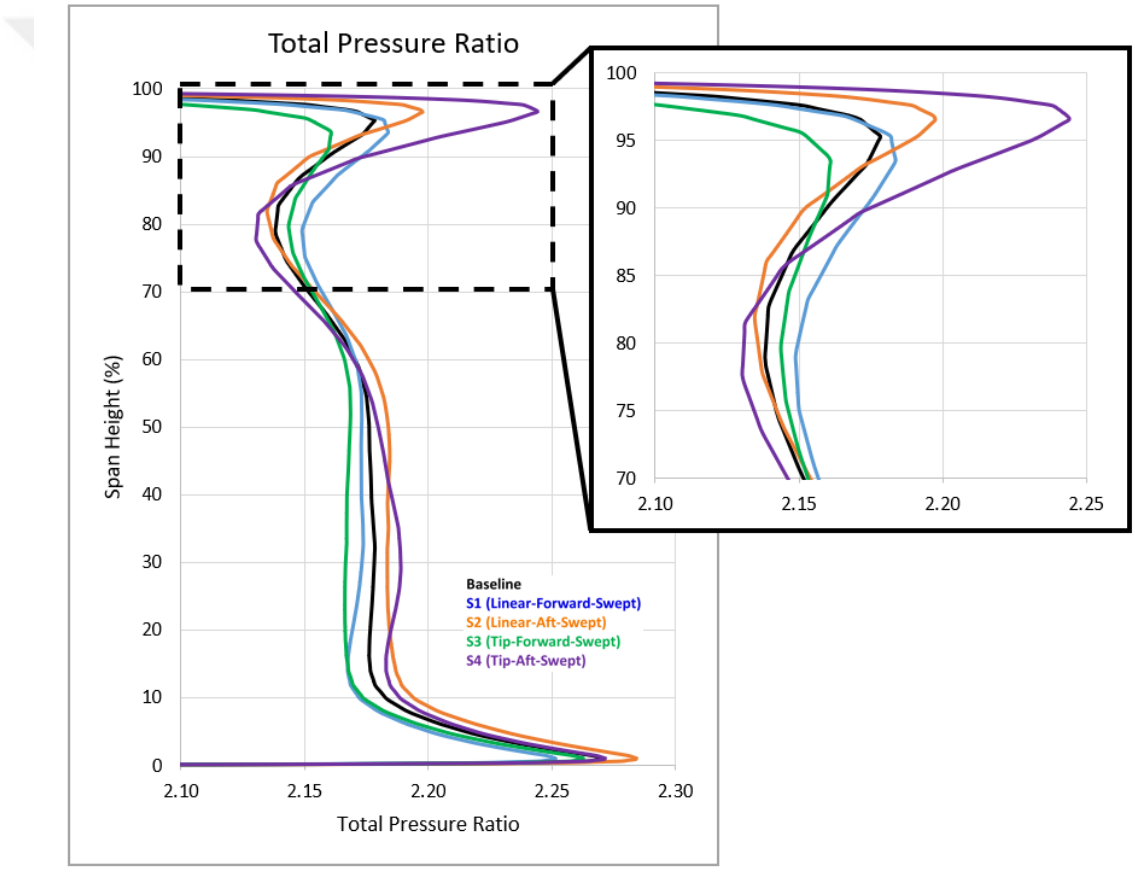

Figure 3.18 : Spanwise total pressure ratio distribution of swept blades at near stall

An effective way to capture spanwise redistribution of the stream tubes is the investigation of the normalized flux. (Figure 3.19) The forward sweep configurations (S1 and S3) create higher flux at the tip, and vice-versa at below %60 span but this change leads to a more uniform spanwise distribution compared to the baseline. The same behavior was reported by Sun et al. (2020).

The type of sweep, linear or only at the tip, does not show any difference at the tip section. The (S1 and S3) or (S2 and S4) are overlapped above the %80 span height. However, the difference at the hub region is more apparent compared to the tip region.

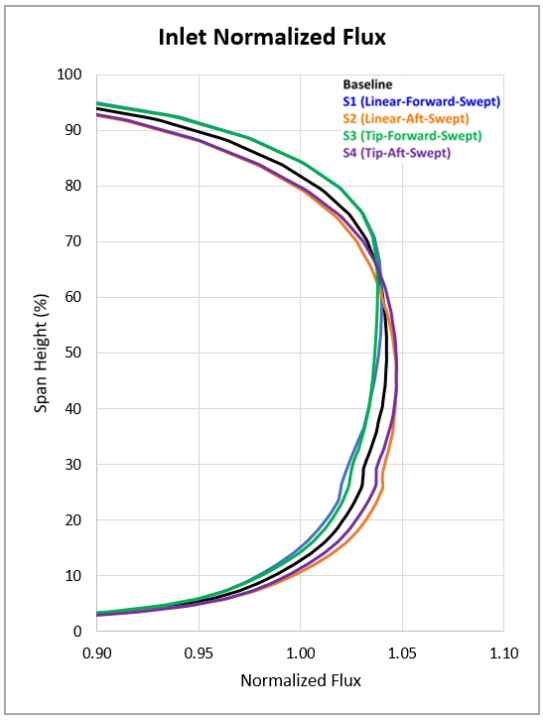

Figure 3.19 : Spanwise normalized inlet flux distribution of swept geometries at choke point

Lean

The spanwise total pressure ratio distribution of leaned blades at the design point (Figure 3.20) shows that the positive-leaned configuration (L1) has less pressurization at the tip where its lean characteristics mainly exist. The positive-bowed configuration (L3) similarly has fewer loadings at the tip; in addition, its hub region is also less loaded as a result of the bow structure. The negative-leaned configuration (L2) has less loading compared to the baseline. The Positive-Bowed configuration (L4) is very similar to the baseline in terms of loading, except mid sections. Mainly, the spanwise variation of the pressurization due to lean is quite slight. However, the isentropic efficiency has much more variation.

The spanwise isentropic efficiency distribution of leaned blades at the design point (Figure 3.21) shows that the positive-lean characteristic (L1 and L3) improves the tip efficiency while the negative-lean characteristic (L2 and L4) creates the efficiency reduction. There is no distinctive change below %60 span.

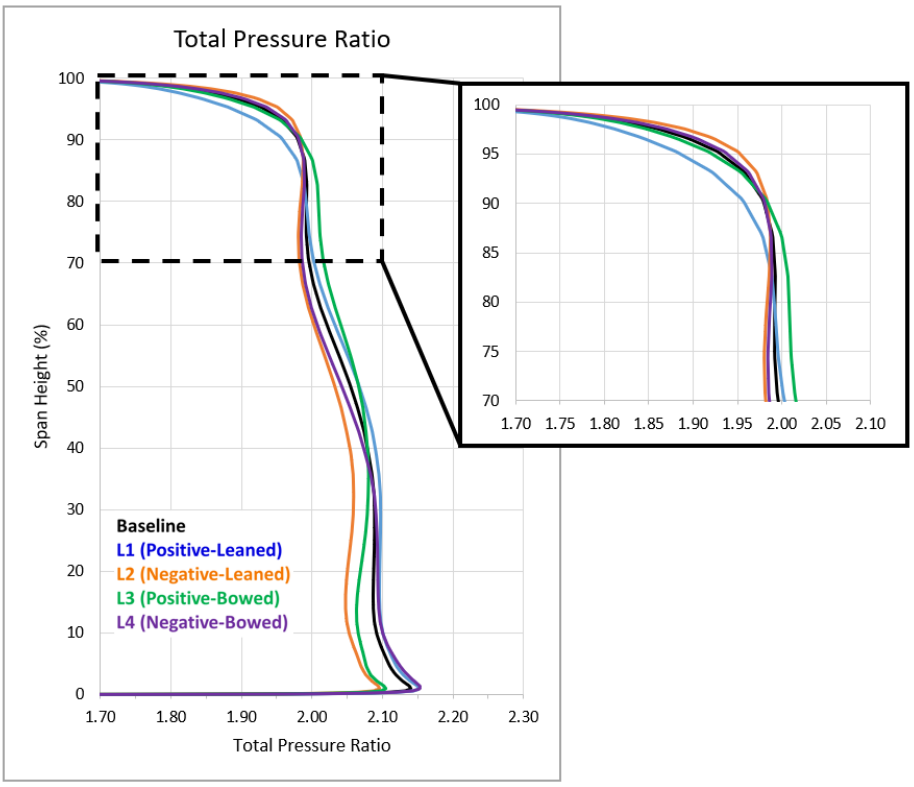

Figure 3.20 : Spanwise total pressure ratio distribution of leaned geometries at design point

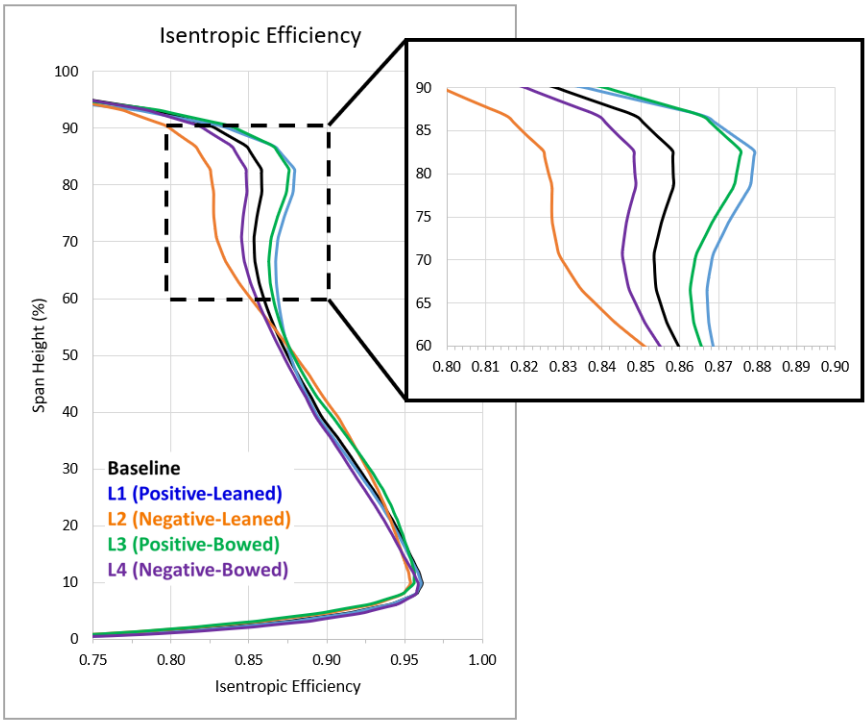

Figure 3.21 : Spanwise isentropic efficiency distribution of leaned geometries at design point

It is seen that the positive-leaned (L1) and positive-bowed (L3) configurations have more uniform loading at near-stall condition. Especially for the tip region there are no spike-type loadings. (Figure 3.22) This behavior is parallel with the operability improvement of these configurations given before. (Figure 3.14)

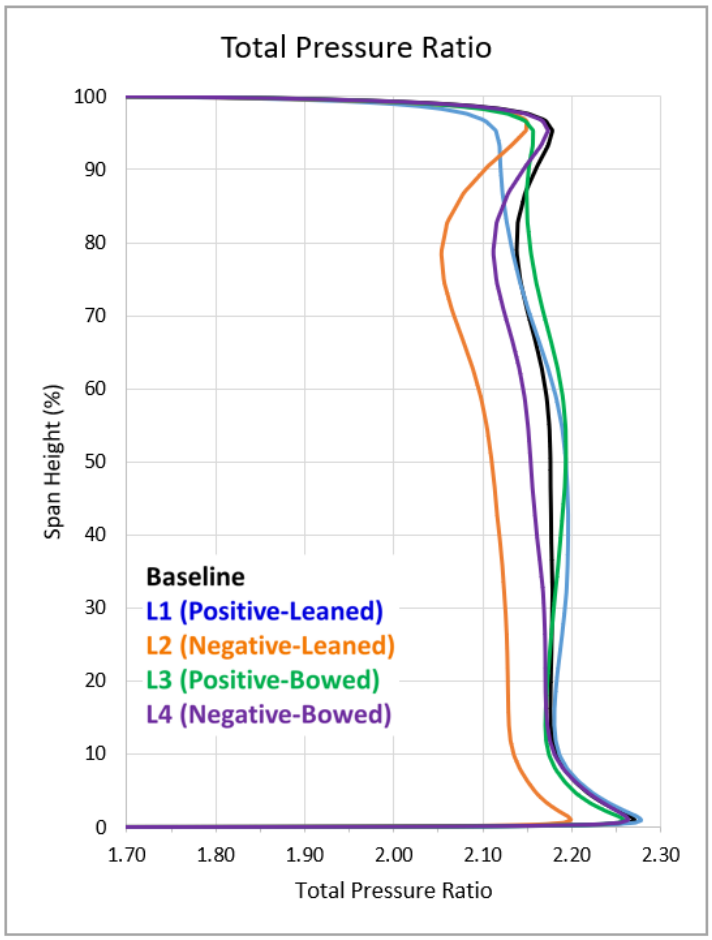

Figure 3.22 : Spanwise total pressure ratio distribution of leaned geometries at near stall

3.4 Blade-to-Blade Flow Field Results

In this section, blade-to-blade flow properties are investigated systematically. The investigations were performed on the %90 span for all cases at the design point.

Sweep

The isentropic Mach distributions of swept geometries at %90 span height and at the design point are given in Figure 3.23. It is seen that passage shock has been moved downstream and weakened with aft sweep applications while vice-versa for forward-

swept applications. Aft-swept geometries create fewer loadings in the vicinity of LE compared to forward swept ones as pointed out on the plot. The less loaded leading edge region is expected to reduce the tip leakage vortex, which will be investigated on the following sections.

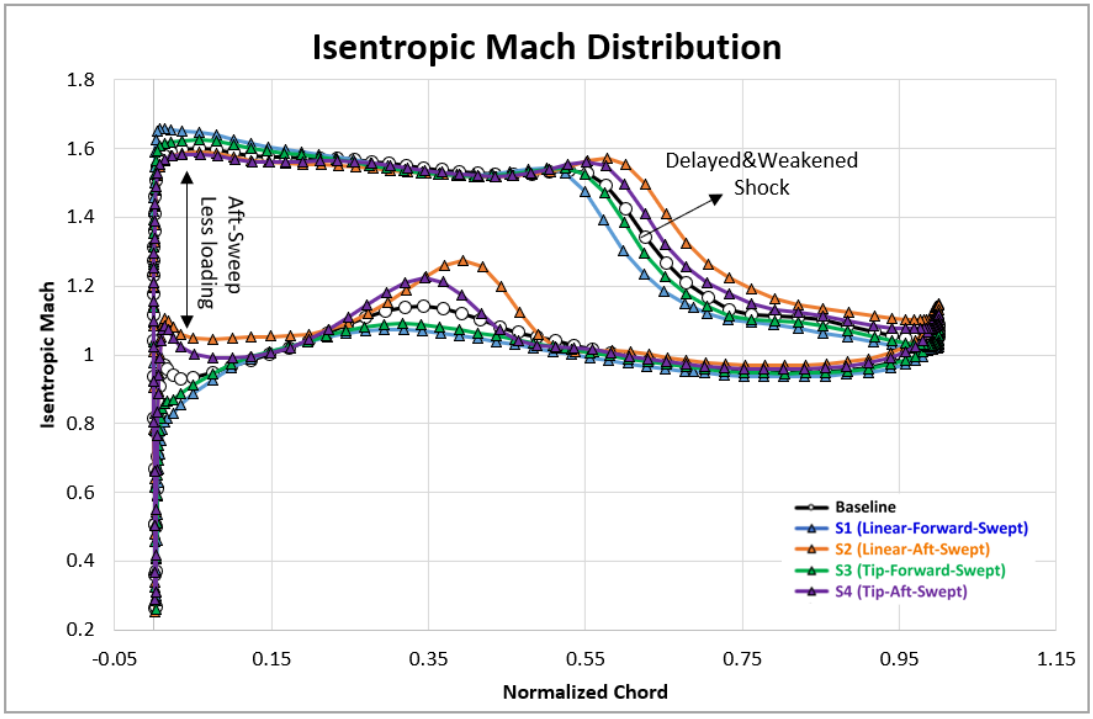

Figure 3.23 : Isentropic mach distributions of swept geometries at %90 span height and design point

The relative Mach field comparison of S1 with baseline at %90 span and the design point is given in Figure 3.24. The wake region is seen to be slightly better at the S1 configuration. Increased shock strength results as forming of expelled shock and movement of the passage shock is seen. Also, the pressure side spike is reduced with the S1 configuration.

The relative mach field comparison of S2 with baseline at %90 span and design point is given in Figure 3.25. The wake region is seen to be slightly enlarged at the S2 configuration. Decreased shock strength results in swallowed shock. Also, the pressure side spike grows up forming secondary acceleration region.

The blade-to-blade flow characteristics of the S3 and S4 configurations (Figure 3.26 and Figure 3.27) are quite similar to S1 and S2 configurations, respectively.

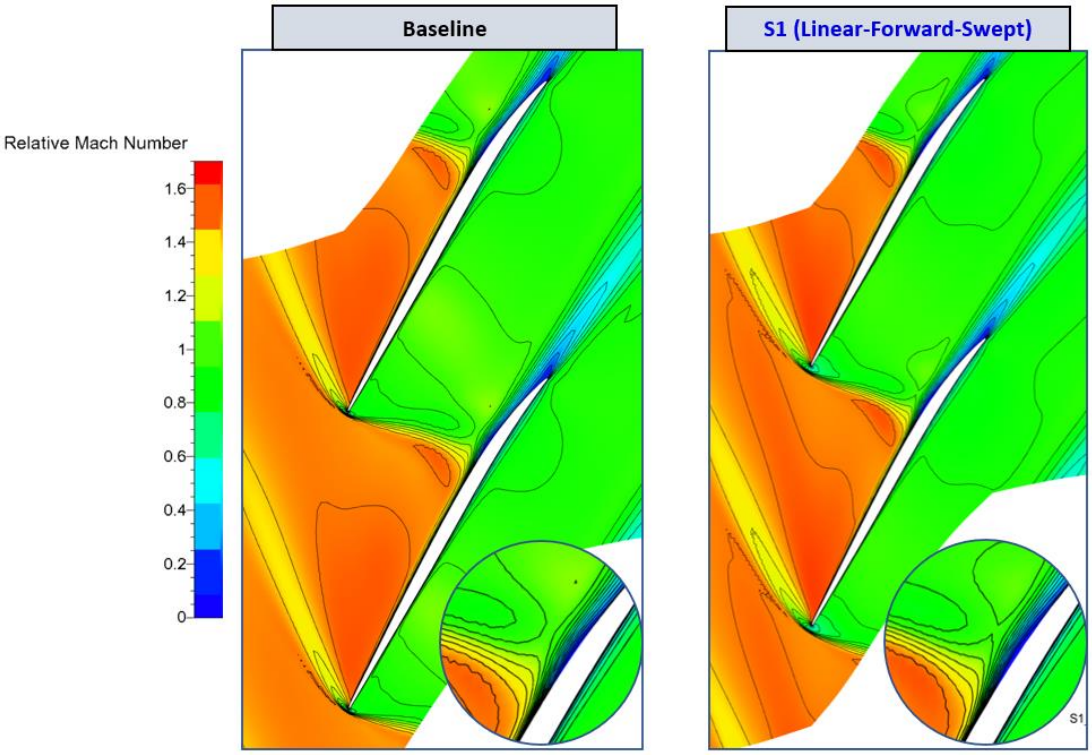

Figure 3.24 : Relative mach field comparison of S1 at %90 span and design point

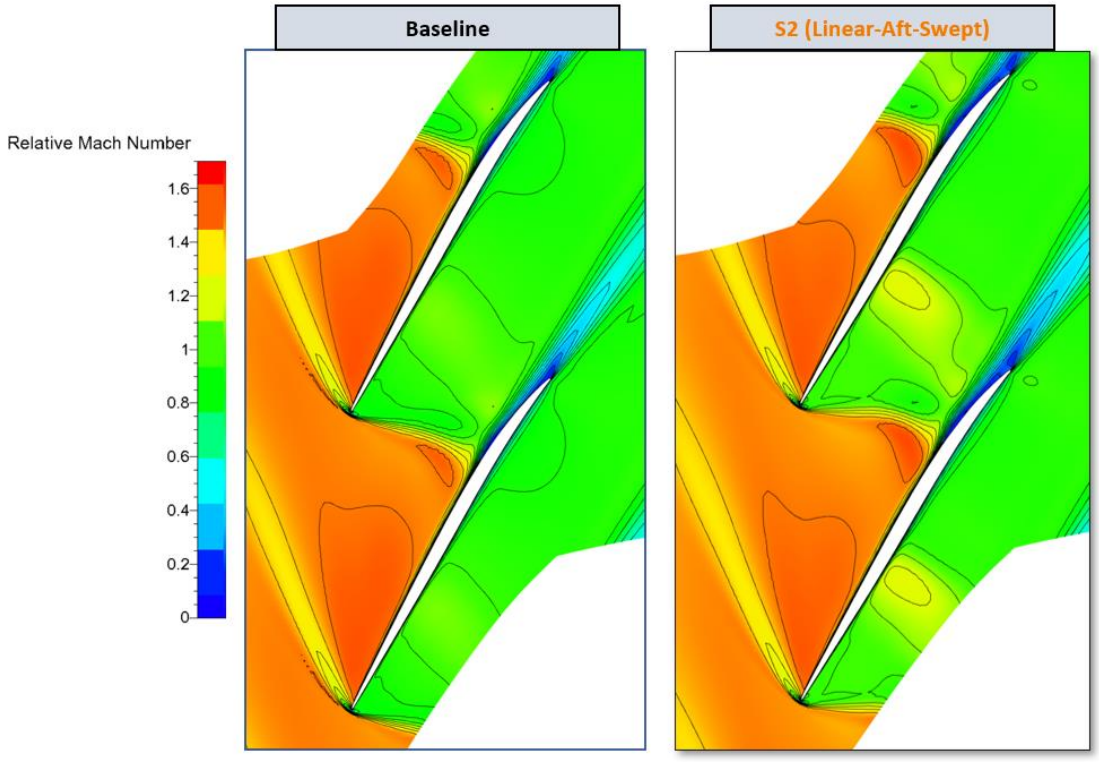

Figure 3.25 : Relative mach field comparison of S2 at %90 span and design point

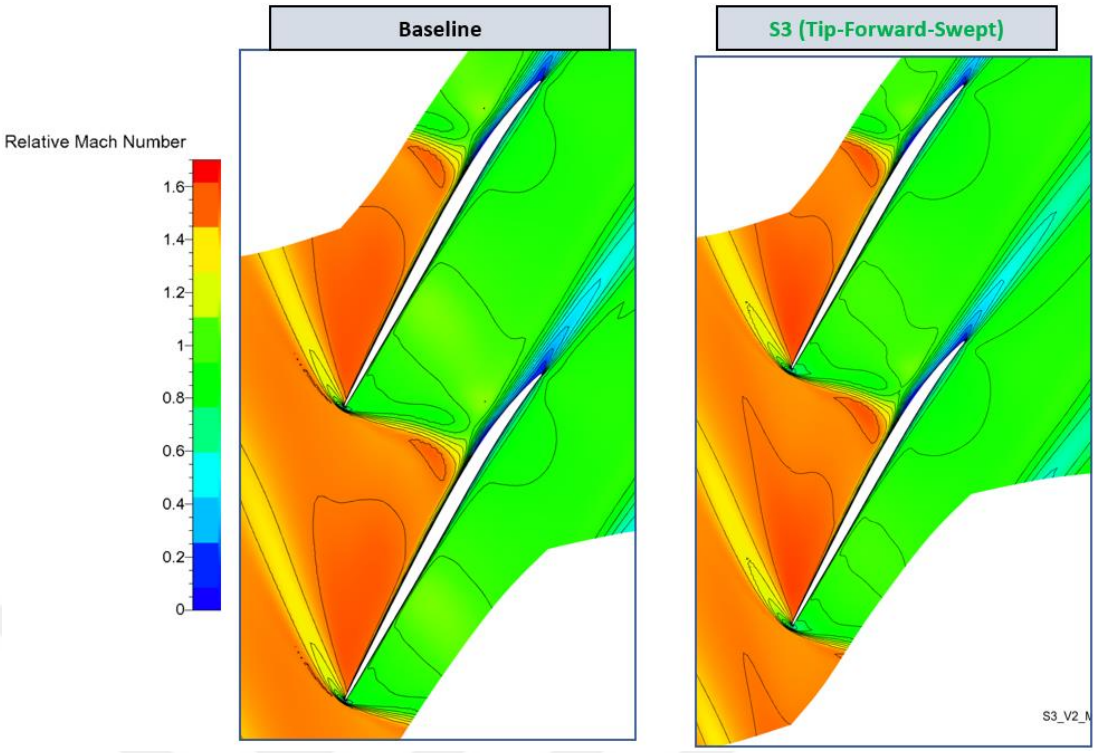

Figure 3.26 : Relative mach field comparison of S3 at %90 span and design point

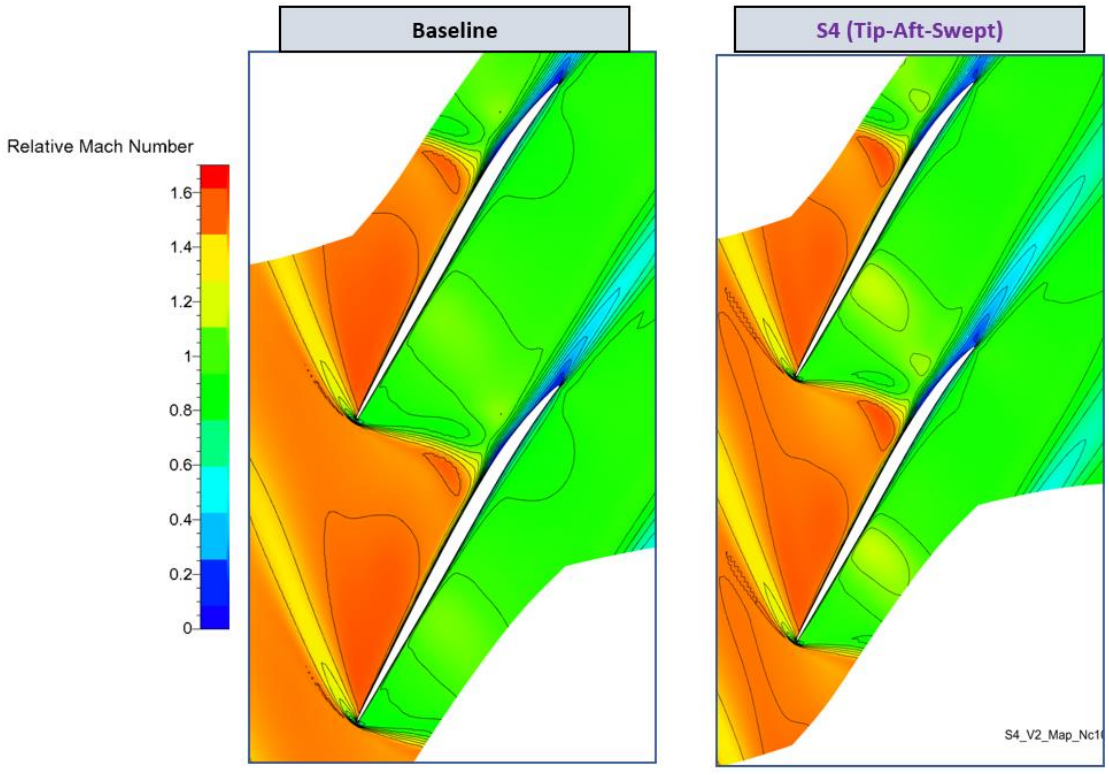

Figure 3.27 : Relative mach field comparison of S4 at %90 span and design point

Lean

The isentropic mach distributions of leaned geometries at %90 span height and at the design point are given with Figure 3.28. It is seen that passage shock has been moved downstream and weakened with positive lean applications. Positive-leaned geometries create fewer loadings in the vicinity of the leading edge compared to negative-leaned ones. The acceleration at the pressure side is slightly affected by lean.

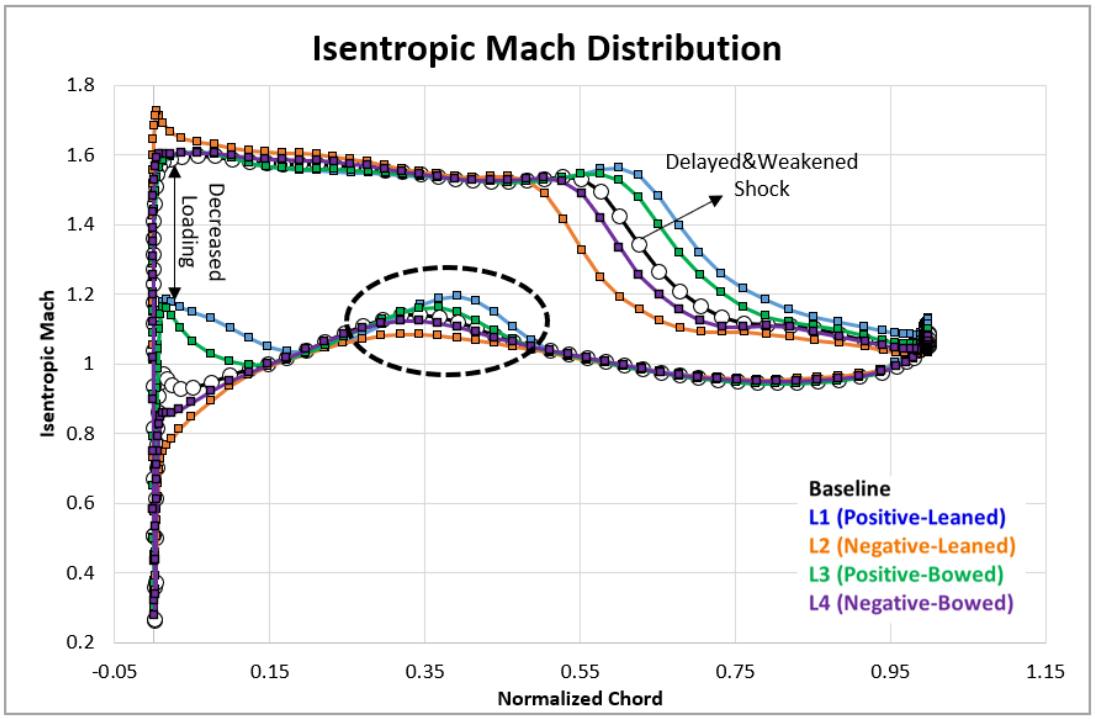

Figure 3.28 : Isentropic Mach distributions of leaned geometries at %90 span height and at the design point

The relative mach field comparison of L1 with baseline at %90 span and design point is given with Figure 3.29. The wake region is seen to be slightly enlarged at the L1 configuration. Decreased shock strength results in swallowed shock. Also, the pressure side spike is increased slightly with forming secondary passage acceleration.

The relative mach field comparison of L2 with baseline at %90 span and design point is given in Figure 3.30. Shock is being expelled and formed to be detached, which is close to stalling condition.

The blade-to-blade flow characteristics of the L3 and L4 configurations (Figure 3.31 and Figure 3.32) are quite similar to L1 and L2 configurations, respectively.

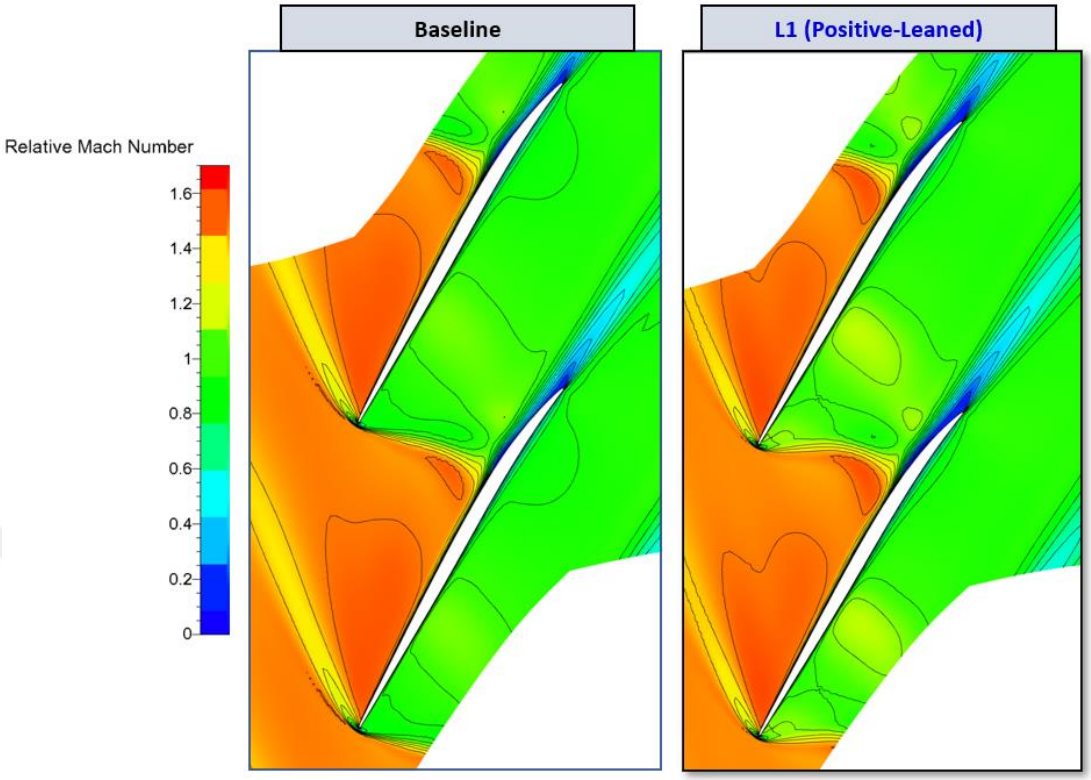

Figure 3.29 : Relative Mach field comparison of L1 at %90 span and design point

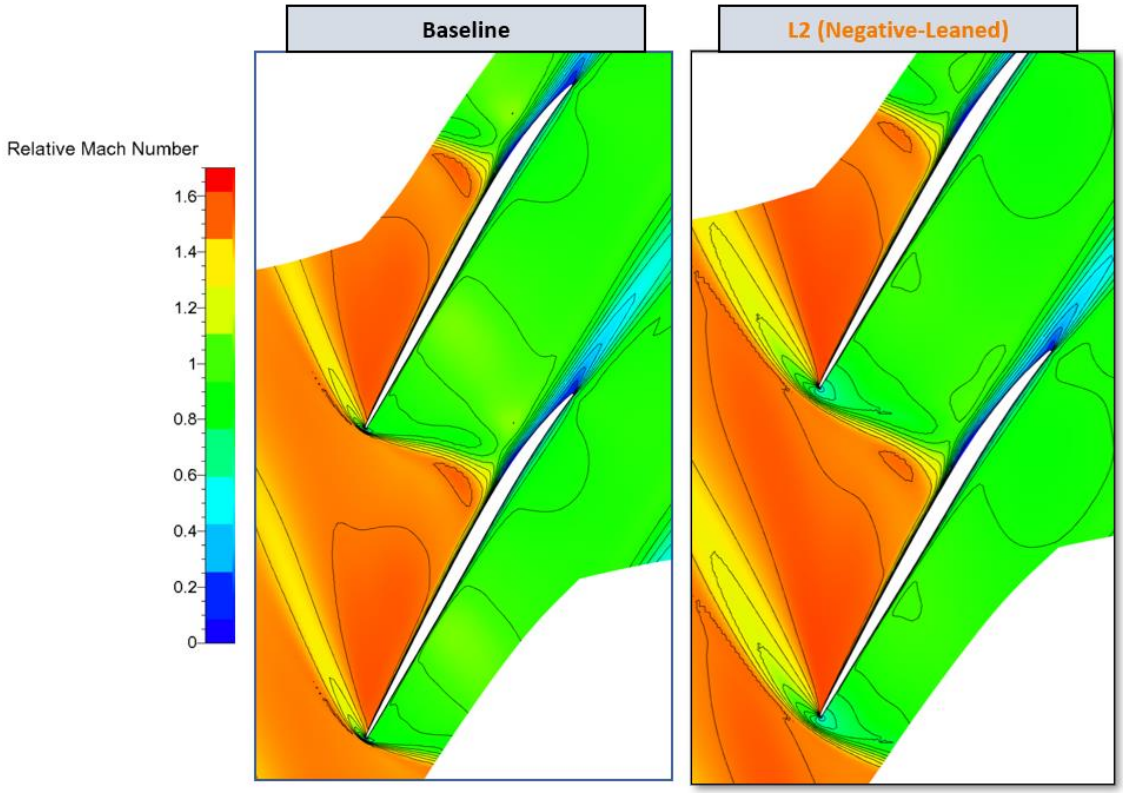

Figure 3.30 : Relative Mach field comparison of L2 at %90 span and design point

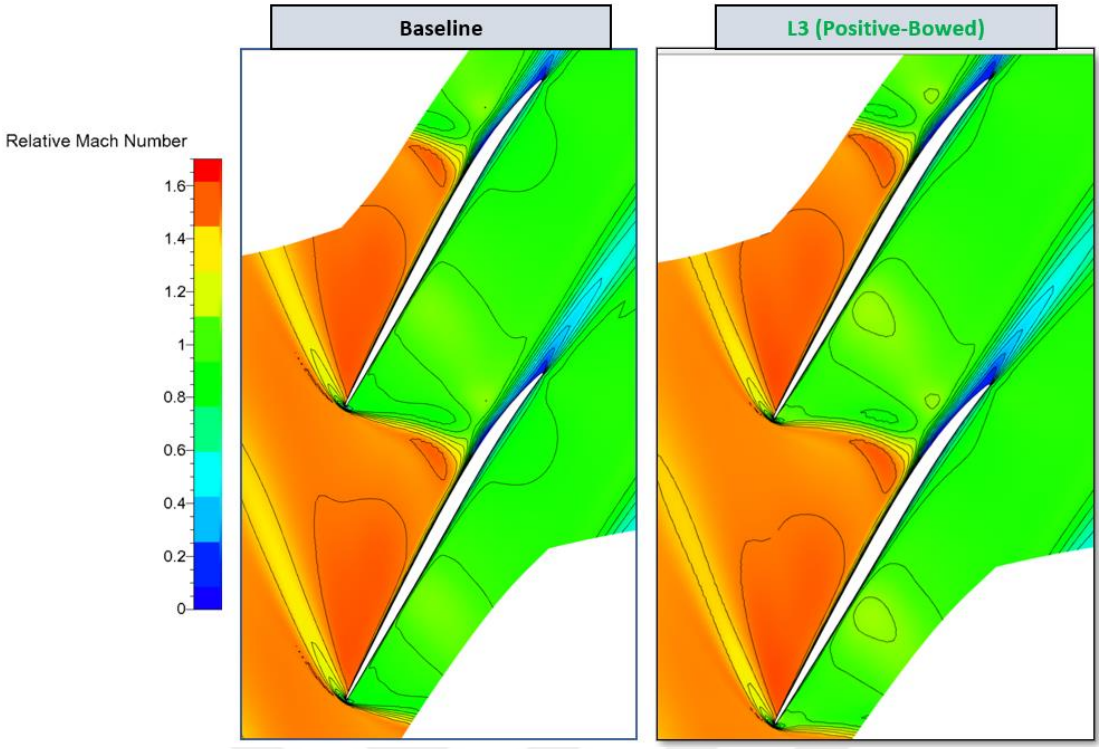

Figure 3.31 : Relative Mach field comparison of L3 at %90 span and design point

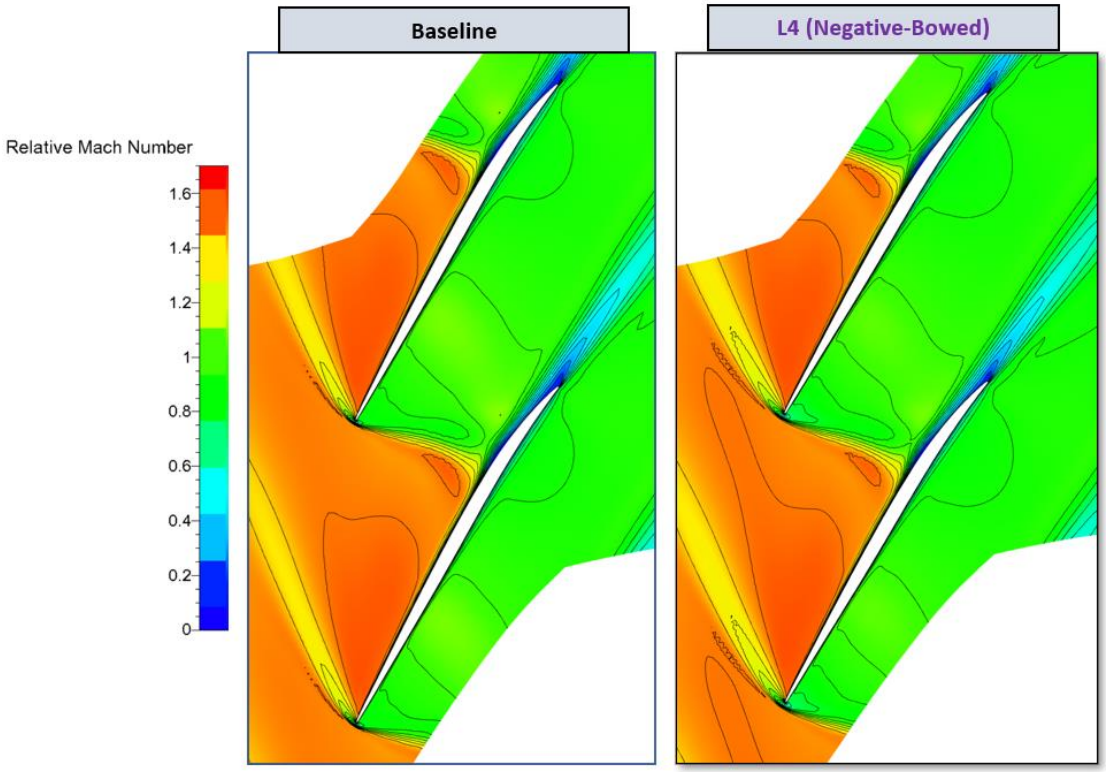

Figure 3.32 : Relative Mach field comparison of L4 at %90 span and design point

3.5 Surface Streamline Results

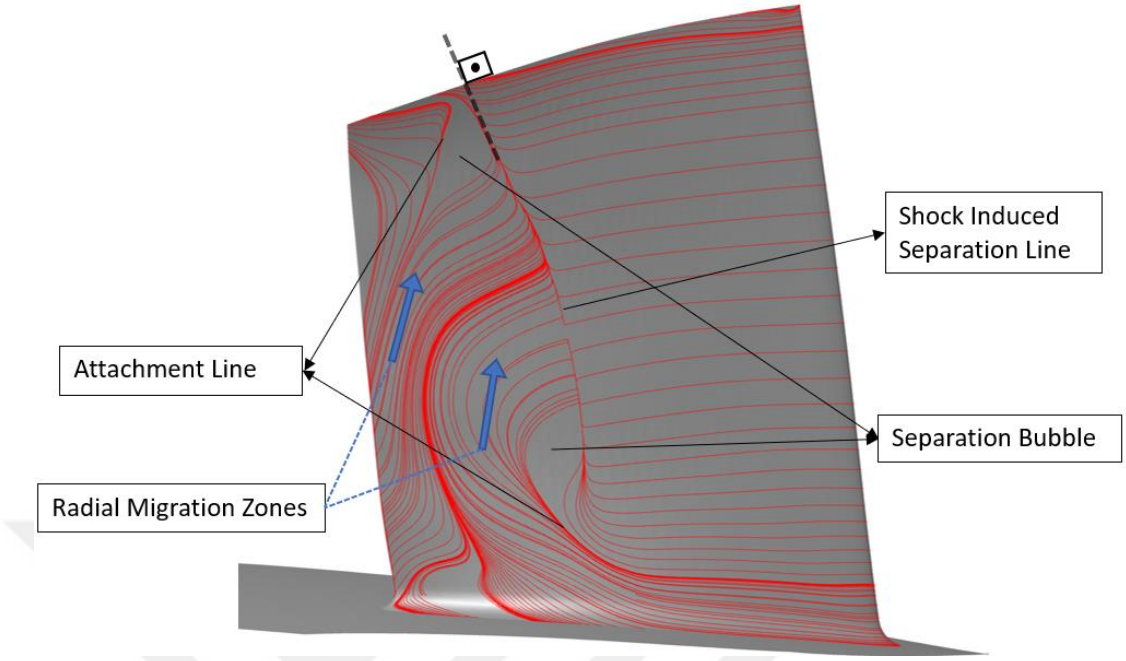

Figure 3.33 : Surface limiting streamlines of baseline solution at design point

The surface limiting streamlines on the suction side of the baseline solution at the design point is given in Figure 3.33. The shock induced-separation region exists widely in the spanwise direction. The separation bubbles that are formed between the separation and re-attachment lines are seen in the specific regions. The radial migration flow pattern is seen below the separation lines. The shock is seen to be perpendicular to the endwall at the tip, which was also given by Domercq (2012).

Sweep

The comparison of the surface limiting streamlines of the S1 swept geometry and baseline is given in Figure 3.34. The passage shock at the tip section is seen to be shifted to the leading edge, which was seen on blade loadings. The separation bubble is enlarged, which is the reason behind the efficiency deficit seen in the 1D results (Figure 3.17). It is seen that the perpendicularity of shock at the tip is conserved.

The comparison of the surface limiting streamlines of the S2 swept geometry and baseline is given with Figure 3.35. The passage shock at the tip section is seen to be shifted to the trailing edge, which was seen on blade loadings. The separation bubble is just about to be eliminated. The efficiency improvement seen in the 1D results is

compatible with the separation bubble behavior. The perpendicularity of shock at the tip is conserved.

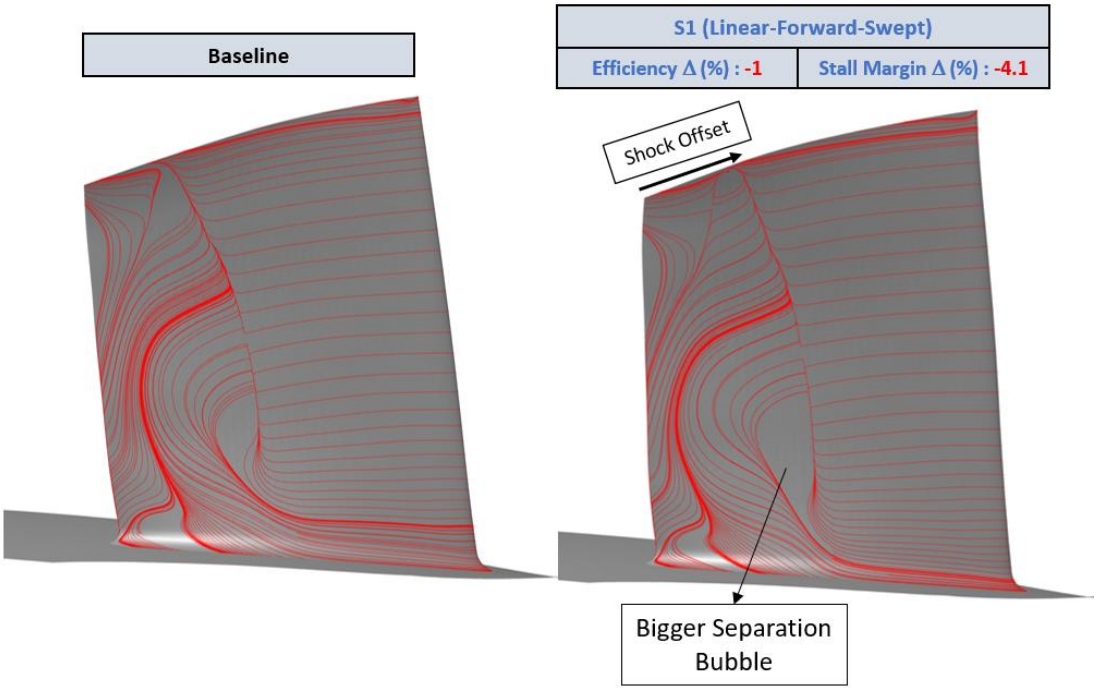

Figure 3.34 : Surface limiting streamlines of the S1 and baseline at design point

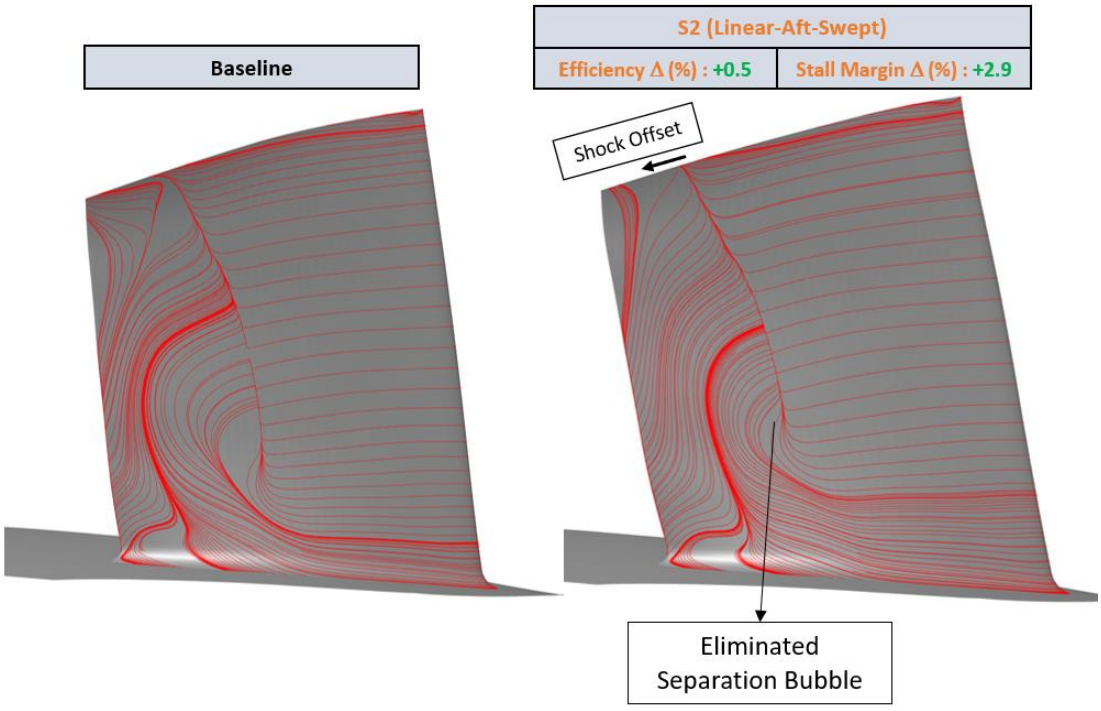

Figure 3.35 : Surface limiting streamlines of the S2 and baseline at design point

The surface limiting streamline characteristics of the S3 and S4 configurations (Figure 3.36 and Figure 3.37) are quite similar to S1 and S2 configurations, respectively.

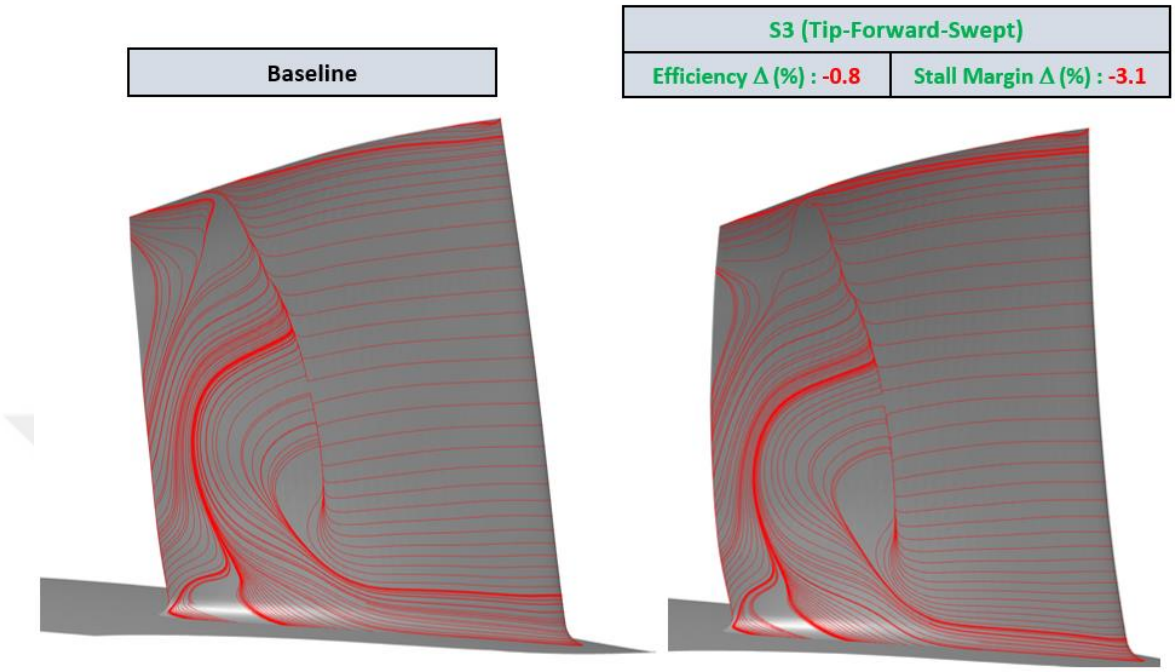

Figure 3.36 : Surface limiting streamlines of the S3 and baseline at design point

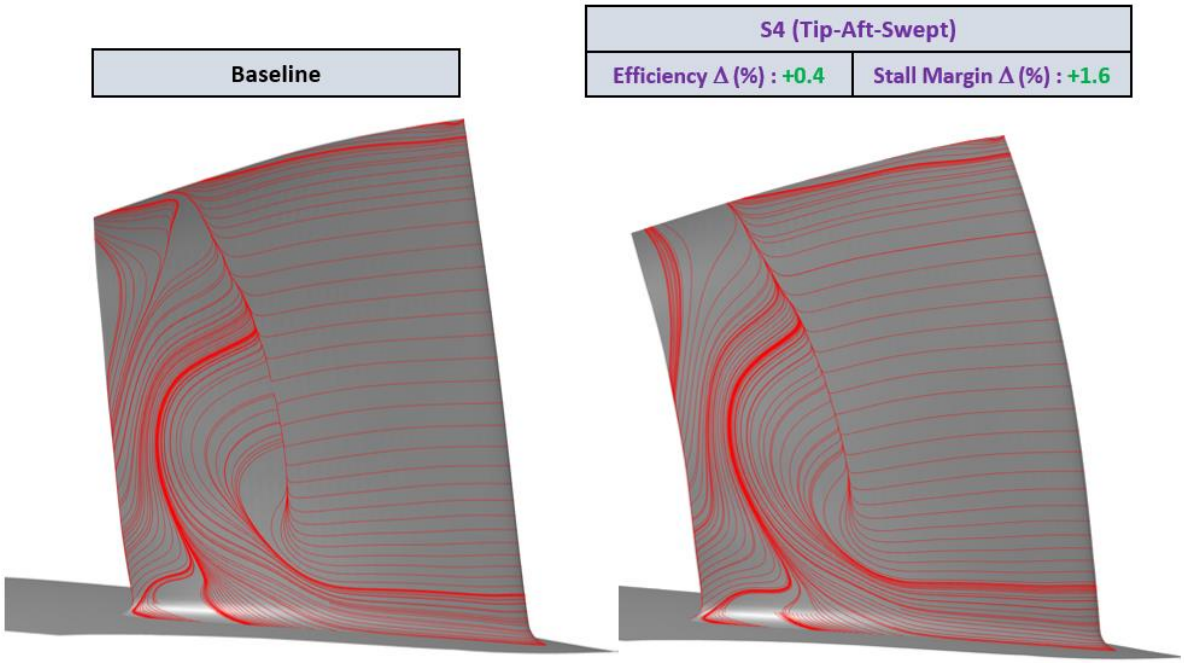

Figure 3.37 : Surface limiting streamlines of the S4 and baseline at design point

Lean

The comparison of the surface limiting streamlines of the L1 leaned geometry and baseline is given in Figure 3.38. The passage shock at the tip section shifted to the trailing edge, which was seen on blade loadings. The separation bubble at the tip section is just about to be eliminated. The efficiency improvement was seen in the spanwise results at the tip section. The separation bubble at mid span is conserved. It is seen that the perpendicularity of shock at the tip is conserved.

The comparison of the surface limiting streamlines of the L2 leaned geometry and baseline is given in Figure 3.39. The passage shock at the tip section shifted to the leading edge, which was seen on blade loadings. The separation bubble at mid span is smaller compared to the baseline. It is seen that the perpendicularity of shock at the tip is conserved here, too.

The surface limiting streamline characteristics of the L3 and L4 configurations (Figure 3.40 and Figure 3.41) are quite similar to L1 and L2 configurations, respectively.

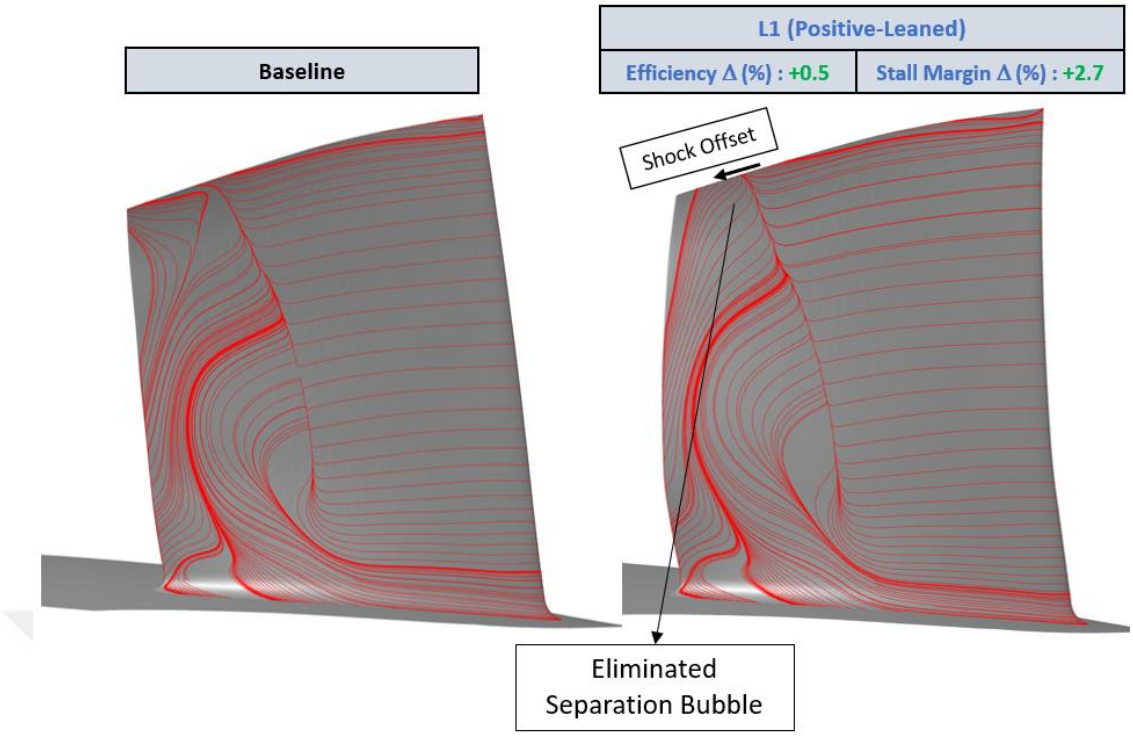

Figure 3.38 : Surface limiting streamlines of the L1 and baseline at design point

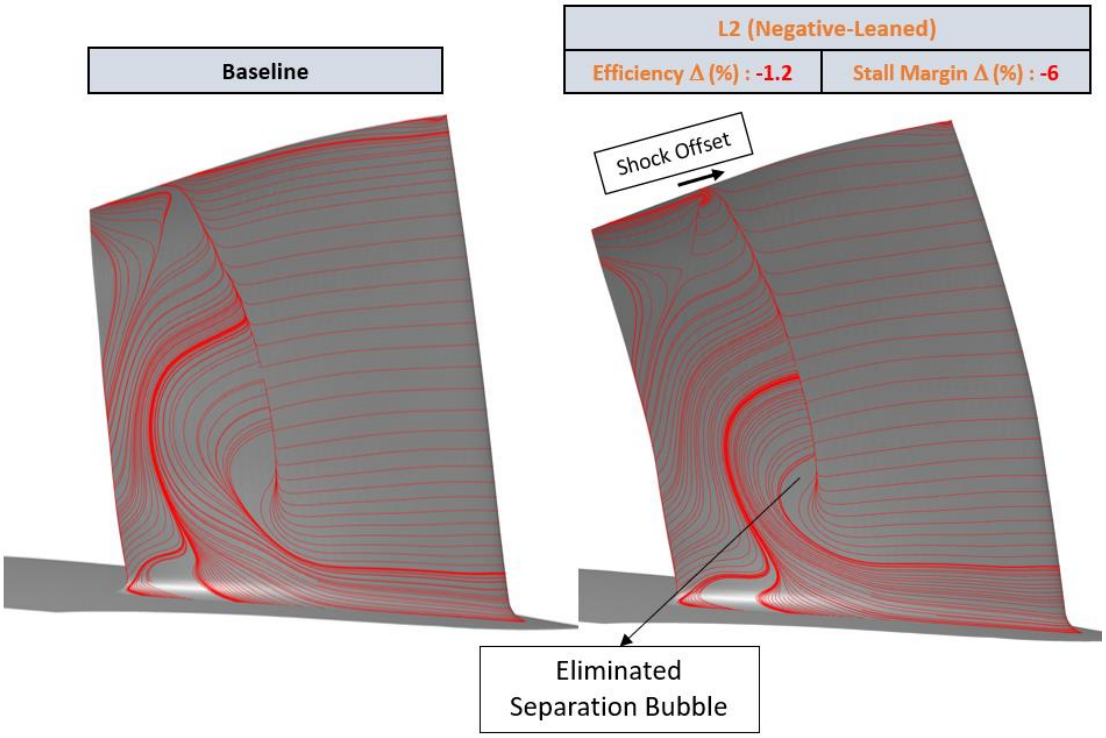

Figure 3.39 : Surface limiting streamlines of the L2 and baseline at design point

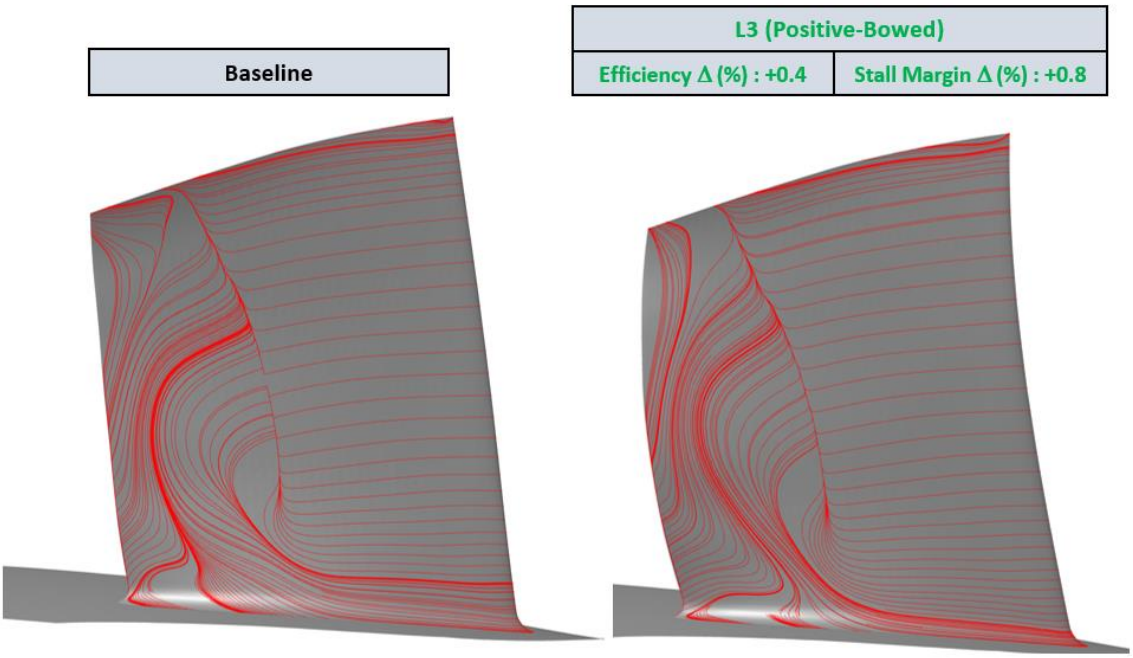

Figure 3.40 : Surface limiting streamlines of the L3 and baseline at design point

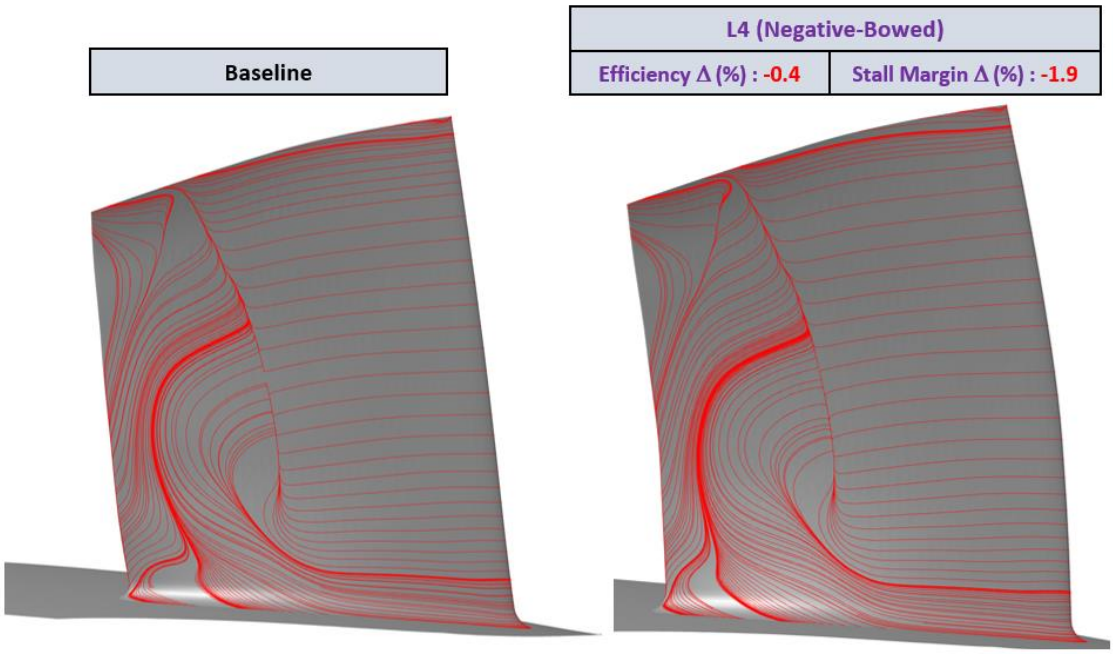

Figure 3.41 : Surface limiting streamlines of the L4 and baseline at design point

3.6 Tip Leakage Flow

The tip leakage loss is one of the major loss sources in the turbomachinery design, which is approximately accounting for up to 1/3 of the total loss. (Denton, 1993) Tip leakage forms a vortex structure, sometimes a second structure also exists. The entropy generation due to tip leakage vortex majorly affects the blade performance and flow field.

In this section, the tip leakage vortex and entropy generation through passage have been investigated.

Sweep

The tip leakage vortex and entropy generation of S1 at the design point are given in Figure 3.42. The tip leakage vortex of the S1 configuration has a wider radius which reflects the stronger vortex. High entropy generation areas are also seen starting from near the upstream planes. Also, the number of streamlines that feed the secondary vortex is less compared to the baseline.

The tip leakage vortex and entropy generation of S2 at the design point are given in Figure 3.43. The tip leakage vortex of the S2 configuration is weaker. Entropy generation is seen to be improved. The high entropy generation areas shifted to the passage exit All the streamlines of TLV mix with mainstream without feeding the secondary vortex of the adjacent blade around the trailing edge.

The tip leakage vortex and entropy generation characteristics of the S3 and S4 configurations (Figure 3.44 and Figure 3.45) are quite similar to S1 and S2 configurations, respectively.

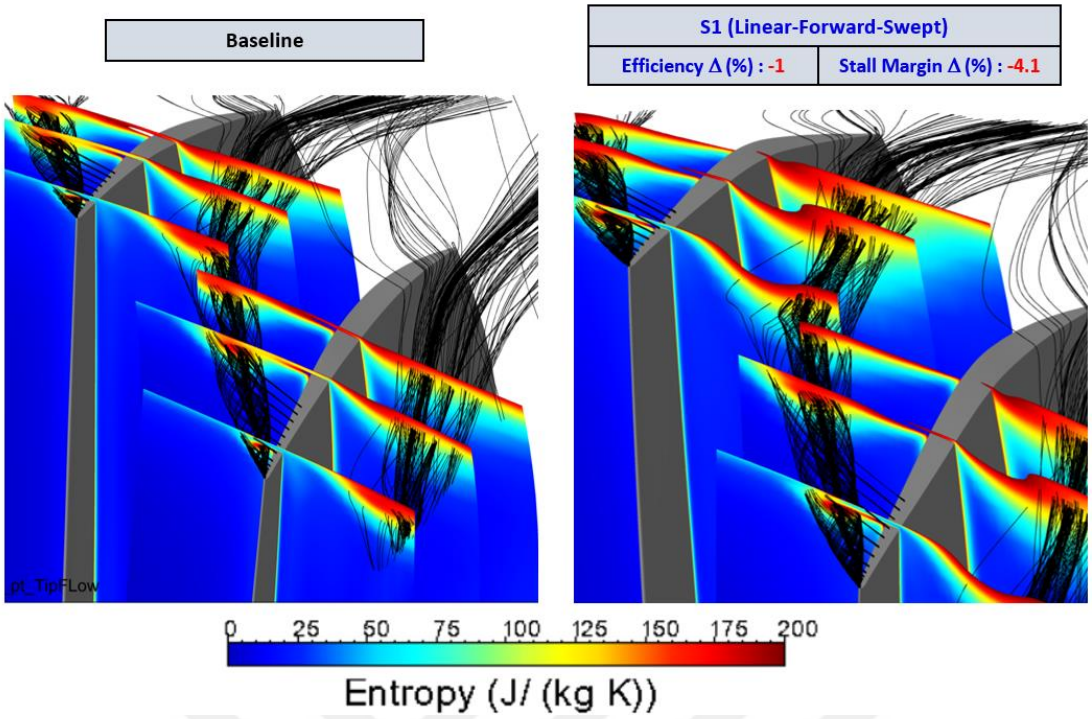

Figure 3.42 : Tip leakage vortex and entropy generation of S1 at design point

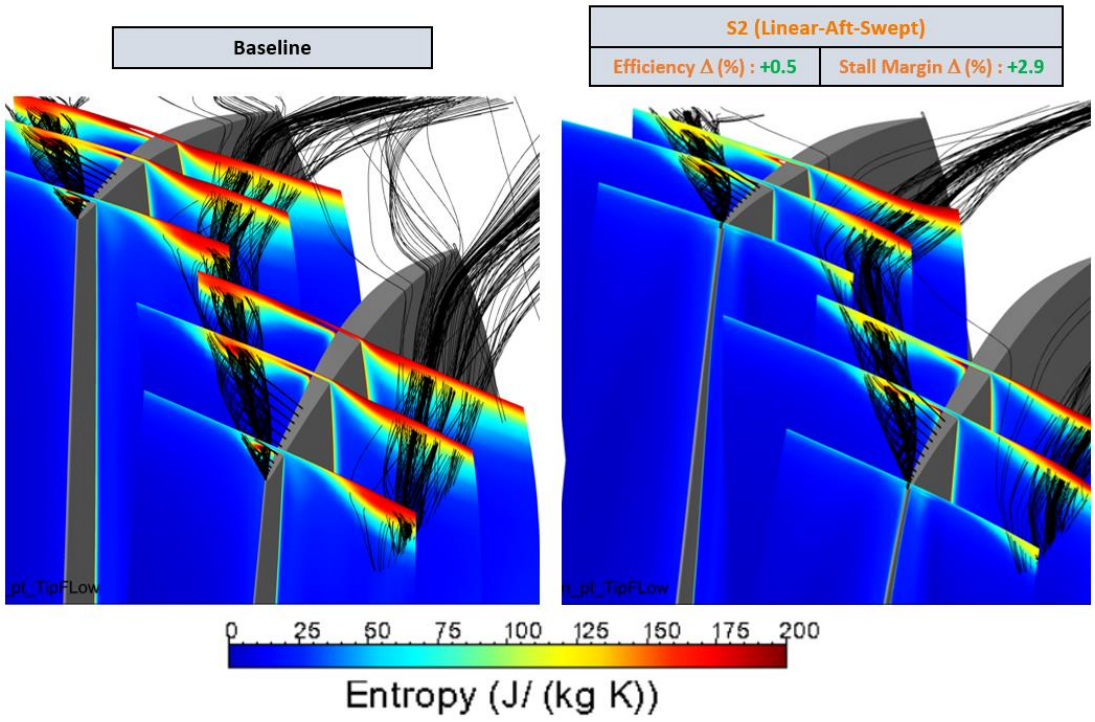

Figure 3.43 : Tip leakage vortex and entropy generation of S2 at design point

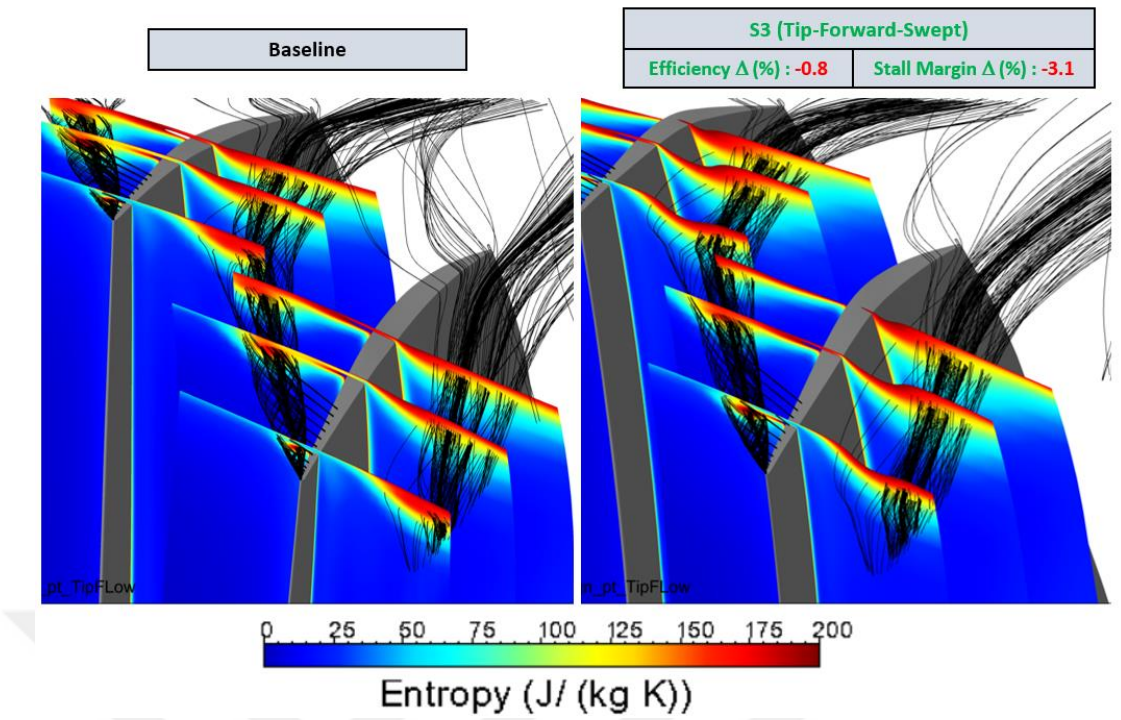

Figure 3.44 : Tip leakage vortex and entropy generation of S3 at design point

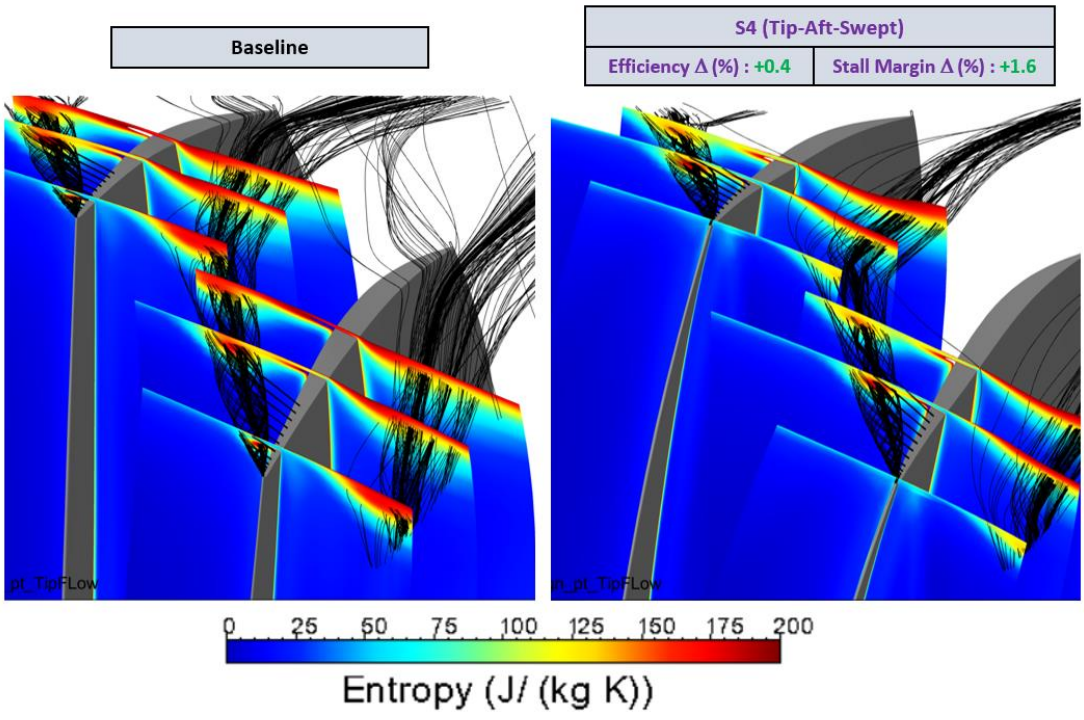

Figure 3.45 : Tip leakage vortex and entropy generation of S4 at design point

Lean

The tip leakage vortex and entropy generation of L1 at the design point are given in Figure 3.46. The tip leakage vortex of the L1 configuration is weaker. Entropy generation is seen to be improved. The high entropy generation areas shifted to the passage exit and smoothed in the azimuthal direction. All the streamlines of TLV mix with mainstream without feeding the secondary vortex of the adjacent blade around the trailing edge.

The tip leakage vortex and entropy generation of L2 at the design point is given in Figure 3.47. The tip leakage vortex of the L2 configuration has a wider radius which reflects the stronger vortex. High entropy generation areas are also seen starting from near the upstream planes. The leakage flow that feeds the secondary vortex is much more stronger as marked in the figure.

The tip leakage vortex and entropy generation characteristics of the L3 and L4 configurations (Figure 3.48 and Figure 3.49) are quite similar to L1 and L2 configurations, respectively.

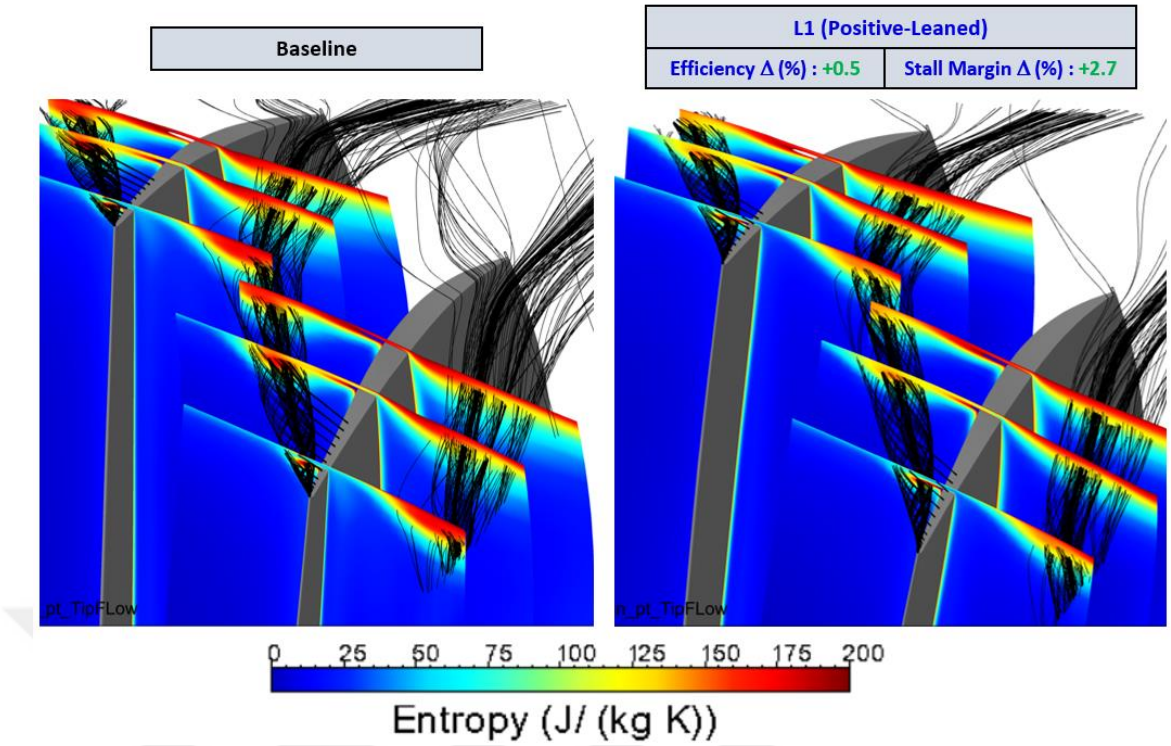

Figure 3.46 : Tip leakage vortex and entropy generation of L1 at design point

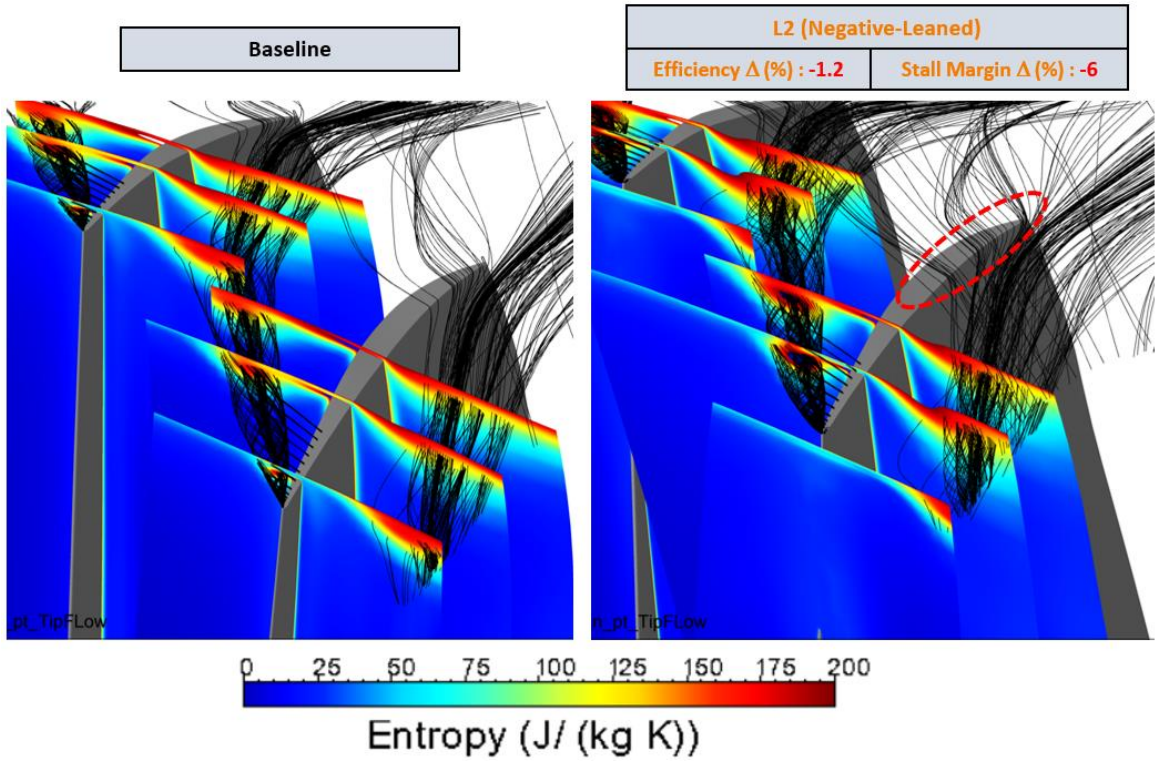

Figure 3.47 : Tip leakage vortex and entropy generation of L2 at design point

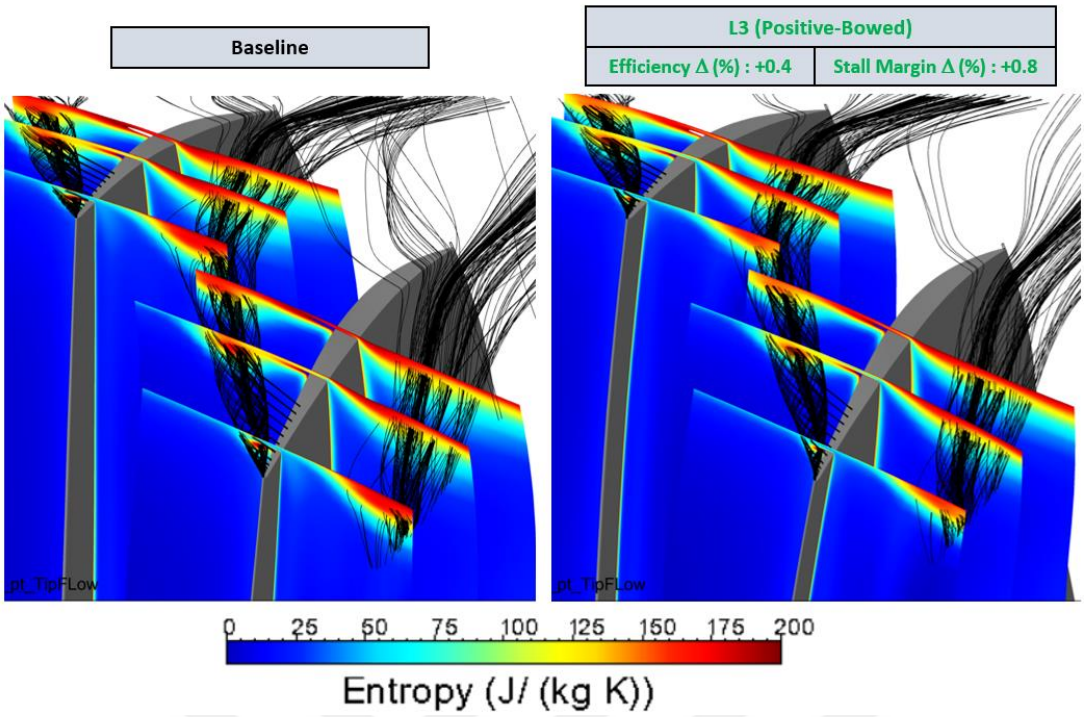

Figure 3.48 : Tip leakage vortex and entropy generation of L3 at design point

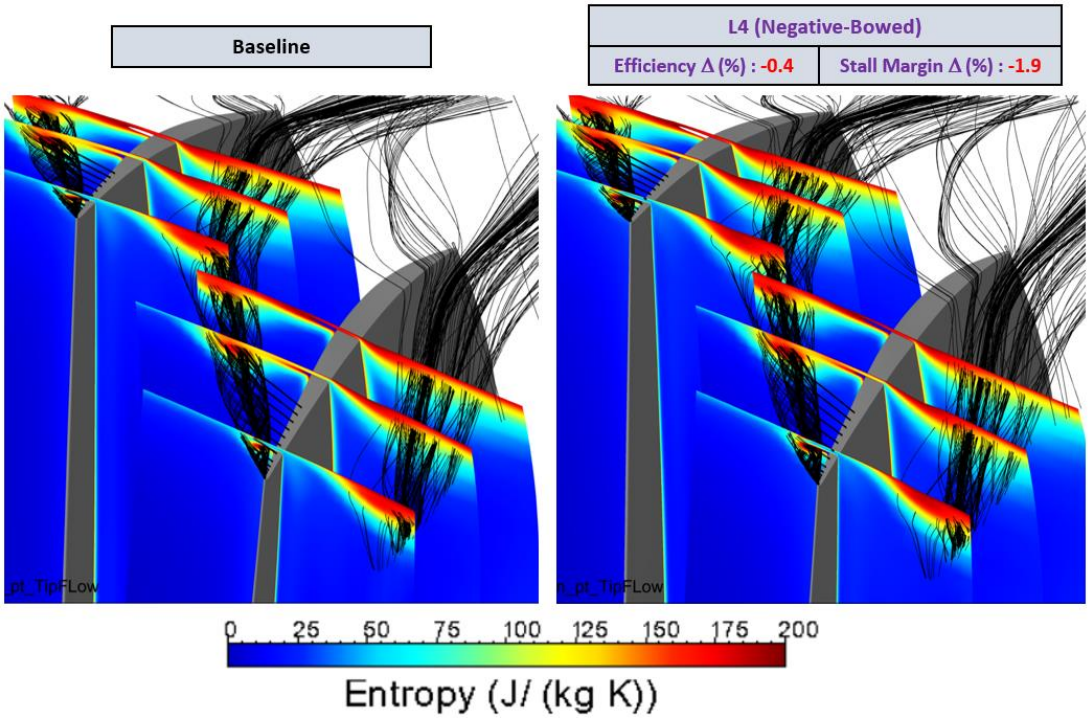

Figure 3.49 : Tip leakage vortex and entropy generation of L4 at design point

4. COMBINED DESIGN

4.1 Combined Geometry

As a final investigation step, the most promising sweep and lean configurations, S2 (Linear-Aft-Swept) and L1 (Positive-Leaned), are combined to further investigate under the assumption of linear superpositioning. (Figure 4.1) The aerodynamic performance of the combined configuration has been investigated with exact similar approaches.

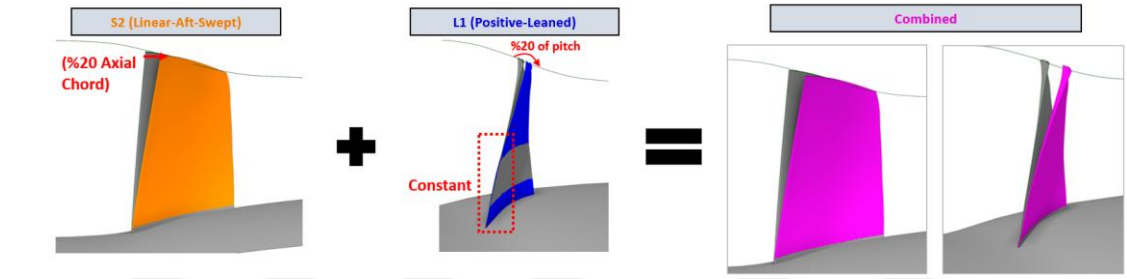

Figure 4.1 : Schematic of combined geometry

4.2 Global Performance

The pressure and efficiency maps of the most promising sweep and lean configurations, S2 (Linear-Aft-Swept) and L1 (Positive-Leaned), and combined geometry are given in Figure 4.2 and Figure 4.3. The combined geometry has the performance characteristic of the superposition of the single cases. The throat capacity is seen to be driven by sweep characteristics. The isentropic efficiency of the combined case is higher than in both cases. Also, the peak total pressure ratio is higher compared to the single cases, S2 and L1.

The comparison of the design point efficiency and stall margin of the combined geometry with baseline and the most promising sweep and lean configurations have been given in Figure 4.4 and Figure 4.5. The combined case reflects a better performance in terms of operability and efficiency. It has a 4.67% stall margin and 0.83% isentropic efficiency improvement.

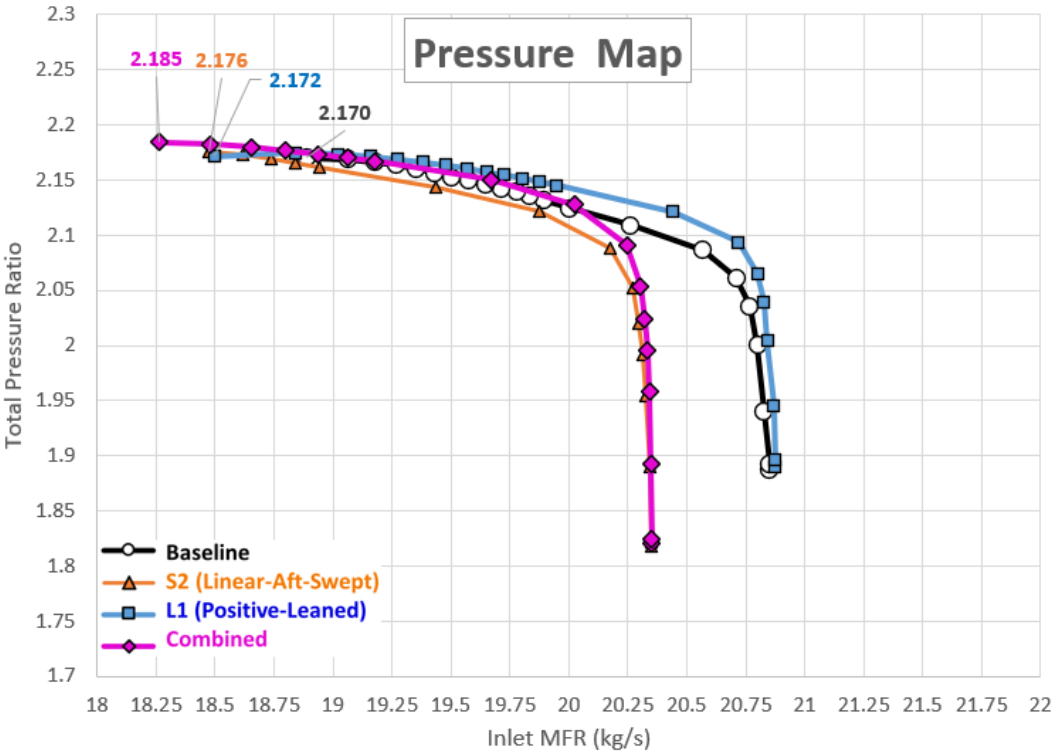

Figure 4.2 : Pressure map of the combined geometry

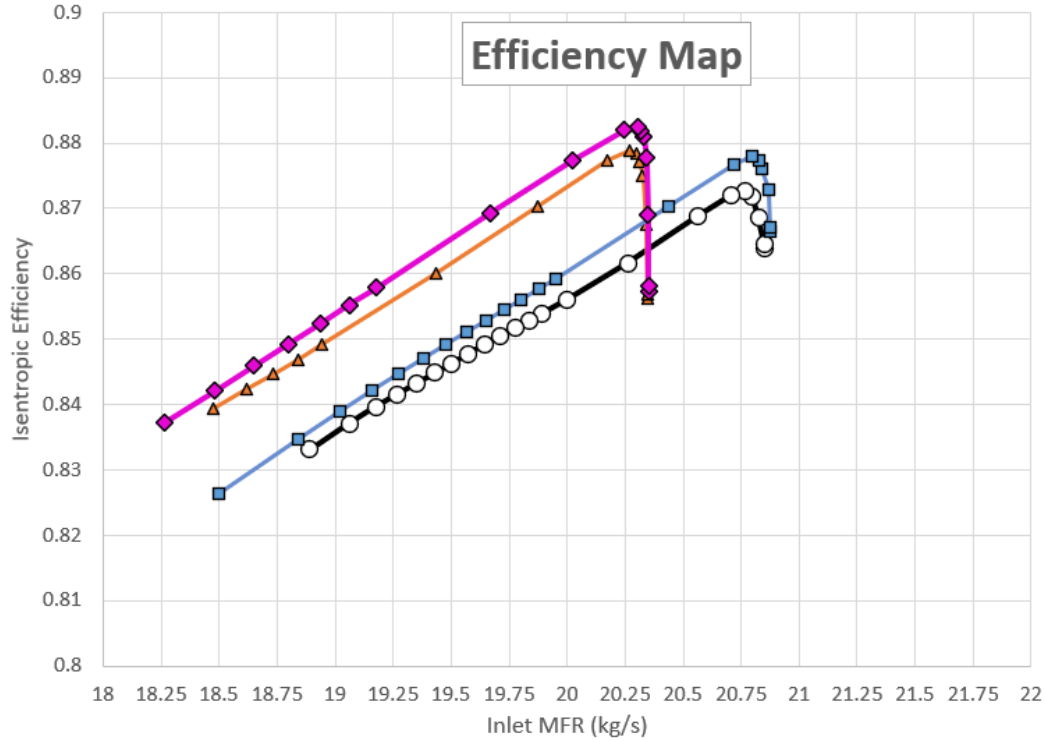

Figure 4.3 : Efficiency map of the combined geometry

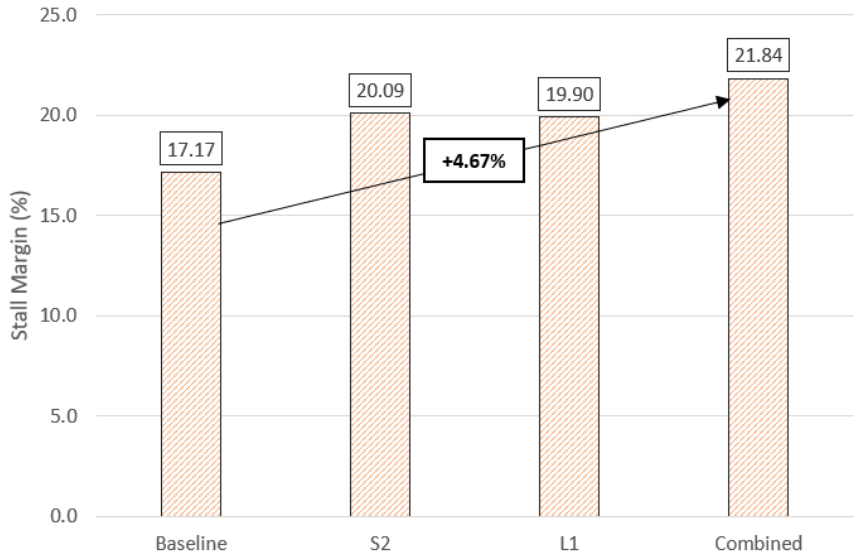

Figure 4.4 : Stall margins of most promising geometries

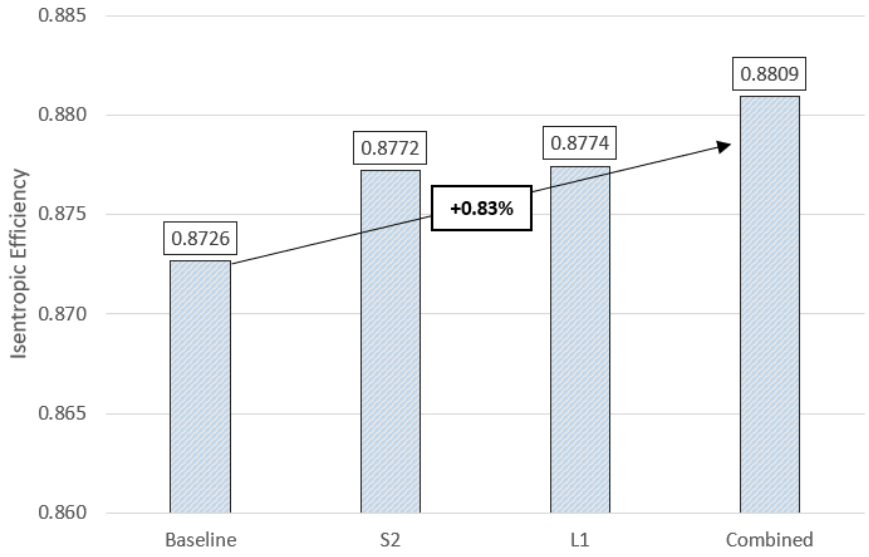

Figure 4.5 : Design point isentropic efficiencies of most promising geometries

4.3 Blade-to-Blade Flow Field Results

It is seen that passage the shock has been moved further downstream and weakened with aft sweep applications. Blade loading around the leading edge is a direct combination of the single cases, which is less compared to the baseline. Pressure side acceleration is smoother compared to baseline and single solutions. (Figure 4.6)

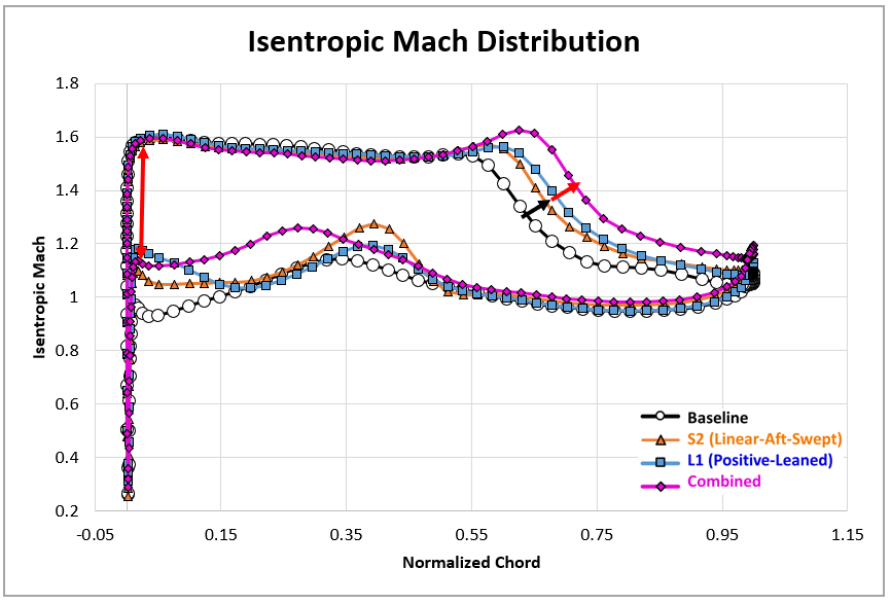

Figure 4.6 : Isentropic Mach plots of most promising geometries at %90 span height and at the design point

4.4 Surface Streamline Results

The comparison of the surface limiting streamlines of the combined geometry with baseline are given in Figure 4.7. The passage shock at the tip section is clearly seen to be shifted to downstream. The separation bubble is smaller compared to the baseline. Perpendicularity of shock at the tip is seen to be conserved here, too.

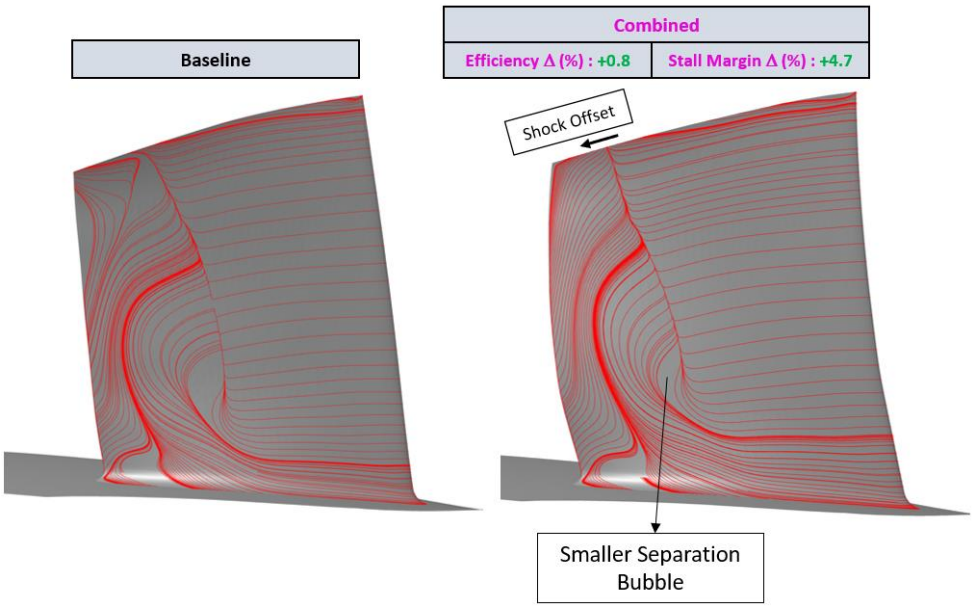

Figure 4.7 : Surface limiting streamlinesof the combined geometry and baseline at design point

4.5 Tip Leakage Flow

The tip leakage vortex and entropy generation of the combined geometry with baseline are given in Figure 4.8 The tip leakage vortex of the combined geometry is seen to be less strong. Entropy generation is seen to be improved. Almost all the streamlines of the tip leakage vortex mix with mainstream without feeding the secondary vortex of the adjacent blade around the trailing edge.

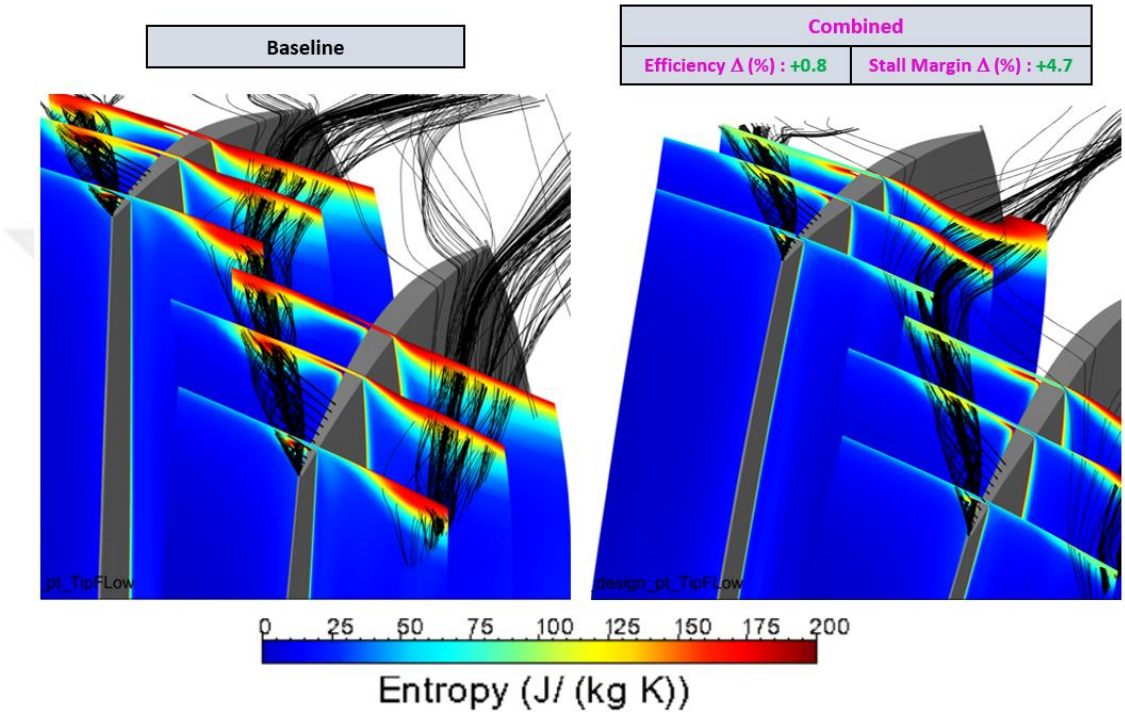

Figure 4.8 : Tip leakage vortex and entropy generation of combined geometry at design point

5. CONCLUSION

A CFD model has been conducted for NASA Rotor 37 and the model has been validated through a mesh independency study. Total 8 new blade geometries have been generated based on Rotor 37, which are swept and leaned, and investigated in terms of aerodynamical performance and flow physics.

It is seen that the forward sweep pushes the shock system to be expelled, which results in a decrease in the isentropic efficiency and stall margin. It also leads to the growth of the separation bubble on the suction side and enlarges the tip leakage vortex which results in higher entropy generation. All the forward sweep characteristics are vice-versa for the aft sweep strategy. The forward sweep is seen not to be a favorable design against the aft-sweep. Similar findings as stated by Verstraete (2011), Benini (2007) and Jang(2006).

It is seen that the positive lean pull the shock system to passage, which increases the isentropic efficiency and stall margin. Also, the positive lean eliminates the separation bubble on the suction side and reduces the tip leakage vortex which results in smaller entropy generation areas. All the positive lean characteristics are vice-versa for the negative-lean strategy. The positive lean is seen to be a favorable design strategy against the negative lean. Similar findings as stated Wang(2021), Aziz(2014), Verstraete (2011), Benini (2007) and Jang(2006) were observed.

The linear combination of the most promising swept and leaned geometry showed that the combined geometry shows a better flowfield compared to singular cases; however, the improvement of the global performance is not the direct combination of the singular cases.

REFERENCES

Abdelhamid, H. F., Shreeve, R. P., & Hobson, G. V. (1998). Sweep in a transonic fan rotor: Part 2 — CFD and stress analyses. *Volume 1: Turbomachinery*. https://doi.org/10.1115/98-gt-579

Aziz, M. A., Owis, F. M., & Abdelrahman, M. M. (2014). Design optimization of a transonic-fan rotor using numerical computations of the full compressible navier-stokes equations and simplex algorithm. *International Journal of Rotating Machinery*, *2014*. https://doi.org/10.1155/2014/743154

Beatty, L. A., Savage, M., & Emery, J. C. (1954). Research memorandum low-speed cascade tests of two 45 0 swept compressor blades with constant spanwise loading. *National Advisory Committee For Aeronautics Washington.*

Benini, E., & Biollo, R. (2007). Aerodynamics of swept and leaned transonic compressor-rotors. *Applied Energy*, *84*(10), 1012–1027. https://doi.org/10.1016/j.apenergy.2007.03.003

Biollo, R., & Benini, E. (2009). Shock/boundary-layer/tip-clearance interaction in a transonic rotor blade. *Journal of Propulsion and Power*, *25*(3), 668–677. https://doi.org/10.2514/1.39541

Biollo, R., & Benini, E. (2011). State-of-art of transonic axial compressors. *Advances in Gas Turbine Technology*. https://doi.org/10.5772/25257

Bliss, D., Hayden, R., Murray, B., & Schwaar, P. (1976). Design considerations for a novel low source noise transonic fan stage. *3rd Aeroacoustics Conference*. https://doi.org/10.2514/6.1976-577

Calvert, W. J., & Ginder, R. B. (1999). Transonic fan and compressor design. *Proceedings of the Institution of Mechanical Engineers, Part C: Journal of Mechanical Engineering Science*, *213*(5), 419–436. https://doi.org/10.1243/0954406991522671

Cao, Z., Zhang, X., Liang, Y., & Liu, B. (2022). Influence of Blade Lean on Performance and Shock Wave/Tip Leakage Flow Interaction in a Transonic Compressor Rotor. *Journal of Applied Fluid Mechanics*, *15*(1), 153–167. https://doi.org/10.47176/jafm.15.01.32753

Chen, N. X., Zhang, H. W., & Huang, W. G. (2010). Aerodynamic sweeping study and design for transonic compressor rotor blades. *Journal of Thermal Science*, *19*(4), 295–299. https://doi.org/10.1007/s11630-010-0386-9

Copenhaver, W. W., Mayhew, E. R., Hah, C., & Wadia, A. R. (1996). The effect of tip clearance on a swept transonic compressor rotor. *Journal of Turbomachinery*, *118*(2), 230–239. https://doi.org/10.1115/1.2836630

Cui, W., Xiang, X., Zhao, Q., & Xu, J. (2016). The effect of sweep on flowfields of a highly loaded transonic rotor. Aerospace Science and Technology, 58, 71–81. https://doi.org/10.1016/j.ast.2016.08.002

Denton, J. D. (1993). Loss mechanisms in turbomachines. *Volume 2: Combustion and Fuels; Oil and Gas Applications; Cycle Innovations; Heat Transfer; Electric Power; Industrial and Cogeneration; Ceramics; Structures and Dynamics; Controls, Diagnostics and Instrumentation; IGTI Scholar Award*. https://doi.org/10.1115/93-gt-435

Denton, J. D., & Xu, L. (2002a). The effects of Lean and Sweep on Transonic Fan Performance. *Volume 5: Turbo Expo 2002, Parts A and B*. https://doi.org/10.1115/gt2002-30327

Domercq, O. (2012). *HP Compressor Aerodynamics: 3D Design and Stage Matching. Von Karman Institute for Fluid Dynamics Lecture Series 2012-2013*.

Dunham, J. (Ed.). (1998). CFD Validation for Propulsion System Components. *Agard Advisory Report 355*.

Envia, E., & Nallasamy, M. (1999). Design selection and analysis of a swept and leaned stator concept. *Journal of Sound and Vibration*, *228*(4), 793–836. https://doi.org/10.1006/jsvi.1999.2441

Furukawa, M., Inoue, M., Saiki, K., & Yamada, K. (1999). The role of tip leakage vortex breakdown in compressor rotor aerodynamics. *Journal of Turbomachinery*, *121*(3), 469–480. https://doi.org/10.1115/1.2841339

Hah, C., & Wennerstrom, A. J. (1990). Three-Dimensional Flowfields Inside a Transonic Compressor with Swept Blades. http://asmedigitalcollection.asme.org/GT/proceedings-pdf/GT1990/79047/V001T01A107/4216494/v001t01a107-90-gt-359.pdf

Hah, C., Puterbaugh, S. L., & Wadia, A. R. (1998). Control of shock structure and secondary flow field inside transonic compressor rotors through aerodynamic sweep. *Volume 1: Turbomachinery*. https://doi.org/10.1115/98-gt-561

Hayden, R. E., Bliss, D. B., Murray, B. S., Chandiramani, K. L., Smullin, J. I., & Schwaar, P. G. (1977). Analysls and design of a high tip speed, low source noise aircraft fan incorporating swept leading edge rotor and stator blades. *NASA CR-135092*

He, X., Zhu, M., Xia, K., Fabian, K., Teng, J., & Vahdati, M. (2023). Validation and verification of Rans solvers for tuda-GLR-openstage transonic axial

compressor. *Journal of the Global Power and Propulsion Society*, *7*, 13–29. https://doi.org/10.33737/jgpps/158034

Inoue, M., Furukawa, M., Saiki, K., & Yamada, K. (1998). Physical explanations of tip leakage flow field in an axial compressor rotor. *Volume 1: Turbomachinery*. https://doi.org/10.1115/98-gt-091

Jang, C.-M., Samad, A., & Kim, K.-Y. (2006). Optimal design of swept, leaned and skewed blades in a transonic axial compressor. *Volume 6: Turbomachinery, Parts A and B*. https://doi.org/10.1115/gt2006-90384

Ji, L., Chen, J., & Lin, F. (2005a). Review and understanding on sweep in axial compressor design. *Volume 6: Turbo Expo 2005, Parts A and B*. https://doi.org/10.1115/gt2005-68473

Kurzke, J. (1996). How to get component maps for Aircraft Gas Turbine Performance Calculations. *Volume 5: Manufacturing Materials and Metallurgy; Ceramics; Structures and Dynamics; Controls, Diagnostics and Instrumentation; Education; General*. https://doi.org/10.1115/96-gt-164

Lewis, R. I., & Hill, J. M. (1971). The influence of sweep and dihedral in turbomachinery blade rows. *Journal of Mechanical Engineering Science*, *13*(4), 266–285. https://doi.org/10.1243/jmes_jour_1971_013_043_02

Obrecht, T. (2012). *HP Compressor Preliminary Design*. *Von Karman Institute for Fluid Dynamics Lecture Series 2012-2013*.

Okui, H., Verstraete, T., Van den Braembussche, R. A., & Alsalihi, Z. (2011). Three dimensional design and optimization of a transonic rotor in axial flow compressors. *Volume 7: Turbomachinery, Parts A, B, and C*. https://doi.org/10.1115/gt2011-45425

Reid, L., & Moore, R. D. (1978a). Design and Overall Performance of Four Highly Loaded, High-Speed Inlet Stages for an Advanced High-Pressure-Ratio Core Compressor. *NASA Technical Paper 1337*.

Reid, L., & Moore, R. D. (1978b). Performance of Single-Stage Axial-Flow Transonic Compressor with Rotor and Stator Aspect Ratios of 1.19 and 1.26, Respectively, and With Design Pressure Ratio of 2.05. *NASA Technical Paper 1338*.

Roache, P. J. (1996). *Verification and Validation in Computational Science and Engineering*.

Seo, S. J., Choi, S. M., & Kim, K. Y. (2008). Design optimization of a low-speed fan blade with sweep and lean. *Proceedings of the Institution of Mechanical Engineers, Part A: Journal of Power and Energy*, *222*(1), 87–92. https://doi.org/10.1243/09576509JPE410

Shabbir, A., Zhu, J., & Celestina, M. (1996). Assessment of three turbulence models in a compressor rotor. *Volume 1: Turbomachinery*. https://doi.org/10.1115/96-gt-198

Smith, L. H., & Asme, M. (1963). *Sweep and Dihedral Effects in Axial Flow Turbomachinery*. http://fluidsengineering.asmedigitalcollection.asme.org/

Suder, K. L. (2020). NASA's role in Gas Turbine Technology Development: Accelerating technical progress via collaboration between academia, industry, and government agencies. *Journal of Turbomachinery*, *143*(1). https://doi.org/10.1115/1.4048696

Suder, K.L. (1996). Experimental Investigation of the Flow Field in a Transonic, Axial Flow Compressor With Respect to the Development of Blockage and Loss. *NASA Lewis Research Center. Clevelend, Ohio.*

Sun, S., Wang, S., & Chen, S. (2020). The influence of diversified forward sweep heights on operating range and performance of an ultra-high-load low-reaction transonic compressor rotor. *Energy*, *194*. https://doi.org/10.1016/j.energy.2019.116857

Wadia, A. R., Szucs, P. N., & Crall, D. W. (1997). Inner workings of aerodynamic sweep. *Volume 1: Aircraft Engine; Marine; Turbomachinery; Microturbines and Small Turbomachinery*. https://doi.org/10.1115/97-gt-401

Wang, Z., Qu, F., Wang, Y., Luan, Y., & Wang, M. (2021). Research on the lean and swept optimization of a single stage axial compressor. *Engineering Applications of Computational Fluid Mechanics*, *15*(1), 142–163. https://doi.org/10.1080/19942060.2020.1862708

APPENDICES

APPENDIX A: Spanwise stacking distribution types used in geometries

APPENDIX B: Blade-to-blade surface demonstration

APPENDIX C: Survey locations of experimental setup for NASA Rotor 37

APPENDIX D: Equations

APPENDIX A

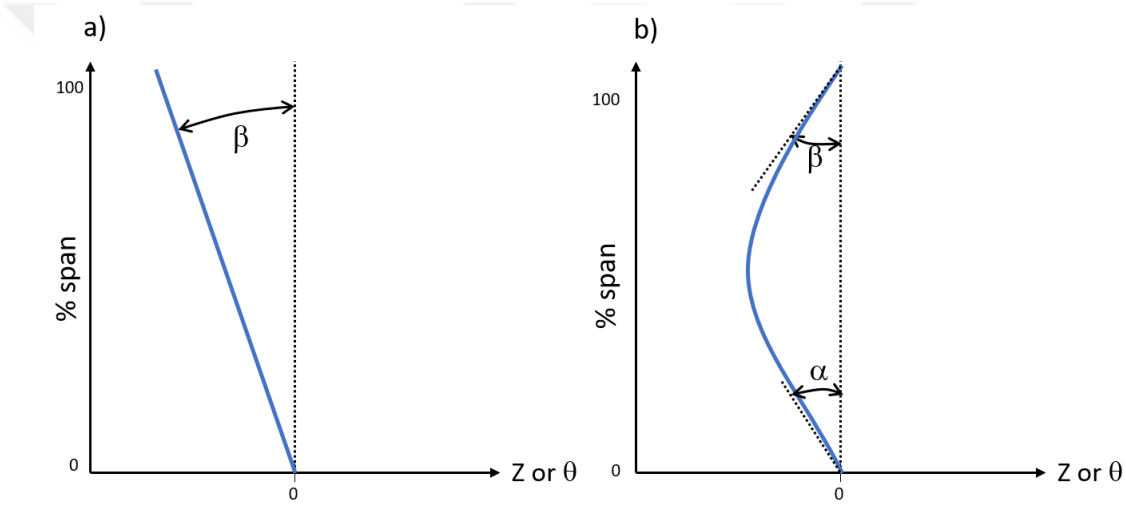

Figure A.1: Sweep Distribution: (a)Single Parameter. (b)Double Parameter

APPENDIX B

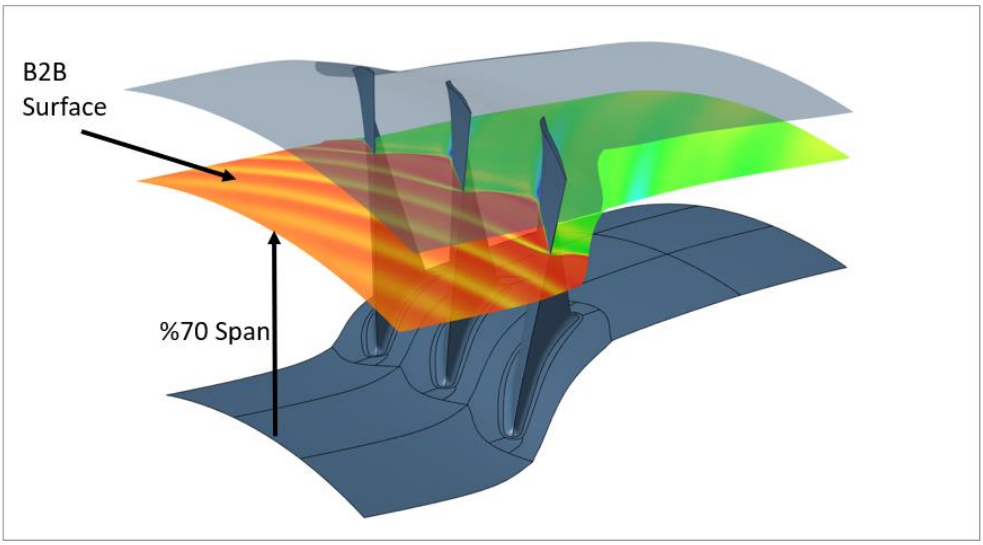

Figure B.1: Blade-to-blade surface demonstration through isometric view

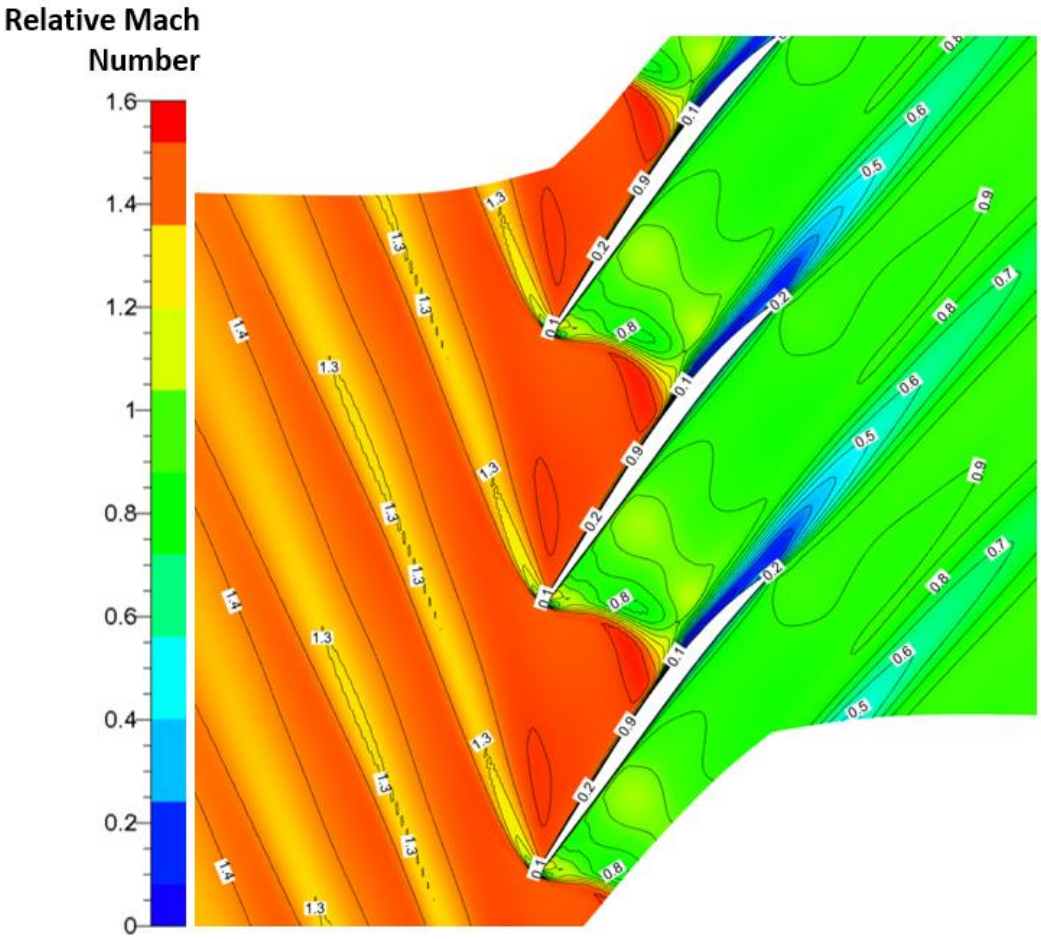

Figure B.2- Design point B2B plane at %70 Span of CFD model

APPENDIX C

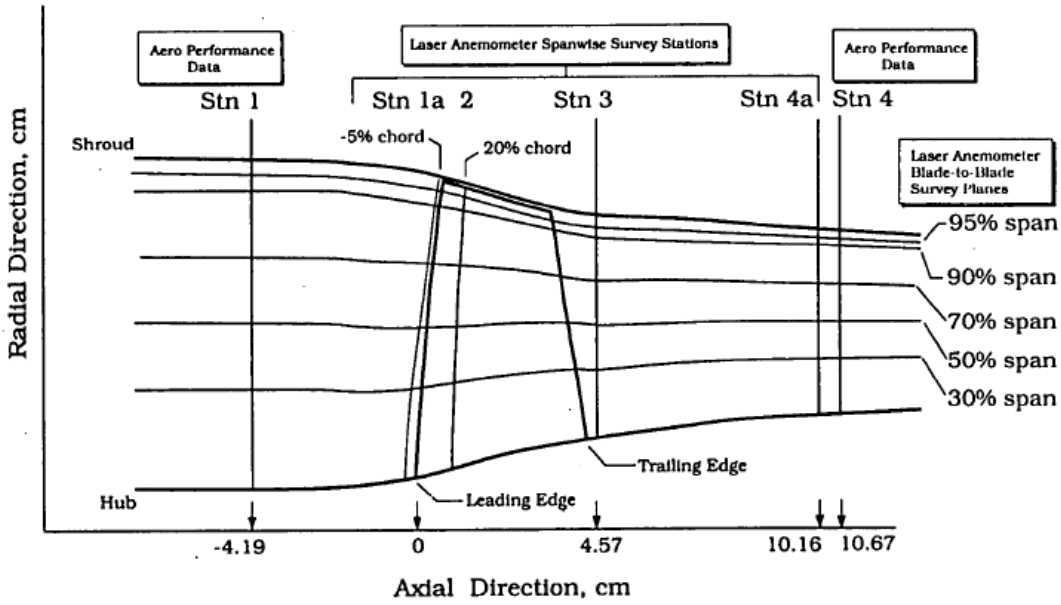

Figure C.1: Survey locations of experimental setup for NASA Rotor 37 (Dunham, 1998)

APPENDIX D

$$PR = \frac{Mass\ Weighted\ Average\ of\ the\ Absolute\ Total\ Pressure\ at\ Rotor\ Exit}{Mass\ Weighted\ Average\ of\ the\ Absolute\ Total\ Pressure\ at\ Rotor\ Inlet}$$

$$TR = \frac{Mass\ Weighted\ Average\ of\ the\ Absolute\ Total\ Temperature\ at\ Rotor\ Exit}{Mass\ Weighted\ Average\ of\ the\ \ Absolute\ Total\ Temperature\ at\ Rotor\ Inlet}$$

$$Stall\ Margin_{@Constant\ Speed} = \left(\frac{(PR/\dot{m})_{Stall\ point}}{(PR/\dot{m})_{Design\ point}} - 1 \right) \times 100$$

$$Isentropic\ Efficiency = \frac{(PR)^{\frac{(\gamma-1)}{\gamma}} - 1}{(TR) - 1}$$

CURRICULUM VITAE

Name Surname : Hasan Berk Güçlü

EDUCATION :

- **B.Sc. :** 2020, Istanbul Technical University, Faculty of Aeronautics and Astronautics, Aeronautical Engineering